Formation and Characterization of Pulsed Laser Ablated Magnetoresistive Material

by

Schadrack Nsengiyumva

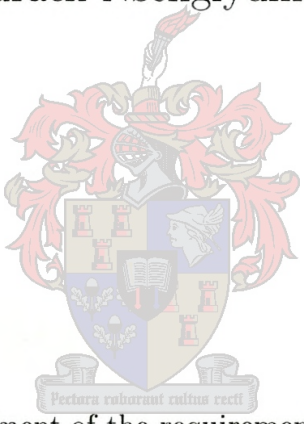

Thesis presented in partial fulfillment of the requirements for the degree of Master of Science in Physics at the University of Stellenbosch

Supervisor: Prof. R. Pretorius

Dept of Physics

University of Stellenbosch

November 2002

Declaration

I, the undersigned, hereby declare that the work contained in this thesis is my own original work and has not previously in its entirety or in part been submitted at any university for a degree.

ABSTRACT

In this investigation the formation of thin film manganites and their electrical characteristics is studied. In order to see the effect of oxidation states on magneto-resistivity, 80% of Mn is replaced by Fe. Pulsed laser deposition (3 J/cm^2), carried out in oxygen partial pressures ranging from 0.01 mbar to 1.00 mbar was used to fabricate the thin films from two target compositions, namely $La_2CaMn_{2.94}Fe_{0.06}O_9$ and $La_2CaMn_{0.6}Fe_{2.4}O_9$. Films were deposited on Si$<100>$, MgO$<100>$, $SrTiO_3<100>$ and $LaAlO_3<100>$ single crystal substrates. Samples were characterized by RBS, AFM, SEM, and XRD. Electrical measurements were also carried out.

One of the main characterization techniques in this investigation is Rutherford Backscattering Spectrometry (RBS). It has been shown that RBS is a very powerful characterization technique when used in conjunction with the RUMP simulation program. The effect of various parameters can be determined beforehand by RUMP simulation of the thin film structures to be investigated. Simulation shows that RBS is an excellent characterization tool for determining film thickness and stoichiometry. The role of oxygen uptake in $La_2CaMn_{3-x}Fe_xO_9$ was investigated as the oxidation states of elements in manganite materials have a large effect on their magnetoresistive properties. The height of the La signal can be used as a measure of the oxygen content. RBS spectra of films deposited on single crystal silicon substrates at different ambient pressures show that the fit between simulated and measured RBS spectra improves with higher oxygen pressures, thereby indicating better quality manganite material. The RBS spectra also show that the films have good stoichiometry.

Atomic force microscopy was used to determine the roughness of the thin films. The annealed film (average roughness 4.5 nm) shows a surface smoother than the non-annealed film (average roughness 5.3 nm). SEM measurements show that in the case of samples having a high Fe content, the crystallite size varies between about 0.04 μm and 0.10 μm, while for samples with high manganese content, the crystallinity varies between 0.03 μm and 0.06μm. Manganites were analyzed using Bragg-Brentano (2θ) X-ray diffraction. Measurements show that manganite films cannot be grown epitaxially on Si$<100>$ and MgO$<100>$ single crystals due to a large lattice mismatch. In the case of $SrTiO_3$ and $LaAlO_3$ several reflections and sharp peaks from the film can be seen, indicating reasonable epitaxial growth. SEM measurements of the samples however show polycrystallinity. Complete epitaxy has thus not occurred, but many grains have an epitaxial orientation. Resistance versus temperature (the room temperature to about 100 K) in zero magnetic field was measured for a $La_2CaMn_{0.06}Fe_{2.4}O_9$ thin film and maximum resistance corresponding to about 108 K was found. At higher temperatures the resistance decreases as temperature increases. The manganite thin film therefore shows semiconductor behaviour. Resistance measurements carried out at different magnetic fields (0 - 1 T) show a small positive magnetoresistance of 0.83 %. Usually the magnetoresistance phenomenon is measured at higher magnetic fields and this could be the reason for our low value as well as the fact that the iron content could be too high.

OPSOMMING

In hierdie ondersoek is die formasie en karakterisering van dunlagie manganiete ondersoek. Om die effek van oksidasie-toestand op magnetoresistiwiteit te bepaal, is 80% van die Mn verplaas deur Fe. Pulseerde laser deposissie(3 J/cm^2), is uitgevoer by 'n parsiële suurstof druk tussen 0.10 en 1.00 mbar deur gebruik te maak van $La_2Ca Mn_{2.94}Fe_{0.06}O_9$ en $La_2CaMn_{0.6}Fe_{2.4}O_9$ teiken skywe. Dunlagies was gedeponeer op Si<100>, MgO<100>, $SrTiO_3$<100> en $LaAlO_3$<100> enkelkristal substrate. Die dunlagies is daarna ge-karakteriseer met behulp van Rutherford terugverstrooing (RBS), atoom krag mikroskopie(AFM), skandeer elektronmikroskopie (SEM) en x-straal diffraksie(XRD). Elektriese metings is ook uitgevoer.

Een van die hoof tegnieke wat gebruik is in hierdie ondersoek is Rutherford terugverstrooing (RBS) van 2 Mev alfa-deeltjies. In hierdie navorsing is aangetoon dat RBS saam met spektra simulasie(RUMP), 'n besondere kragtige metode is om die stoichiometrie en dikte van manganiet lagies te bepaal. Die rol van die opname van suurstof in die dunlagies was ondersoek, aangesien die oksidasie toestand van manganiet lagies 'n groot effek het op hulle magnetoresistiwiteit. Die hoogte van die La sein is gebruik as 'n maatstaf van suurstof inhoud. RBS spektra van dunlagies gevorm op enkelkristal silikon substrate by verskillende parsiële suurstof drukke wys dat die passing tussen gemete en gesimuleerde spektra verbeter by hoër suurstof drukke, wat beter kwaliteit manganiet materiaal aandui. Die RBS spektra het ook aangetoon dat die stoichiometrie van die lagies uitstekend is.

Atoom krag mikroskopie(AFM) is gebruik om die grofheid van die oppervlaktes van die dunlagies te bepaal. Lagies wat by 750 grade celsius uitgegloei is (gemiddelde gladheid van 4.5 nm) was gladder as films wat nie na ablasie uitgegloei is nie (gemiddelde gladheid van 5.3 nm). SEM metings toon ook dat dunlagies met 'n hoë Fe inhoud 'n kristalliet deursnit het van 0.04 tot 0.10 mikrometer en die met 'n hoë mangaan inhoud 'n poli-kristalliniteit het van tussen 0.03 en 0.06 mikrometer het. Bragg-Brentano(twee-theta) X-straal diffraksie meting wys dat manganiet films nie epitaksieël op Si<100> en MgO<100> enkelkristal substrate gevorm kan word nie, weens 'n groot verskil in die kristal-rooster parameters. SEM metings van die monsters wys polikristalliniteit. Algehele epitaksie het dus nie plaasgevind nie, maar verskeie kristalliete het 'n epitaksiële orientasie. Weerstand metings is gemaak by temperature so laag as 100 Kelvin vir $La_2CaMn_{0.06}Fe_{2.4}O_9$ dunlagies en 'n maksimum weerstand is by 108 Kelvin gevind. By hoër temperature het die weerstand afgeneem soos die temperatuur toeneem, wat halfgeleier gedrag aandui. Weerstand metings by verskillende magneetvelde (0 tot 1 Tesla) wys 'n klein magnetoresistiwiteits effek van 0.83%. Gewoonlik word magnetoresistiwiteit gemeet by hoë magneet velde (ongeveer 6 Tesla). Dit, sowel as die hoë Fe samestelling van die monsters kan die rede wees vir die lae magnetoresistiwiteit wat waargeneem word.

ACKNOWLEDGEMENTS

I would like to extend my gratitude and sincere appreciation to the following group of people, without whose assistance and encouragement this work would not have been achieved.

- Prof. R. Pretorius, Physics Department, University of Stellenbosch, my supervisor, for his guidance, constant encouragement, continuous support and constructive discussions throughout his supervision of this investigation;
- Dr. K. Bouziane, Physics Department, Sultan Qaboos University, for suggesting and initiating this project and for his assistance with pulsed laser deposition, XRD and SEM measurements;
- Dr. M. Maaza, Physics Department, University of the Witwatersrand, for his support and assistance with electrical measurements;
- Dr. C. Theron, iThemba Labs, for his help during experiments and assistance with Latex;
- The Baldé family, for their encouragement and support;
- Dr. S. Wyngaardt, Physics Department, University of the Western Cape, for his encouragement, his willingness to help all the time;
- The Laser Research Institute of the Physics Department, University of Stellenbosch, for their assistance with excimer laser during pulsed laser deposition;
- Mr U. Buttner, Electrical and Electronic Engineering and Mr U. Deutchlander, Physics Department, University of Stellenbosch, for their assistance with pulsed laser deposition;
- All the staff and my fellow postgraduate students of the Physics Department, for their invaluable help in many circumstances;
- The Rwandan Governement and The World Bank for their financial support;
- My wife, Philomene, for her patience and understanding during my long absence , her enduring encouragement and moral support through sms and e-mails;
- My kids, Blaise, Robert, Lambert and Céline for their strong patience and obedience to their mum;
- My gratitude to Him who gave me the health and strength to perform this project and still keeps upon me and my family.

Contents

Chapter 1

Introduction

1.1 Electrical Properties of Materials

1.1.1 Introduction

The electrical classification of solid materials can be visualized in terms of the band theory of solids and are strongly correlated with the interatomic spacing in the solid. The electron energy levels in a solid are often expressed in relation to the Fermi energy which is the maximum energy occupied by an electron at 0 K. The concept of the Fermi energy is a crucially important concept for the understanding of the electrical and thermal properties of solids. Therefore, the differences between metals, insulators and semiconductors depend on:

1. The band structure of each,
2. Whether the valence bands are full or only partly full,
3. The magnitude of any energy gap between full and empty bands.

The electrical properties are also determined by point defects in a solid. These are imperfections in a crystal lattice and the main types of points defects are substitution, vacancies, interstitial ions, electrons, and holes.

1.1.2 Metals

A solid is considered to be a metal if it has high electrical and thermal conductivity. The chemical definition of a metal also includes having a characteristic lustre or shine. The metals are also malleable and ductile. The microscopic properties of metals are often stated in terms of their Fermi energy and their free electron density. In the case of electrons, it is necessary to use quantum statistics, with the requirement that each state of the system, specified by a set of quantum numbers, can be occupied by only one electron with respect to the Pauli exclusion principle. In terms of probability, the probability of finding an electron in a particular state of energy E is given by[1]

$$f(E) = \frac{1}{e^{(E-E_F)/kT} + 1}, \tag{1.1}$$

where E_F is the Fermi energy. The function *f(E)* is called the Fermi-Dirac distribution function. The function *f(E)* has the value of unity for $E < E_F$ and zero for $E > E_F$. **Figures 1.1**(a) and (b) show the behaviour of *f(E)* at T= 0 K and $T > 0$ K respectively. Thus at $T = 0$ K, all levels with energy less than E_F will be completely filled and those above E_F will be completely empty. The main variations in the Fermi-Dirac distribution function with temperature occur in the vicinity of the Fermi energy. At $T > 0$ K, only a small fraction of the levels with energies greater than the Fermi energy is occupied. Moreover, a small fraction of the levels below the Fermi energy is empty. The conduction electron population for a metal is calculated by multiplying the density of conduction electron states *N(E)* with the Fermi function *f(E)*. The number of conduction electrons per unit volume per unit energy is[1]

$$\frac{dn}{dE} = N(E)f(E) = \frac{8\sqrt{2}\pi m^{3/2}}{h^3}\sqrt{E}\frac{1}{e^{(E-E_F)/kT} + 1}. \tag{1.2}$$

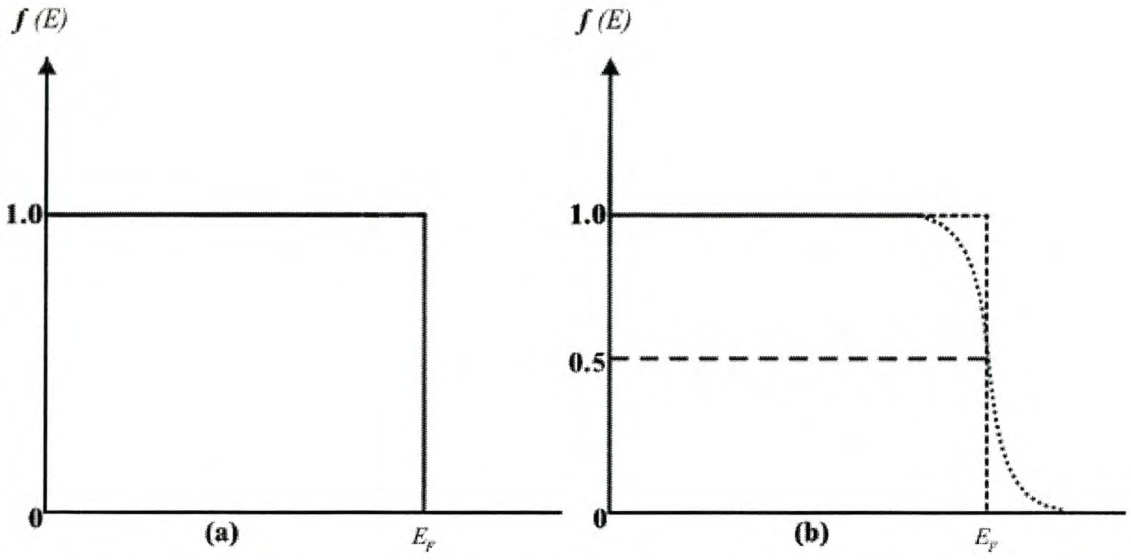

Figure 1.1: *A plot of the Fermi-Dirac distribution function at (a) $T = 0$ K, and (b) $T > 0$ K, where E_F is the Fermi energy*

The total population of conduction electrons per unit volume can be obtained by integrating equation 1.2 to obtain

$$n = \int_0^\infty N(E)f(E)dE = \frac{8\sqrt{2}\pi m^{3/2}}{h^3}\int_0^\infty \frac{\sqrt{E}}{e^{(E-E_F)/kT}+1}dE. \tag{1.3}$$

At 0 K, the top of the electron distribution is defined as E_F so that the integral becomes

$$n = \frac{8\sqrt{2}\pi m^{3/2}}{h^3}\int_0^{E_F} E^{1/2}dE = \frac{8\sqrt{2}\pi m^{3/2}}{h^3}\left(\frac{2}{3}E_F^{3/2}\right). \tag{1.4}$$

This expresses the conduction electron density n in terms of the Fermi energy E_F. We can also express the Fermi energy in terms of the electron density

$$E_F = \frac{h^2}{2m}\left(\frac{3n}{8\pi}\right)^{2/3}. \tag{1.5}$$

According to equation 1.5, E_F gradually increases with increasing electron concentration in the conduction band. This is right, because the electrons fill the available energy states, two electrons per state, in accordance with the Pauli exclusion principle, up to the Fermi

level. The order of magnitude of the Fermi energy for most metals is about 5 eV. We can also define the electron velocity at the Fermi level and the Fermi temperature respectively by the following expressions

$$v_F = \left(\frac{2E_F}{m}\right)^{1/2}, \tag{1.6}$$

$$T_F = \frac{E_F}{k}. \tag{1.7}$$

To summarize, a metal can be considered as a system with a large number of energy levels available to the valence electrons. The levels are filled in accordance with the Pauli exclusion principle beginning with $E = 0$ and ending to $E = E_F$. At $T = 0$ K, all levels below the Fermi energy are filled , while all levels above E_F are empty as it is shown in **Figure 1.2**. Though the levels are discrete, they are so close together that the

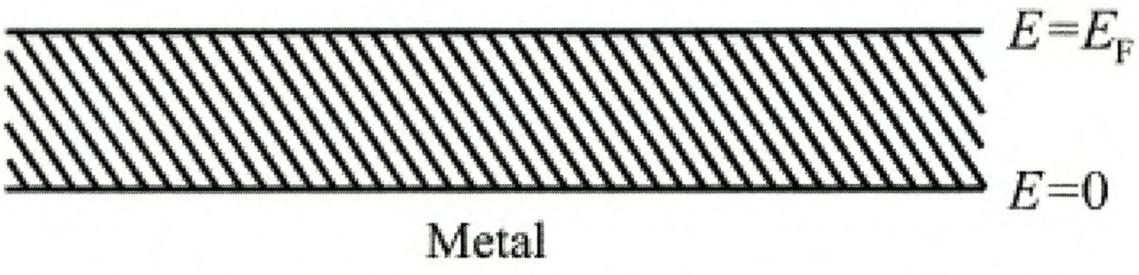

Figure 1.2: *A half-filled band of a conductor. At $T = 0$ K, the Fermi energy lies in the middle of the band.*

electrons have an almost continuous distribution of energy. At room temperature, a very small fraction of the valence electrons are excited above the Fermi energy. However, if an electric field is applied to the metal, electrons with energy near the Fermi energy require only a small amount of additional energy from the field to reach nearby empty energy levels. Thus electrons in a metal are free to move with only a small applied field because there are many unoccupied levels close to occupied energy levels.

1.1.3 Insulators

Most solid substances are insulators, and in terms of the band theory of solids this implies that there is a large forbidden gap between the energies of the valence electrons and the energy of the conduction electrons. The Fermi energy lies in the energy gap as it is illustrated in **Figure 1.3**. Since the energy gap for an insulator is large ($\sim$ 10 eV) compared

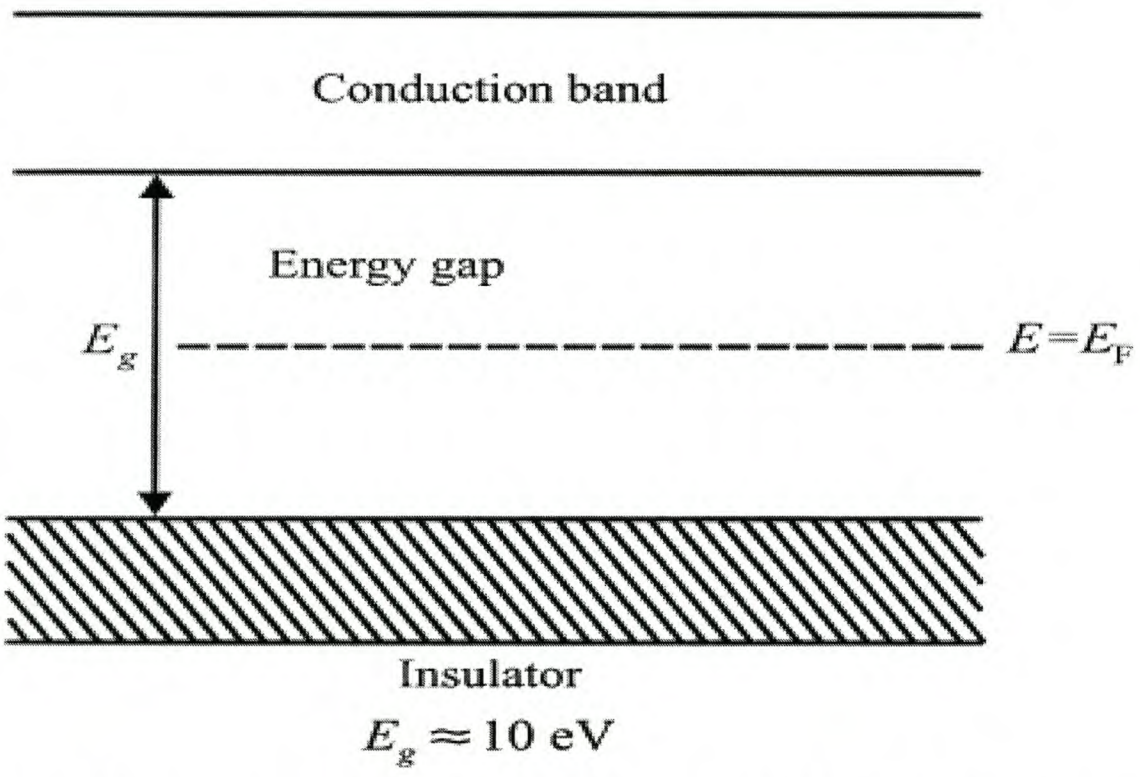

Figure 1.3: *An insulator at $T = 0$ K has a filled band and an empty conduction band. The Fermi energy lies somewhere between these bands.*

to kT at room temperature ($kT = 0.025$ eV), the Fermi-Dirac distribution predicts that there will be very few electrons thermally excited into the upper band at normal temperatures. Despite the many vacant states in the conduction band for an insulator, there are so few electrons actually occupying conduction band states that the overall contribution to electrical conductivity is very small, resulting in high resistivity for insulators. While the doping of insulators can dramatically change their optical properties, it is not enough

to overcome the large band gap to make them good conductors of electricity. However, impurity atoms at low concentrations in certain insulators may have large effects on the magnitude and mechanisms of conductivity. This is the case of colossal magnetoresistance materials which, basically insulators, become conductive by doping.

1.1.4 Semiconductors

Conversely to insulators, semiconductors have an energy gap of the order of 1 eV. At $T = 0$ K, all electrons are in the valence band and there are no electrons in the conduction band. This makes the semiconductors poor conductors at low temperature. However, since the Fermi level is located at about the middle of the gap , and since E_g is small (see **Figure 1.4**), appreciable numbers of electrons can be thermally excited from the valence band to the conduction band.

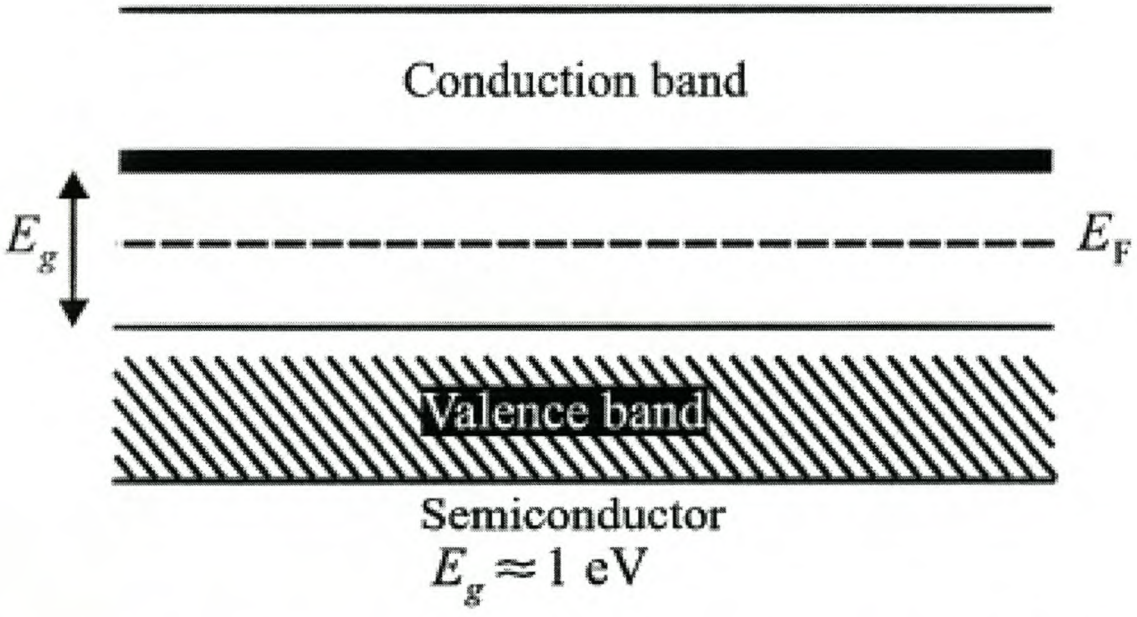

Figure 1.4: *The band structure of a semiconductor at room temperature ($T \approx 300$ K). Note that the energy gap is much smaller than in an insulator.*

A small applied potential can easily raise the energy of the electrons in the conduction band, resulting in a moderate current. For the fact that thermal excitation across the narrow gap is more probable at higher temperatures, the conductivity of semiconductors depends strongly on temperature and increases rapidly with the temperature. The semiconductivity is provided by electrons and holes. In a semiconductor, when an electron moves from the valence to the conduction band, it leaves behind a vacant site, or so-called hole which is nothing else but an electron-deficient site. The hole acts as a charge carrier in the sense that a valence electron from a nearby bond can be transferred into the hole, thereby filling it and leaving a hole behind in the electron's original place. In an intrinsic semiconductor, there are equal numbers of conduction electrons and holes. When conduction is dominated by acceptor impurities or donor impurities, the material is called an extrinsic semiconductor. Semiconductors doped with acceptor atoms (charge carriers are holes) are called p-type semiconductors and semiconductors doped with donor atoms (charge carriers are electrons) are called n-type semiconductors.

1.1.5 Superconductors

Certain materials show a very remarkable behavior; when they are cooled, their electrical resistance decreases in the usual way, but on reaching a certain temperature, they suddenly lose all traces of electrical resistance. They are then said to have passed into the superconducting state. The temperature at which the resistance of a superconductor drops dramatically to zero is called the transition temperature or the critical temperature. **Table 1.1** shows the critical temperatures for some metallic elements. Metal superconductors are in the category of Type I superconductors.

Table 1.1: *Critical temperatures for some Type I metallic superconductors*

Superconductor	Critical Temperature	Superconductor	Critical Temperature
Lead (Pb)	7.2 K	Lanthanum (La)	4.9 K
Tantalum (Ta)	4.47 K	Mercury (Hg)	4.15 K
Tin (Sn)	3.72 K	Indium (In)	3.40 K
Thallium (Tl)	1.70 K	Rhenium (Re)	1.697 K
Protactinium (Pa)	1.40 K	Thorium (Th)	1.38 K
Aluminium (Al)	1.175 K	Gallium (Ga)	1.10 K
Gadolinium (Gd)	1.083 K	Molybdenum (Mo)	0.915 K

Type I superconductors are characterized by their critical temperature T_c and critical magnetic field B_c. In the presence of a magnetic field, the value of T_c decreases with increasing magnetic field. The critical magnetic field as a function of temperature (see **Figure 1.5**) is given by the following approximate expression:

$$B_c(T) = B_0 \left[1 - \left(\frac{T}{T_c}\right)^2\right]. \tag{1.8}$$

The critical magnetic field B_0 is a maximum at $T = 0$ K. Above the critical magnetic field, the superconducting state is destroyed, and the material behaves as a normal conductor with finite resistance. Type II superconductors are characterized by two critical magnetic

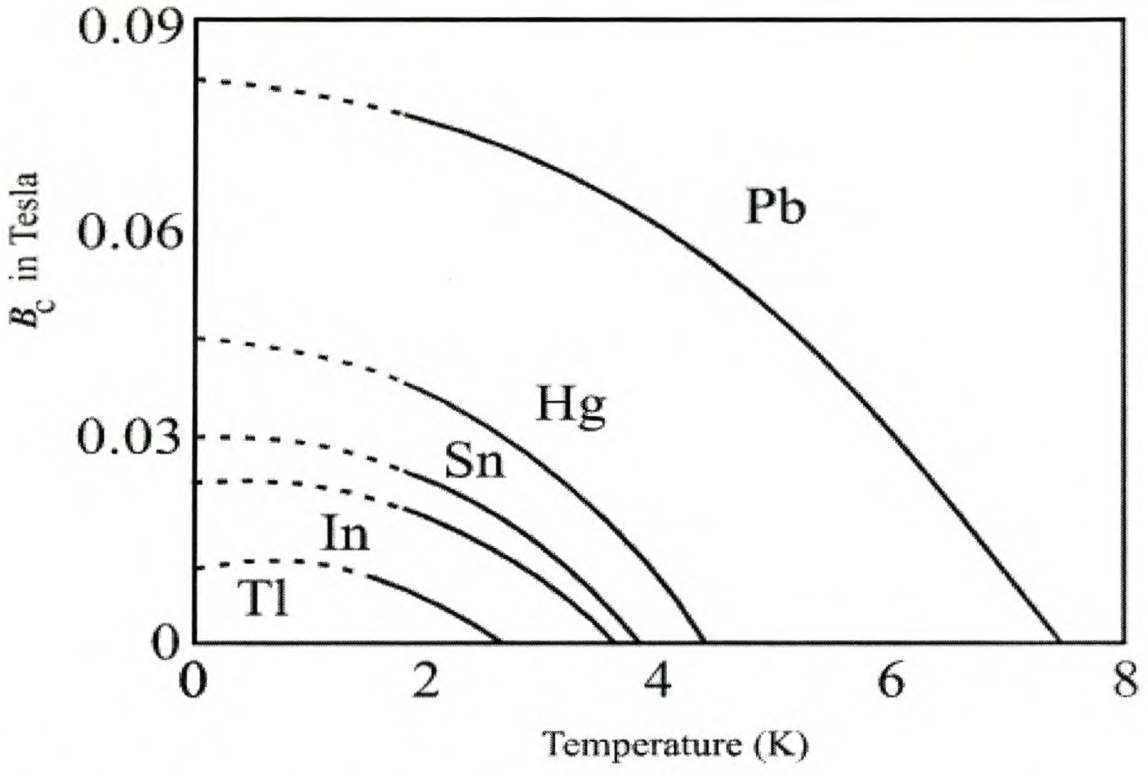

Figure 1.5: *The critical field $B_c(T)$ versus temperature T for several type I superconductors. For a given metal, the material is superconducting at fields and temperatures below its critical curve, and behaves like a normal conductor above that curve[1].*

fields B_{c1} and B_{c2}. Below B_{c1} (Meissner state), the superconductor excludes all the flux lines. It behaves exactly as type I superconductors. When the applied magnetic field exceeds the upper critical value B_{c2}, the flux lines penetrate in the material and the superconducting state is destroyed. At field strengths between B_{c1} and B_{c2}, the field begins to intrude into the material. When this occurs the material is said to be in a mixed state, often referred to as the vortex state. These different states are represented in **Figure 1.6**. The vortex regions are essentially filaments of normal regions through which magnetic field lines can pass. The latter are excluded from the superconducting regions. The superconducting state is defined by three important factors: critical temperature T_c, critical field B_{c2}, and critical density J_c. Each of the three parameters is very dependent on the other two properties present. Maintaining the superconducting state requires

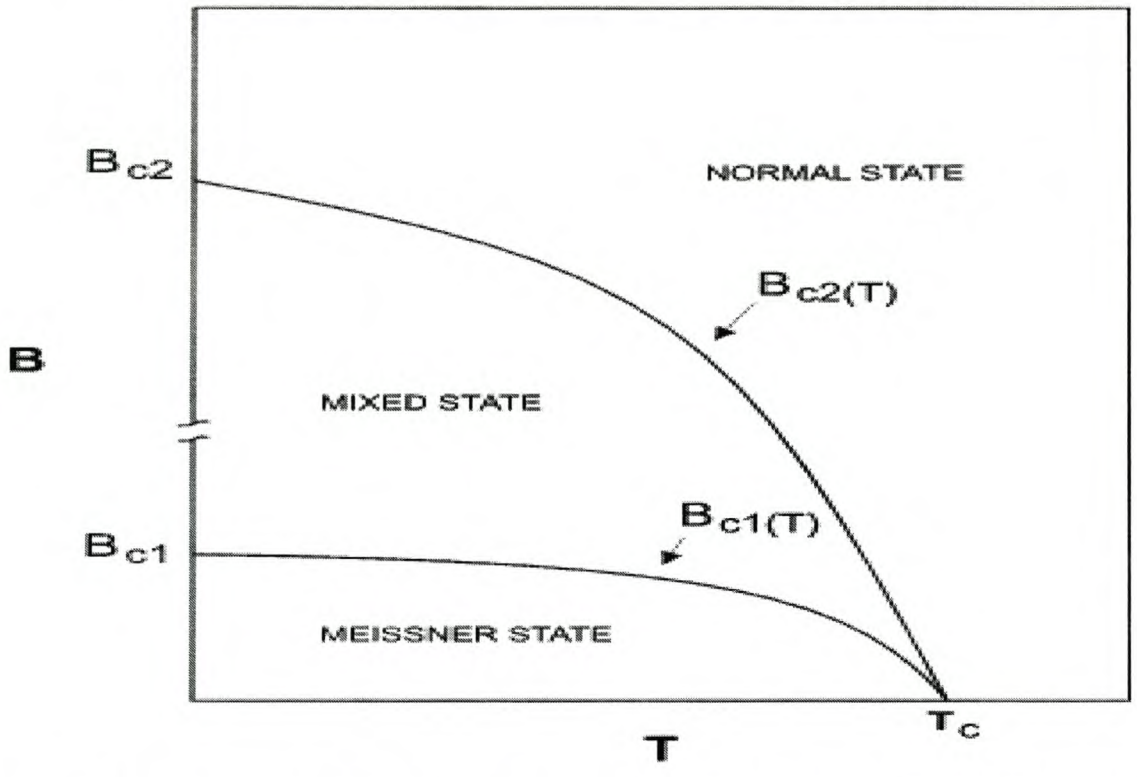

Figure 1.6: *Magnetic phase diagram showing the mixed and Meissner states of a type-II superconductor separated by the* $B_{c1}(T)$. *Note that* $B_{c2}(0)$ *in high-temperature superconductors (HTs) can be up to four orders of magnitude larger than* $B_{c1}(0)$*[2].*

that both the magnetic field and the current density, as well as the temperature, remain below the critical values, all of which depend on the material. The highest values of B_{c2} and J_c occur at 0 K, while the highest value of T_c occurs when B and J are zero. Type II superconductors are comprised of alloys and metallic compounds. The well-known $YBa_2Cu_3O_7$ is a type-II superconductor. The critical field values for type II superconductors are very large compared to type I superconductors. For instance, the upper critical field for the alloy $Nb_3(AlGe)$ is $B_{c2} = 44$ T and $T_c = 21$ K. For this reason, type II superconductors are suited for constructing high field-superconducting magnets. When a type II superconductor is in the mixed state, sufficiently large currents can lead to a motion of vortices perpendicular to the direction of the current, that is, parallel to the applied magnetic field. The stability of these vortices, in response to

the magnetic field, is very important because their motion results in resistivity. Vortex motion can be effectively pinned by adding defects, or by adding impurities or other special inclusions. Superconductors have remarkable properties which make them different from other materials. Among them we can name: perfect diamagnetism, Meissner effect, persistent currents, penetration depth, and coherence length.

1.1.6 Temperature dependence of resistance

In metallic conductors, the Fermi level (the highest filled energy level) lies within the conduction band, and the conduction electrons are not localized or bound to any particular atom. We can relate the conductivity of a metal as well as solid materials to microscopic parameters that describe the motion of electrons by the following expression

$$\sigma = ne\mu, \tag{1.9}$$

where $\mu = e\tau/m^*$; n is the carrier concentration, e the charge of an electron, τ the relaxation time (time between the collisions), m^* the effective mass of the electron, and μ the electron mobility. In metals, the carrier concentration, n, changes very slowly with temperature and includes only electrons which can easily be excited from occupied states into empty states, thus propagating through the metal. The relaxation time τ is inversely proportional to temperature, due to scattering by lattice vibrations (phonons). The total resistivity of a metal can be described by the Matthiessen rule

$$\rho_{total} = \rho_{thermal} + \rho_{impurity} + \rho_{deformation}. \tag{1.10}$$

The resistivity rises linearly with temperature, increasing thermal vibrations and density of vacancies. It can be described by the following expression

$$\rho_T = \rho_0 + aT, \tag{1.11}$$

where ρ_0 is the resistivity at 0 K, a, the temperature coefficient, and T the temperature. The conductivity of metals varies between 10^6 and 10^4 $\Omega^{-1}cm^{-1}$. **Figure 1.7** shows the variation of electrical resistivity (inverse of conductivity) versus temperature for pure and impure metals. Above the Debye temperature θ_D, the conductivity decreases with increasing T, generally decreasing as $1/T$[3,4]. In semiconductors, the carrier concentra-

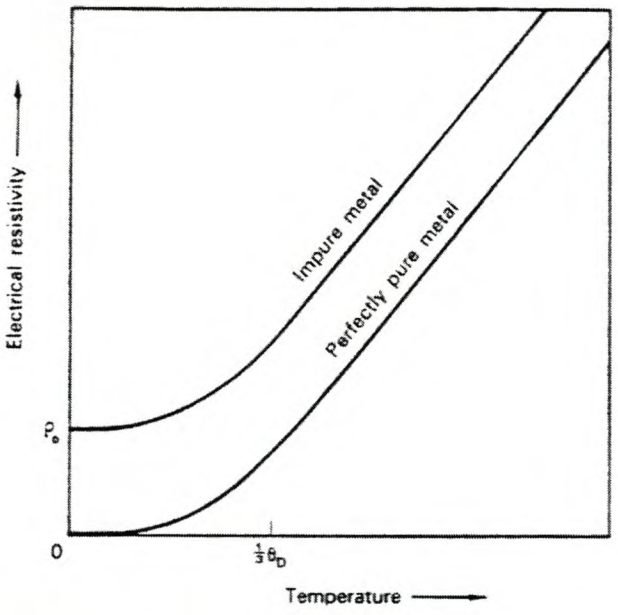

Figure 1.7: *Variation of resistance of metals with temperature[5].*

tion, n, increases as the temperature goes up, due to excitations across the band gap E_g, which is small ($\sim$ 1 eV) and is proportional to $e^{(E_g/kT)}$. Since the exponential dependence of n dominates, a plot of $\ln\sigma$ as function of $1/T$ is essentially linear. The conductivity in semiconductors increases as the temperature increases and varies between 10^{-5} and 10^3 $\Omega^{-1}cm^{-1}$.

In insulators, the band gap is large and prevents thermal elevation of electrons into the valence band. In impurity-containing insulators, low temperature conductivity is often

dominated by the impurity-controlled mechanisms and is termed extrinsic conductivity. At high temperature, the conductivity may become dominated by the fundamental ionic conductivity of the pure crystal, which is termed intrinsic conductivity. The conductivity values are generally lower than about $10^{-15}\ \Omega^{-1}cm^{-1}$. For semiconductors and insulators, the carrier concentration, n, usually increases exponentially with temperature. The effect of this dramatic increase in n outweighs the effect of the small decrease in the mobility, μ. Hence, the conductivity σ increases rapidly with temperature. Insulators are extreme examples of semiconductors in that n is very small at normal temperatures. Thus some insulators become semiconducting at high temperatures where n becomes appreciable and, conversely, some semiconductors become more like insulators at low temperatures.

For superconductors, the resistivity drops dramatically at their critical temperature. In striking contrast to metallic and alloy superconductors, with critical temperatures all in the range 2-23 K, all high-T_c superconductors have $T_c \geq 38$ K, and the most important ones, $T_c > 77$ K. The classical metallic superconductor's resisistivity obeys Bloch's law

$$\rho(T) = \rho_0 + \alpha T^5 \tag{1.12}$$

at low temperatures, ρ_0 being the residual resistivity due to impurity scattering, as illustrated in **Figure 1.8 (a)**. High-temperature superconductors have transition temperatures that are in the linear region, shown in **Figure 1.8 (b)**.

1.2 Magnetism in Solids

1.2.1 Introduction

The magnetism response of most magnetic solids involves the orientation of the magnetic dipoles contained in the solid. These magnetic dipoles, or magnetic moments, consist of the electron spin moment and the electron orbital dipole moment. For magnetic materials the relationship between the flux density **B**, the applied magnetic field **H**, and the

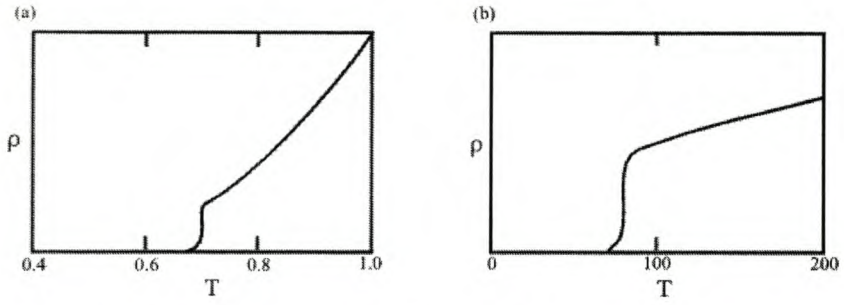

Figure 1.8: *Abrupt drop of the resistivity to zero at the superconducting transition T_c (a) for a low-temperature superconductor in the Bloch T^5 region and (b) for a high-temperature superconductor in the linear region. The temperature is given in the Kelvin scale, while the resistivity scales are arbitrary[6].*

magnetization **M** is given by the relation:

$$\mathbf{B} = \mu_0(\mathbf{H} + \mathbf{M}), \tag{1.13}$$

where μ_0 is the permeability in free space. The magnetization **M** is proportional to the applied magnetic field **H**

$$\mathbf{M} = \chi\mathbf{H}, \tag{1.14}$$

where χ is the magnetic susceptibility. It describes the response of a material to the applied magnetic field. The coupling between the magnetic moments in solids and the applied magnetic field can arise through different behaviors in these solids.

1.2.2 Paramagnetism

Paramagnetism occurs in materials whose molecules have permanent magnetic dipoles moments due to the intrinsic magnetic moments of unpaired electrons. These dipoles interact only weakly with each other and are randomly oriented in the absence of an external magnetic field. When the material is placed in an external field, its atomic dipoles tend to line up with the field. However, this alignment process must compete with the effects of thermal motion, which tends to randomize the dipole orientations.

Many paramagnetic substances obey Curie's law especially at high temperatures. This states that the magnetic susceptibility is inversely proportional to the temperature

$$\chi = \frac{C}{T}, \tag{1.15}$$

where C is the Curie constant. Often, however, a better fit to the experimental data is provided by the Curie-Weiss law

$$\chi = \frac{C}{T + \theta}, \tag{1.16}$$

where θ is the Weiss constant. These two types of behaviour are shown in **Figure 1.9** in which χ^{-1} is plotted against T. In **Figure 1.10(a)**, a schematic plot of susceptibility

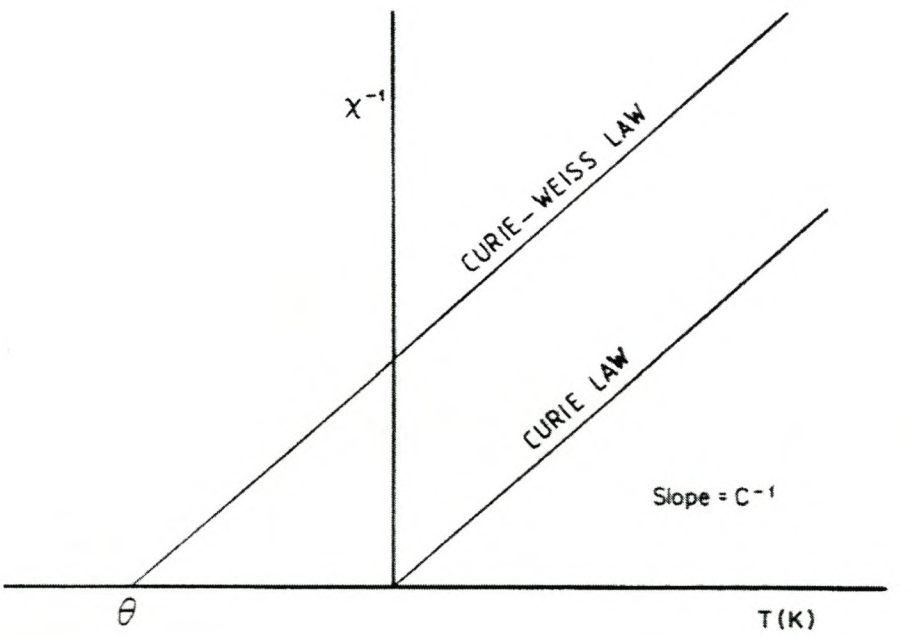

Figure 1.9: *Plot of reciprocal susceptibility versus temperature showing Curie and Curie-Weiss law behaviour[7].*

as function of temperature is shown for paramagnetic materials. Their susceptibility is positive but small ($0 < \chi \ll 1$).

1.2.3 Ferromagnetism

Below a transition temperature T_c called the Curie temperature, ferromagnetic materials undergo a spontaneous orientation of spins which leads to large magnetic effects. For ferromagnetic materials, the temperature dependence of χ does not fit the Curie/Curie-Weiss laws as shown schematically in **Figure 1.10(b)**. Ferromagnetic materials show a very large susceptibility at low temperatures that decreases increasingly rapidly with rising temperature. Above the Curie temperature, the material is no longer ferromagnetic but reverts to paramagnetic. In ferromagnetic materials, the electron spins are aligned parallel due to the cooperative interactions between spins on neighbouring ions in the crystal structure.

1.2.4 Antiferromagnetism

When the alignment of the spin moments of neighboring atoms or ions are exactly in opposite directions, the phenomenon is called antiferromagnetism. For antiferromagnetic materials, the value of χ increases with rising temperature up to a critical temperature, known as the Neel point, T_N. Above T_N, the material reverts to paramagnetic behaviour (see **Figure 1.10(c)**).

1.2.5 Ferrimagnetism

Ferrimagnetism is another prevalent type of ordering of the magnetic moments besides ferromagnetism and antiferromagnetism. In ferrimagnetic materials, although the individual magnetic moments of adjacent atomic particles are aligned antiparallel, they are not of equal magnitude. The prototype known ferrite is Fe_3O_4, sometimes called lodestone. This formula may be written as $Fe^{2+}O^{2-}$-$(Fe^{3+})_2(O^{2-})_3$ in which the Fe ions exist in both +2 and +3 valence states in the ratio 1:2. A net spin magnetic moment exists for each Fe^{2+} and Fe^{3+} ion. Furthermore , the O^{2-} ions are magnetically neutral. Antiparallel spin-coupling interaction exists between the Fe ions, similar in character to

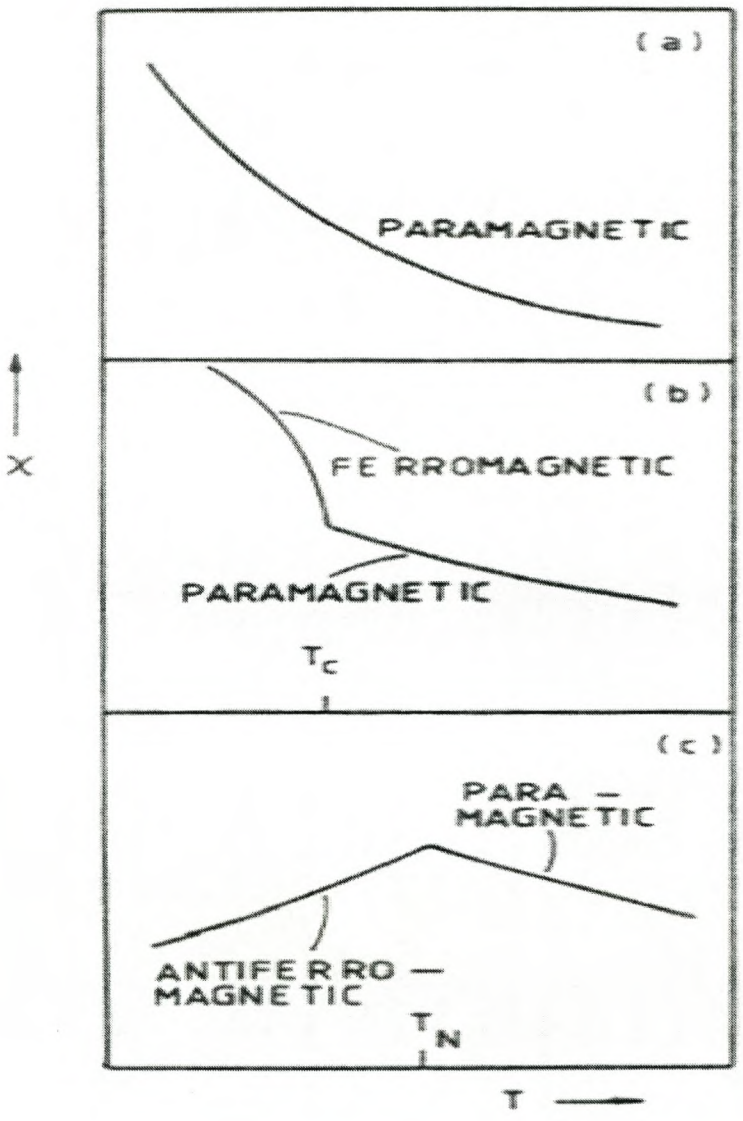

Figure 1.10: *Temperature dependence of the magnetic susceptibility for (a) paramagnetic, (b) ferromagnetic and (c) antiferromagnetic materials[7].*

antiferromagnetism. However, the net ferrimagnetic moment arises from the incomplete cancellation of spin moments.

1.2.6 Diamagnetism

Materials are diamagnetic when they exhibit a weak induced magnetization in the opposite direction to an applied field. In the presence of an external magnetic field, the electrons assume a precessional mode about the nucleus resulting in a magnetic moment that opposes the field. Diamagnetic materials have a small ($0 < \chi \ll 1$) but negative susceptibility and their magnetization is independent of temperature, unlike paramagnetism, ferromagnetism, and antiferromagnetism. Diamagnetism is a property of all material. It can be observed only in the absence of other masking effects, actually in insulators composed of atoms or ions with all electronic shells filled.

1.3 Magnetoresistivity

1.3.1 Introduction

Certain types of materials exhibit extreme changes in electrical resistivity when they are subjected to a magnetic field. This effect, called magnetoresistivity attracted much interest because of potential applications especially in magnetic recording and magnetic sensors that they can provide. During the discovery of magnetoresistivity (MR), the effects grew in strength and were progressively named anisotropic magnetoresistivity (AMR), giant magnetoresistance (GMR), and colossal magnetoresistance (CMR). Some authors define magnetoresistivity as

$$MR(\%) = \frac{\Delta R}{R(0)} \times 100\% = \frac{R(H) - R(0)}{R(0)} \times 100\%, \tag{1.17}$$

others as

$$MR(\%) = \frac{\Delta R}{R(H)} \times 100\% = \frac{R(H) - R(0)}{R(H)} \times 100\%, \tag{1.18}$$

where *R(H)* and *R(0)* are the resistances at a given temperature in the presence and absence of a magnetic field, respectively. In the second case the magnitude of negative magnetoresistance is very large compared to the first case. The approximate magnitudes of various types of magnetoresistance are shown in **Table 1.2**[8] where the equation 1.18 is used. Magnetoresistance can be positive $R(0) < R(H)$ or negative, e.g., $R(0) > R(H)$. In non-magnetic pure metals and alloys MR is generally positive and it shows a quadratic dependence on H. MR is usually negative in magnetic materials because of the suppression of disorder by the magnetic field.

Table 1.2: *The approximate magnitudes of different types of magnetoresistivity[8].*

Type of MR	Magnitude
Magnetoresistivity (MR)	1%
Giant magnetoresistivity (GMR)	200%
Colossal magnetoresistivity (CMR)	100,000%

1.3.2 Giant magnetoresistivity (GMR)

Giant magnetoresistance was discovered in 1988 by two European scientists Peter Gruenberg and Albert Fert, working independently[9,10]. The effect is most usually seen in magnetic multilayered structures, where two magnetic layers are closely separated by a thin spacer layer a few nm thick. **Figure 1.11** shows layers of cobalt and copper with the magnetizations of the cobalt layers in the opposite and same directions. GMR is analogous to a polarisation experiment, where aligned polarisers allow light to pass through, but crossed polarisers not. The first magnetic layer allows electrons of only one spin state

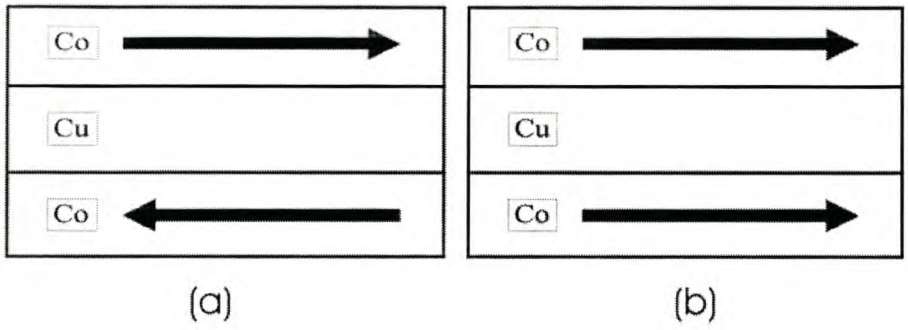

Figure 1.11: *Schematic representation of a stack of layers (two ferromagnetic layers are separated by a nonmagnetic thin spacer layer). The thickness of Co is* $\approx$ *11 Å and the thickness of Cu is* $\approx$ *9 Å.*

to pass through easily if the second magnetic layer is aligned to the first. As a result, the resistance of the structure will be low. If the second magnetic layer is misaligned then neither spin channel can get through the structure easily and the electrical resistance is high. The schematic diagram is represented in **Figure 1.12**. In the two-current model

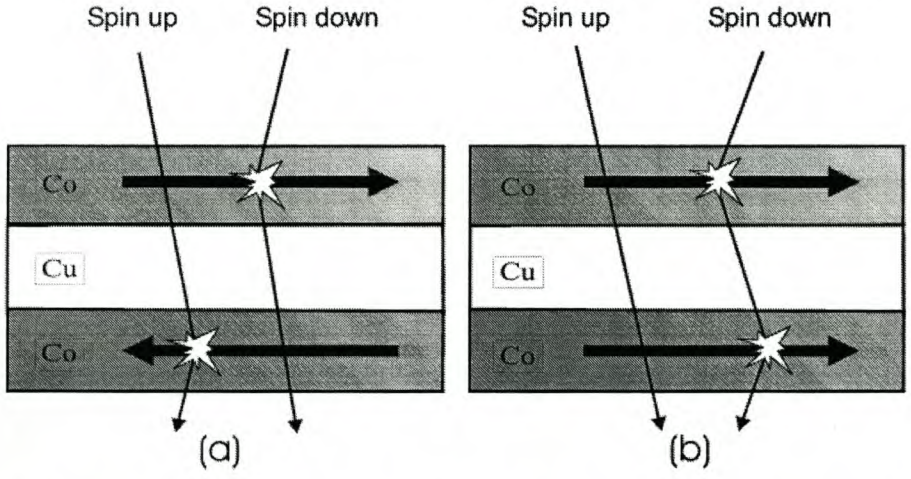

Figure 1.12: *Schematic diagram of spin-dependent electron scattering for antiparallel and parallel alignment of magnetic thin films.*

the electrical current in the stack of layers is divided into two currents resulting from spin-up and spin-down electrons. These two types of electrons have different scattering

probabilities at the interfaces and in the bulk of layers, due to a spin-dependent potential landscape and differences in the density of states at the Fermi level. In general an electron will have a higher scattering probability when its spin direction is opposite to the local magnetization direction[11]. The spin-up acts as a shunting current, which lowers the resistivity of the complete stack of layers considerably as compared to the situation when the magnetic moments are antiparallel. As of early 2000, IBM has already produced GMR heads in the lab capable of 35 GB/in^2, suggesting that hard disks of 200 GB or more are just around the corner[12].

1.3.3 Colossal magnetoresistivity (CMR) in manganite materials

Mixed valence manganites with the perovskite structure (same structure as of the mineral $CaTiO_3$) have been studied for almost 50 years. Manganites are of type $A_{1-x}B_xMnO_3$ where (A = La, Pr, or Nd), (B = Ca, Ba, Sr, or Pb), and x is the concentration of B varying over a wide range $0 \leq x \leq 1$. Interest in mixed-valence manganites revived in the 1990s following the preparation of high-quality thin films with large negative magnetoresistance by Von Helmholt *et al.*[13] and Chahara *et al.*[14] using a method employed for high-temperature superconductors, to which the manganites are structurally related.

This family of compounds offers a degree of chemical flexibility which permits the relation between the oxides' structure, electronic and magnetic properties to be examined in a systematic way. Their rich electronic phase diagrams (see **Figure 1.13**) reflect the fine balance of interactions which determine the electronic state. Depending on the composition, manganites show a variety of magnetic and electric phenomena, including ferromagnetic, antiferromagnetic, charge, and orbital ordering. Research on the manganites has revealed new phenomena such as colossal[16] and granular magnetoresistance (drop of resistance under magnetic field)[17], and has led to the formulation of important physical concepts such as double exchange [18,19] and the Jahn-Teller polaron[20,21]. The magnitude of MR in these materials can be very large, close to 10^5 % as per equation 1.18. For this reason, many scientists prefer to call this phenomenon colossal magnetoresistance

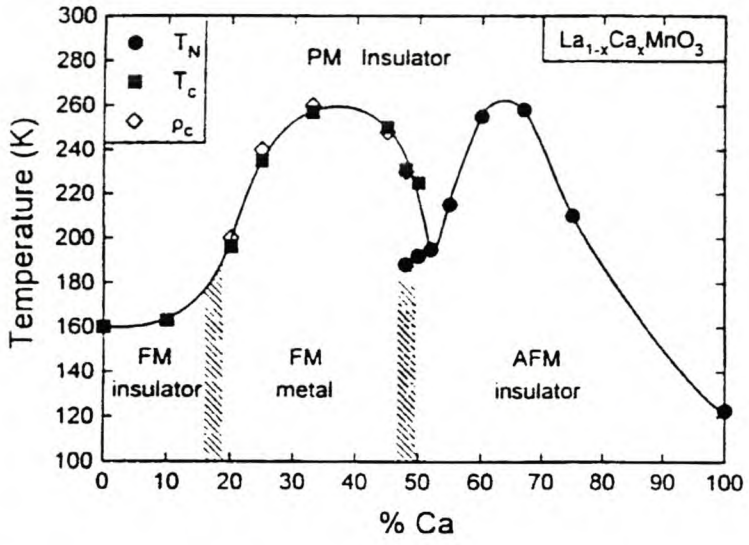

Figure 1.13: *Phase diagram of magnetic and transport properties of the series* $La_{1-x}Ca_xMnO_3$. *FM stands for ferromagnetic; PM stands for paramagnetic and AFM stands for antiferromagnetic[15](see* **Appendix A***: Definition terms and symbols.)*

(CMR), as distinct to GMR in layered or granular metallic materials which magnitude is very much lower than 10^5 %. **Figure 1.14** shows one typical plot of the resistance as a function of magnetic field; the magnetoresistance MR value much larger than 10^5 % at a temperature of 77 K, and a magnetic field of 5 T. Early research was motivated by a need to develop insulating ferromagnets with a large magnetization for high frequency applications. More recent work has been driven by a desire to understand and exploit the large negative colossal magnetoresistance effects which appear near and below the Curie temperature. The manganite perovskites also have potential as electrolytes, catalysts, magnetoresistive sensors, magnetoresistive read heads, magnetoresistive random memory (MRAM) and novel electronic materials. The mixed-valence oxides $La_{1-x}Ca_xMnO_3$ (the system investigated in this study) can be regarded as solid solutions between end members $LaMnO_3$ and $CaMnO_3$ with formal valence states $La^{3+}Mn^{3+}O_3^{2-}$ and $Ca^{2+}Mn^{4+}O_3^{2-}$, leading to mixed valence compounds such as $(La_{1-x}^{3+}Ca_x^{2+})(Mn_{1-x}^{3+}Mn_x^{4+})O_3$. The ending compounds are antiferromagnetic at low temperatures and insulator in the whole range of temperatures. The region $x < 0.2$ was initially reported as ferromagnetic insulator

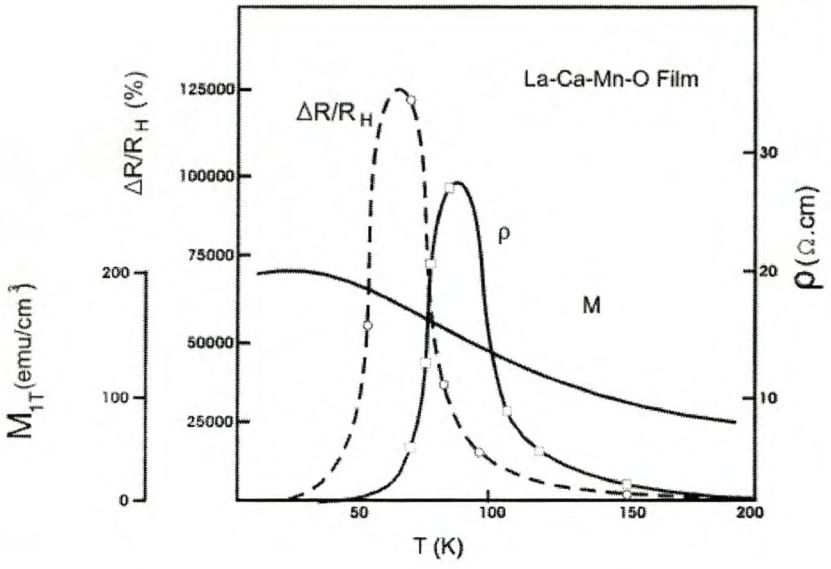

Figure 1.14: *Resistivity (ρ), magnetoresistance ($\Delta R/R_H$), and magnetization (M) versus temperature for a magnetic field of 5 tesla(adapted from Jin et al[15]).*

[15] but subsequent experiments[22,23] proved that the ferromagnetic region is restricted to the concentration range $0.2 \leq x \leq 0.5$. In this intermediate doping range, a large magnetoresistance (colossal magnetoresistance) was observed[16].

Crystal structure of manganites

The manganites crystallize in the cubic perovskite structure ABO_3. A good way to regard the structure is as a cubic close-packed array formed of O^{2-} anions and large A cations, with the small B cations in the octahedral interstitial sites **Figure 1.15 (a).** The second way is to put the La atoms at the centre and surround it by the eight Mn atoms in the corners **Figure 1.15 (b)**. This ideal structure is distorted by cation mismatch and the Jahn Teller effect, whereby a distortion of the oxygen octahedron surrounding the B cation splits the energy levels of a 3d ion such as Mn^{3+}, thus lowering the energy and giving rise to long and short bonds. The distorted structures are frequently orthorhombic

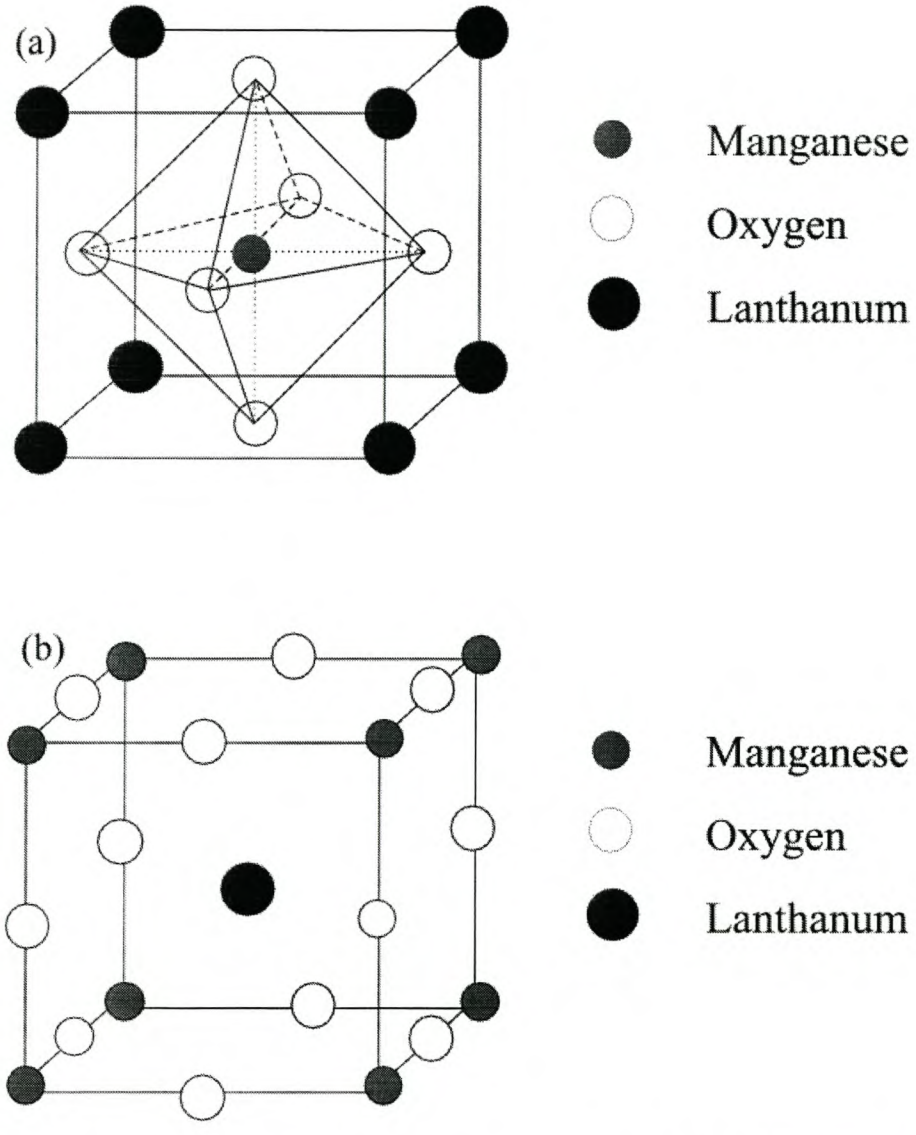

Figure 1.15: *Structure of perovskite manganites. (a) Cubic perovskite unit cell centered at Mn, and MnO octahedron. A MnO_6 octahedron of one particular cube with the Mn atom at the centre is connected to the adjacent octahedra by the common oxygen vertices. (b) Cubic perovskite unit cell: La atom is at the centre and surrounded by eight Mn atoms in the corners. Oxygen atoms are in the middle of each cubic edge between two Mn nearest neighbours.*

and is characterized by the Goldsmith tolerance factor[24], defined as

$$t = \frac{d_{A-O}}{\sqrt{2}(d_{Mn-O})}, \tag{1.19}$$

where d_{A-O} and d_{Mn-O} are the average A cation-oxygen and manganese-oxygen distances respectively. In the case of an ideal cubic perovskite, $t = 1$. Normally the perovskite structure may form in oxides for which $0.89 < t < 1.02$. The geometry of the Mn-Mn bond plays a crucial role since the oxygen ion mediates the double exchange. In an ideal perovskite structure, the Mn ions occupy the centers of the oxygen octahedrons with 180^0 Mn-O-Mn bond angle. Distortion of the crystal structure results in buckling of the octahedral network, thereby altering the Mn-O-Mn bond angle and bond distance, affecting the electron hopping probability and the double-exchange interaction.

Hole-doped manganates

The perovskite manganate $LaMnO_3$ is an insulator at all temperatures and undergoes an antiferromagnetic transition with a Neel temperature, $T_N \sim 150K$. When the La^{3+} in $LaMnO_3$ is progressively substituted by a divalent cation as $La_{1-x}A_xMnO_3$ (A= Ca, Sr or Ba), the proportion of Mn^{4+} increases and the orthorhombic structure decreases. At a certain concentration x, the material becomes ferromagnetic with a well-defined Curie temperature T_c. Below T_c, the manganates exhibit metal-like conductivity . This simultaneous observation of itinerant electron behavior and ferromagnetism in the manganates compound is explained by Zener's double-exchange mechanism[18]. The basic process in this mechanism is the hopping of a d-hole from $Mn^{4+}(d^3, t_{2g}^3, S = 3/2)$ to $Mn^{3+}(d^4, t_{2g}^3 e_g^1, S = 2)$ via the oxygen, so that the Mn^{4+} and Mn^{3+} change places: $Mn^{3+}O^{2-}Mn^{4+} \rightarrow Mn^{4+}O^{2-}Mn^{3+}$ This situation involves the transfer of an electron from the Mn^{3+} site to the central oxide ion and simultaneously the transfer of an electron from the oxide ion to the Mn^{4+} site. Such transfer is referred to as double-exchange (DE). It is a maximum when the magnetic moments of the manganese ions (Mn^{3+} and Mn^{4+}) are aligned parallel and a minimum where they are aligned antiparallel. Thus, the mechanism which leads to enhanced electrical conductivity requires a ferromagnetic

coupling. The relation between the electrical conductivity and ferromagnetism by the DE mechanism as originally proposed by Zener is obtained from the following expressions: The magnitude of the exchange energy,ϵ, is given by

$$\epsilon = \frac{h\nu}{2}, \tag{1.20}$$

where ν is the frequency of oscillation of the electron between the two Mn sites. The diffusion coefficient for an Mn^{4+} ion is defined by

$$D = \frac{a^2\epsilon}{h}, \tag{1.21}$$

where a is the lattice parameter. Making use of the Einstein equation relating conductivity, σ and D, $\sigma = ne^2D/kT$, where n is the number of Mn^{4+} ions per unit volume, we obtain

$$\sigma = \frac{xe^2D}{kT}. \tag{1.22}$$

Since the ferromagnetic Curie temperature T_c is related to the exchange energy by the approximative relation, $\epsilon \approx kT_c$, we obtain the following expression for the electrical conductivity:

$$\sigma \approx \left(\frac{xe^2}{ah}\right)\left(\frac{T_c}{T}\right), \tag{1.23}$$

where x is the fraction of Mn^{4+} ions in $La_{1-x}A_xMnO_3$. Double-exchange is strongly affected by structural parameters such as the Mn-O-Mn angle or the Mn-Mn transfer integral. Analogous to the perpendicular conduction of electrons in GMR, the electron that hops away from the Mn^{3+} remembers the spin state it had on the ion as determined by Hund's rule on the Mn^{4+}, if the net ions spins of the neighboring Mn^{3+} and Mn^{4+} are in the same direction[25]. Thus, the resistance of the material becomes a function of its intrinsic magnetic order. Usually the compounds show metallic behavior in the ferromagnetic region and insulator-like in the paramagnetic region. There also exists a critical average size of the interpolated cation below which the CMR property cannot be observed. The essential consequence of the double exchange is the formation of Jahn-

Teller polarons, a process that tends to localize the electrons. The Mn provides the effective spins and the local Jahn-Teller distortion. The Jahn-Teller distortion provides strong electron-phonon coupling, lifting the double degeneracy of the energy orbitals, while preserving the total orbital energy[26].

Crystal field theory in transition metals

Manganese ($[Ar]3d^5)4s^2$ and Iron ($[Ar]3d^64s^2$ are part of the group of transition metals. In transitions metal compounds, the majority of the d electrons on the metal atom do not usually take part in bond formation but do influence the coordination environment of the metal atom and are responsible for properties such as magnetism. In an octahedral environment, the five d orbitals on a transition metal are no longer degenerate but split in two groups, the t_{2g} group of lower energy and the e_g group of higher energy. The extent to which these two sets of orbitals are split is denoted by Δ or alternatively $10D_q$ as shown in **Figure 1.16.** From d^4 (Mn^{3+},Cr^{2+}) to d^7 (Co^{2+}) atoms or ions,

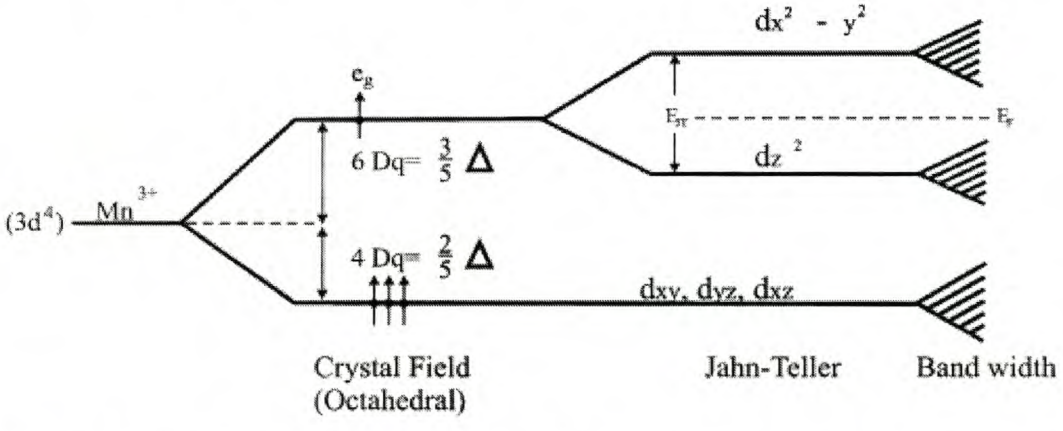

Figure 1.16: *Energy level diagram for d-levels in a d^4 ion experiencing a Jahn-Teller effect. The Fermi level lies between JT split orbitals (adapted from Ref[27,28]).*

two possible configurations occur, giving low spin (LS) and high spin (HS) states. The increased energy, Δ, required to place an electron in an e_g orbital, and hence maximize the multiplicity, has to be balanced against the repulsive energy or pairing energy, P, which arises when two electrons occupy the same t_{2g} orbital. In many transition metal

compounds, the metal coordination is distorted octahedral and distortions are such that the two axial bonds are either shorter than or longer than the other bonds. The Jahn-Teller effect is responsible for these distortions in d^9, $d^7(LS)$ and $d^4(HS)$ which have odd numbers of e_g electrons. The Jahn-Teller theorem states that any non-linear molecular system in a degenerate electronic state will be unstable and will undergo distortion to form a system of lower symmetry and low energy thereby removing the degeneracy. For instance, in $Mn^{3+}[(t_{2g})^4(e_g)^1]$, the e_g orbitals contain one electron and the t_{2g} contain four electrons. The singly occupied orbital can be either d_{z^2} or $d_{x^2-y^2}$ and in a free situation both would have the same energy. However, since the metal coordination is octahedral, the e_g levels are no longer degenerate. The e_g orbitals are higher energy orbitals than the t_{2g} since they point directly towards the surrounding ligands. The single occupied orbital will experience stronger repulsions and this has the effect of lengthening the metal-ligand bonds in the direction of the single occupied orbital.

1.3.4 Summary

The existence of Mn^{4+} ions in hole doped manganites and the double-exchange provide a link between charge transport and magnetization in CMR materials. The aforementioned strong Hund coupling makes the charge transfer possible between the neighbouring Mn^{3+}/Mn^{4+} ions if the spin of the e_g electron of the Mn^{3+} is aligned with the spin of the Mn^{4+}. Anderson and Hasegawa[29] and de Gennes[30] established that the effective transfer integral of an e_g electron to the next Mn neighbour depends on the angle between the local t_{2g} moments. If they are parallel, the electron will be easily transferred. The ferromagnetic order is consequently related to a large electronic itinerancy, i.e metallic behaviour.

The doping of manganites by iron is also susceptible to enhance the CMR effect in the manganites. This is the case of the perovskite $La_{0.67}Ca_{0.33}Mn_{0.9}Fe_{0.1}O_3$. This compound has been confirmed to exhibit spin-glass behaviour meanwhile the metal-insulator and CMR effects have also been observed near its spin freezing temperature, besides

which the insulator behaviour has been found to reappear at lower temperature[31]. It is also noted that, upon Fe doping, the large negative magnetoresistance is dramatically enhanced in the perovskite $La_{0.63}Ca_{0.37}Mn_{1-x}Fe_xO_3$. For the undoped sample (x=0), CMR of 120% is observed near T_c. For x=0.08, a 5 T field reduces ρ by one order of magnitude. For x=0.12, the CMR effect increases to three orders of magnitude. However, further doping to x=0.18 shows insulating behaviour in the whole temperature range, with or without a 5 T field, although a sizable MR remains[25]

1.4 Pulsed Laser Deposition (PLD)

1.4.1 History

PLD involves the interaction of a focussed high power laser pulse with a multicomponent solid target material. Material ablated from the target forms a fast moving plume consisting of atomic and molecular particles, directed away from the target, and towards a usually heated substrate on which the particles condense to form a thin film. The substrate temperature and background gas are carefully controlled to be conducive to the growth of a desired phase of multi-elemental compound.

The use of lasers to ablate material has to be traced back to 1962 when Breech and Cross[32], used a ruby laser to excite and vaporize atoms from solid surfaces. Throughout 1963 and 1964, about two dozen publications detailed the early experiments on laser ablation. The first experiment demonstrating the laser deposition of thin films was performed by Smith and Turner[33] in 1965, also by using a ruby laser. This marked the beginning of the development of the pulsed laser deposition technique. The seventies represent a time of expanded uses of laser ablation for analysis of various materials and also more detailed studies of the physics of the ablation. The thin film development was still slow, hampered by the poor quality of the films. Most progress in the seventies concentrated on plume diagnostics (mass and charge dependence of the ejected plume) and

model development. The growth of literature on laser ablation in the eighties has been explosive. This growth is based on two factors:

1. The expansion and integration of laser technology into virtually every scientific laboratory;

2. The increased number and importance of various applications.

During this decade, picosecond lasers became common and femtosecond lasers emerged. Tunable lasers expanded their range into the ultraviolet and infrared. Besides Nd:YAG and CO_2 lasers, excimer lasers delivering ultra-violet radiation were also used in the deposition of thin films. The development of the films grown by laser ablation reached a very interesting level and attained its reputed fame with the advent of high T_c superconductors[34]. Since the successful deposition and growth of high T_c superconducting thin films in 1987, pulsed laser deposition has attracted widespread interest in the research community. To date, it remains the efficient technique to fabricate crystalline thin films with epitaxy quality of materials. It has been demonstrated that the composition of rather complex multi-elementary materials can be reproduced in the film under appropriate conditions of laser-energy density and deposition angle with respect to the target surface normal[35].

1.4.2 Mechanisms

On the basis of the review papers by D.H. Lowndes[36] and D.G. Geohegan[37], the laser ablation can be thought of occurring through three main mechanisms:

1. The evaporation of surface layers during the early part of the pulse.
   The interaction of a laser pulse with the target is primarily determined by the laser energy density. Two thresholds can be identified: the first is the threshold for laser ablation (the energy density where measurable material removal starts) and the plume threshold. The evaporation threshold can be understood by the

exponential increase in the vapour pressure with temperature predicted by the Clausius-Clapeyron equation. At a certain laser density, the rapid laser heating rates ($\sim 10^{11} K s^{-1}$) overcome the thermal diffusion and radiation losses and evaporation proceeds nonlinearly. The evaporants consist of atoms, ions, molecules, clusters, and fragments.

2. Plasma heating

   Heating of the plasma is thought to occur via inverse-Bremsstrahlung absorption of the laser light in electron-ion pairs[38,39]. Emission spectroscopy of plasmas during the initial expansion indicate typical temperatures of $\sim$ 10000 K, well above the boiling points of most materials. Thus during $\sim$ 30 ns, a high pressure ($\sim$ 10-500 atm.) bubble of hot plasma is formed $\leq 50\mu$m from the target. Using time-of-flight mass spectroscopy, C.H. Becker *et al*[40] found that by increasing the laser fluence from 2.5 J/cm^2 to 4.3 J/cm^2 resulted in a marked decrease in clusters of size $\geq$ 100 nm; at 4.3 J/cm^2 the amount was less than 10 % of the number at 2.5 J/cm^2. This indicates that the intense focussed excimer beam is very efficient in photodissociating the clusters to produce smaller mass ions.

3. Expansion of the plume

   - Foward directionality

     The expansion of the bubble produces a supersonic beam. It is important to have the correct picture of the shape of the plasma bubble the moment that the laser pulse ended. The transverse dimensions are given by the laser spot size (typically 2-3 mm), but in the direction perpendicular to the target, the initial plasma dimensions are only tens of micrometers. Thus, the high temperature plasma would start expanding and since there are no impediments to move away from the target, the plasma rapidly expands in the forward direction, giving rise to the well known forward directed plume (see **Figure 1.17**). Atoms and ions attempting to move parallel to the target would undergo frequent scattering, due to the high density of the material in the parallel

direction. Thus, the plume rapidly expands away from the target, causing the characteristic forward peaking.

- Angular distribution of ablated species

  The angular distribution of the source f(θ) of atoms in the plume is usually of the form

$$f(\theta) \propto \cos^p \theta. \tag{1.24}$$

  This results in a film thickness profile of

$$T(\theta) \propto \cos^{p+3} \theta, \tag{1.25}$$

  the extra $\cos^3 \theta$ resulting since the flux emitted into a solid angle element $d\Omega$ would be deposited on a substrate area element $dA = D^2 \frac{d\Omega}{\cos^3 \theta}$, D being the target-substrate distance[41]. A well established, but initially counter-intuitive result is that the film thickness profile T(θ), becomes more sharply forward peaked as the spot size increases. R.E. Muencheusen *et al*[42] pointed out that a large diameter laser spot and a smaller laser spot scanned over the same area result in different angular distributions, the large spot area giving rise to a more forward peaked plume. Also, less peaking can be achieved by focusing the beam sharper or by decreasing the oxygen pressure slightly. When depositing lead and tungsten, A.D. Akhsakhalyan *et al*[43] found that p$\sim$ 7 when the spot size was $\leq$ 200 μm (diameter) while p $\sim$ 23 when the spot size was increased to $\sim$ 2 mm (diameter). Thus, if the focussed laser spot is initially longer in the horizontal direction, the film will be elongated in the vertical direction.

- Control of kinetic energy by gas-phase collisions

  In order to grow epitaxial thin films on crystalline substrates, the ablated species should have sufficient kinetic energy to break bonds in the surface layer to facilitate the formation of a crystalline structure at low substrate temperature. Where the substrate would allow heating to higher temperatures,

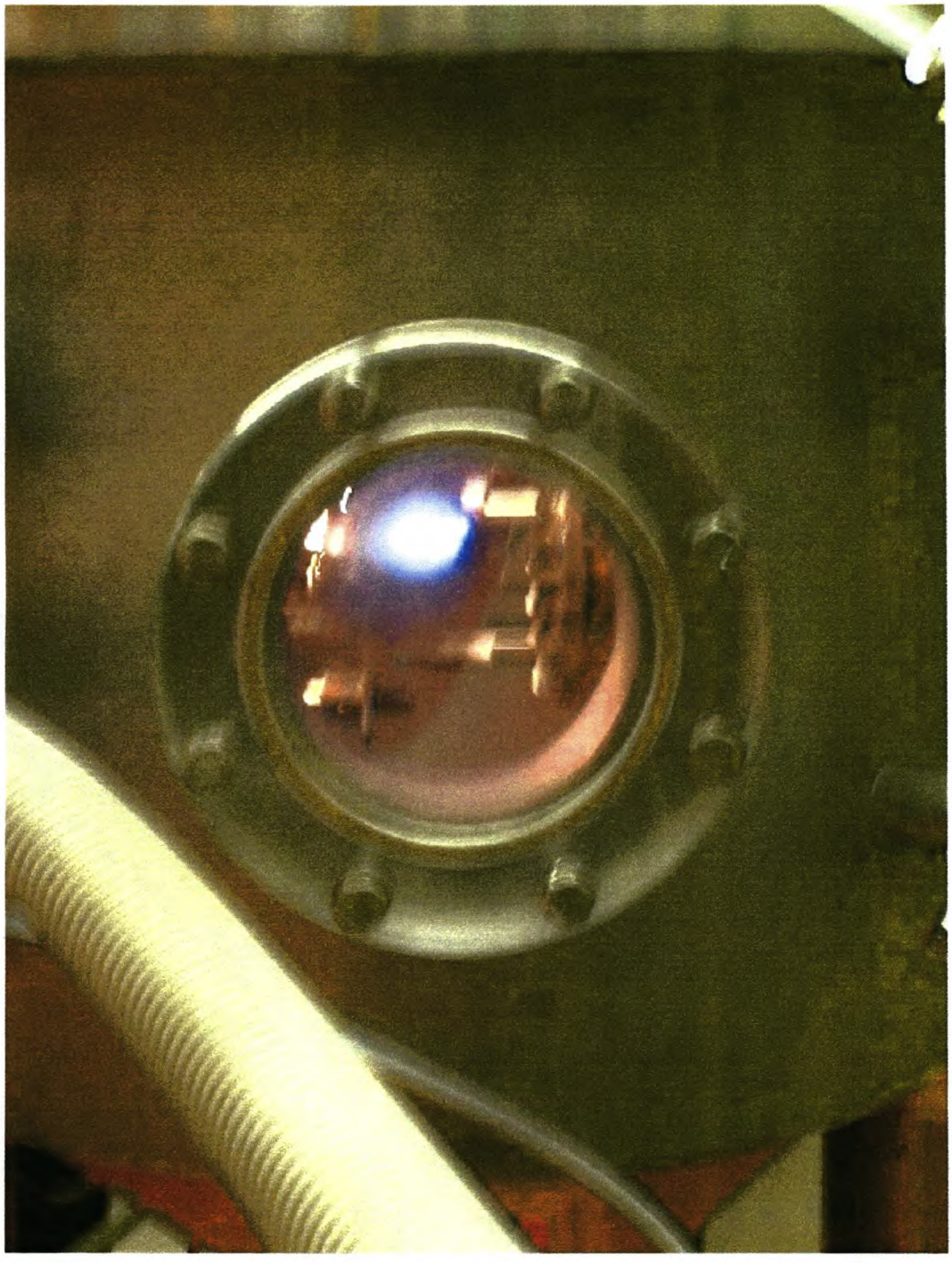

Figure 1.17: *Photograph of the forward peaked plume produced by laser ablation of* $La_{0.67}Ca_{0.33}Mn_{0.98}Fe_{0.02}O_3$ *target in an oxygen ambient pressureof 0.5 mbar at the Laser Research Institute of the Physics Department, University of Stellenbosch. On the left is the substrate holder and on the right the target holder. The target is rotating whereas the substrate is fixed and heated at* 750^0C *during ablation.*

without causing reaction with the ambient gas or the deposited species, the higher temperature would also facilitate the breaking of bonds necessary for the formation of an epitaxial layer. At higher energies the ablated species can produce deeper lattice displacements, causing structural defects like excessive grain boundaries and misorientation in the film. The optimum kinetic energy appears to be ≤ 20 eV. Ambient gas, together with the substrate distance can be used to moderate the kinetic energy of the ablated material, via gas-phase collisions. At sufficiently high pressures, the gas-phase collisions completely thermalise the initial kinetic energy of the ablated material so that it is not delivered to the growing film surface.

1.4.3 Advantages and disadvantages of PLD

Advantages

1. The fast response due to extremely short pulses (each less than 50 ns).
2. The high energy of the the ablated species (evaporants) can enhance the quality of film growth.
3. The ability to accurately replicate the stoichiometry of the ablated target within the laser-deposited thin film.
4. PLD does not require hot filaments and therefore allows a number of reactive gases to be present in the chamber during deposition.
5. The chamber-pressure, the target-substrate distance, the target orientation with respect to the beam are significantly decoupled, enabling a greater degree of freedom during the deposition.
6. The fabrication of multi-layers is fairly straightforward with rapid substitution of targets into the path of the laser beam. Most materials have a fairly common

range of evaporation parameters, therefore, it is relatively easy to design automated systems capable of sophisticated thin film structures.

Disadvantages

There are two major drawbacks of PLD:

1. The lack of uniformity over a large area due to a narrow angular distribution(forward peaking) of the plume.
2. Splashing (deposition of particulates onto the substrate).

Three mechanisms lead to splashing:

- Surface boiling

It occurs if the time required to transfer laser energy into heat is shorter than that needed to evaporate a surface layer with a thickness on the order of skin depth. Under this condition, the subsurface layer is superheated before the surface itself has reached the vapor phase. This process will expel micro-sized molten globules onto the substrate.

- Expulsion of the liquid layer by the shock wave recoil pressure

In this mechanism, the force that causes the splashing explosion comes from above the liquid layer in a form of recoil pressure exerted by the shock wave of the plume. The signature of this type of splashing is also the formation of micro-sized condensed globules onto the substrate.

- Exfoliation

Exfoliation occurs when materials ejected from the target are randomly shaped solid particulates. The rate of ejection and the particulate size depend on the laser power

density as well as the surface morphology of the target. For most materials, the surface is eroded by repetitive laser ablation, forming long needle-shaped microstructures of only a few microns in dimension. These microdendritic structures point toward the direction of the incoming laser beam due to the shadowing effect. Mechanically, they are very fragile and can be broken by the thermal shock induced during the intense laser radiation. The loose debris is carried toward the substrate by the rapidly expanding plume and condenses on it.

1.4.4 New advances

The lack of uniformity over a large area due to the small size of the ablation plume (film area typically $<1\ cm^2$) and forward peaking is one of the main disadvantages of pulsed laser deposition. To overcome this problem, new techniques using rotation and translation, by rastering the laser or the substrate are now under investigation. The techniques include off-axis target, rotational-translational PLD, and laser beam scanning **(Figures 1.18 (a),(b),(c))**. Researchers think that the combination of the above techniques could offer thin films with structural and thickness uniformity. Other possibilities are:

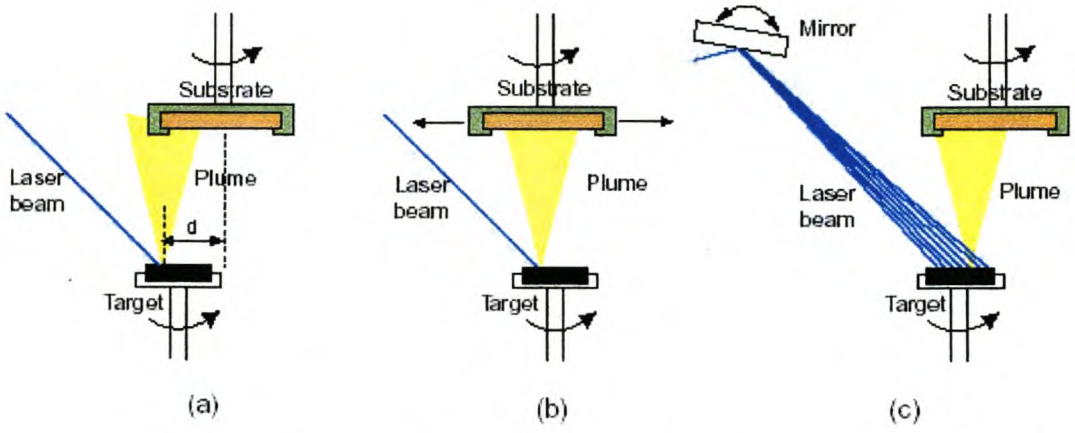

Figure 1.18: *Three techniques to increase the thin film area. (a) off-axis PLD. (b) rotational-translational PLD. (c) laser-beam scanning.*

1. Target wobbling

   The target is mounted such that a small angle is formed between the target and the axis of rotation.

   Thus, one can get a continuous change in the plume direction **(Figure 1.19)**.

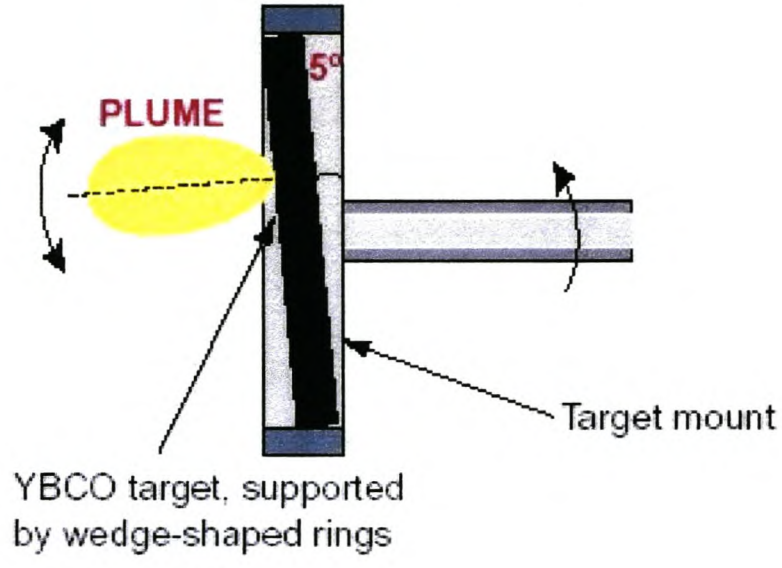

Figure 1.19: *For target wobbling, the target makes a* 5^0 *angle with the axis of rotation.*

2. Off-axis PLD with aperturing

   The plume has a 7 mm offset from the center of the substrate plate. The plume edges are apertured in front of the substrate **(Figure 1.20)**.

3. Large target-substrate

   The target-substrate distance can be increased from the present typically 60 mm up to 100 mm. As result, 70-mm diameter can be uniformly coated (**Figure 1.21**).

Other advances are oriented in the plume monitoring. One group of researchers at Oak Ridge National Laboratories (ORNL)[44] are investigating how one can get a thin film of

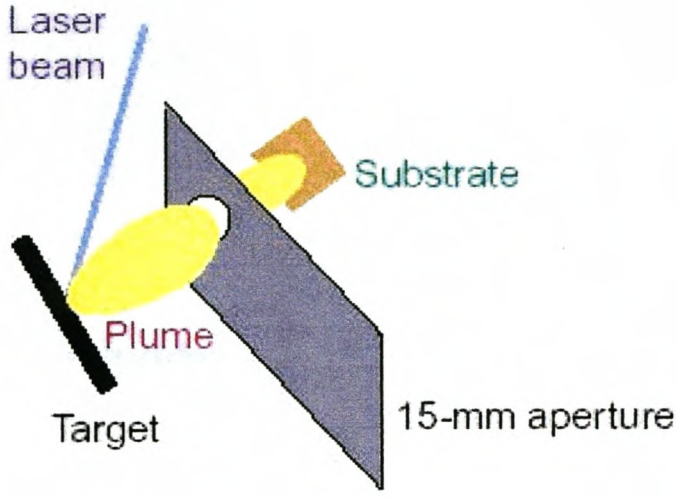

Figure 1.20: *Schematic of the plume path towards the substrate through the aperture of 15 mm. The aperture is close to the substrate.*

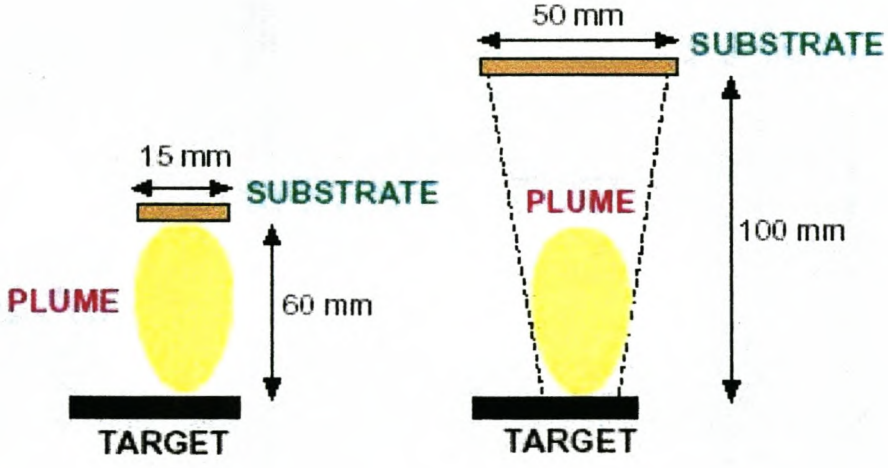

Figure 1.21: *Effect of increasing the substrate-target distance on the deposition thin film. With a substrate-target distance of 100 mm, the size of the thin film is increased more than three times than the substrate-target distance of 60 mm.*

high quality by monitoring the plume. Their technique includes a fast-intensified charge-coupled detector camera to acquire images of the fluorescent plasma; optical emission and absorption spectroscopy that differentiate among the plume's atomic and molecular species and states; and an ion probe, which measures ion energy and plasma density. From these tools, scientists can learn how fast the plume is moving and how much material in different atomic forms is present in the plume's different parts. Then, it can be predicted whether the film being produced will be uniformly thick and can determine which conditions the laser beam energy and wavelength, gas pressure, substrate temperature have changed and how such change should be corrected to optimize film quality.

Another ORNL group of researchers[45] have designed a device that combines a laser, a rotating drum on which separate oxide targets could be mounted, a computer -controller that would select (or skip) each target and adjust the laser energy needed to ablate it as it rotated several times per second **(Figure 1.22)**. Such an automated device would switch targets for pulsed laser ablation much faster than manually operated mechanical shutters and could not only control stoichiometry but also add buffer layers and contact layers or construct multilayered structures with ease. The system is called LARES (Laser Ablation by Rapidly Exchanged Sources). It can be simply programmed for the desired composition, and the controller selects the proper targets and fires the laser with the correct energy to deliver the needed amount of each target material. Due to the speed and flexibility of this system, researchers can do material synthesis at least 10 times faster than previously.

Today PLD offers the fastest route to prototyping any thin-film coating. In fact, many multicomponent materials produced with PLD promise valuable applications. For instance, Superconducting quantum interference devices (SQUID's) are the result of PLD of high temperature superconductors. Barium strontium titanium oxide thin-films can be used in making very large scale integrated (VLSI) circuits, where the sizes of capacitors can be reduced dramatically. PLD-produced iron-oxide films may be used in magnetic

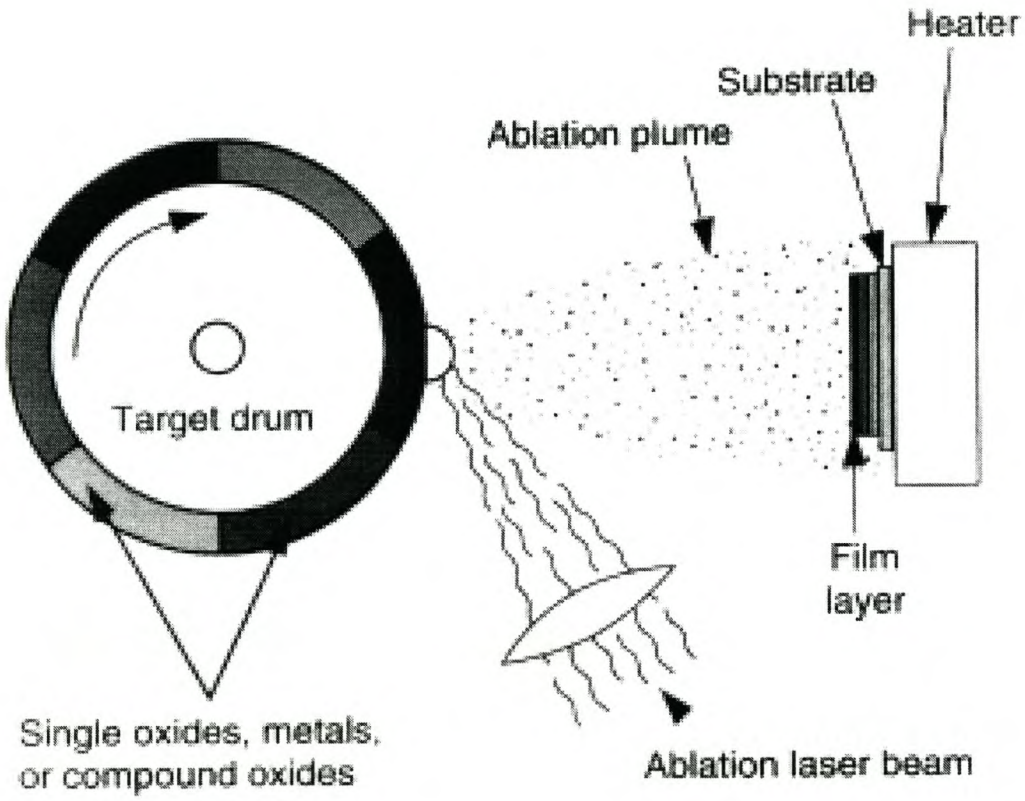

Figure 1.22: *Schematic of the LARES set-up. Six targets are mounted on the rotating drum. The pulsed laser strikes the drum at the same point, but because the drum is rotating, the laser ablates different targets at the appropriate energies. Repeated ablations of different targets materials result in the deposition of a thin film onto the substrate.*

recording. Optoelectronics applications can use thin films of lithium niobium oxide made with PLD. Many other PLD-produced thin films appear in devices for a variety of other technologies, including environmental sensors, micromechanical devices, light emitters, medical implants, and various coatings.

1.5 Scope of Investigation

Much of the exploration of the CMR materials has been done through the doping of the La sites, which brings about lattice effects, and ultimately influences the DE. Fewer studies have been devoted to Mn doping sites, which are playing a central role in the double exchange (DE). The objective of this work is to elucidate the role of the Mn ion on the CMR effect by replacing it with a similar transition metal, namely Fe in $La_{0.7}Ca_{0.3}Mn_{1-x}Fe_xO_3(LCMFO)(0 < x < 1)$. Early studies have shown that in this Fe(Mn) doping range, a direct replacement of Mn^{3+} by Fe^{3+} occurs. In addition, Mn^{3+} and Fe^{3+} have identical size. These conditions should enable us to bypass the strong lattice effects (as we are dealing with the same structures) and study the physical properties of the system of perovskites by investigating the electronic structure only. Referring to the previous work, high-quality thin film perovskites are a requirement to observe a large magnetoresistance effect. In addition, they exhibit a variety of transport and magnetic properties that sensitively depend on the composition, stoichiometry and structure of the materials. Extensive work of preparation, characterization and optimization of thin films of manganite perovskites LCMFO by pulsed laser deposition (PLD) from sintered ceramic targets has been carried out. Thin films were deposited on different single crystal substrates such as MgO, $LaAlO_3$, $SrTiO_3$ and Si.

This thesis is subdivided in six chapters. The introduction is given in **Chapter 1**, while the aim of **Chapter 2** is to discuss all the experimental methods employed to investigate LCMFO thin films deposited by PLD. This includes Rutherford backscattering spectroscopy (RBS), x-ray diffraction (XRD), atomic force microscopy (AFM), scanning

electron microscopy (SEM) and resistivity measurements. **Chapter 3** deals with modeling and simulation of the LaCaMn(Fe)O system, looking mainly at the thickness and the stoichiometry. The main purpose of **Chapter 4** is to investigate the oxygen uptake in $La_2CaMn_{3-x}Fe_xO_9$ films formed by PLD, while in **Chapter 5**, the results from the characterization of the samples are presented; RBS for sample thickness, AFM, SEM, and XRD for surface morphology, crystallinity and phase identification. Electrical and magnetic results are also presented. In **Chapter 6** a summary and conclusion of this investigation is given.

Chapter 2

Experimental Methods

2.1 Sample Preparation

$La_{0.67}Ca_{0.33}Mn_{0.98}Fe_{0.02}O_3$ and $La_{0.67}Ca_{0.33}Mn_{0.20}Fe_{0.80}O_3$ thin film structures were prepared by pulsed laser deposition. The substrates used: silicon $< 100 >$, perovskites $LaAlO_3$ and $SrTiO_3$, and MgO single crystals. The procedures for substrate preparation concerned only silicon substrates. $LaAlO_3$, $SrTiO_3$, and MgO substrates were used as they were from their packages. The substrate plays a key factor for the high quality of the thin film in the deposition process. The substrate should provide mechanical support but not interact with the film except for sufficient adhesion, and provide a template ordering. In practice, the substrate exerts considerable influence on film characteristics. The most important issues regarding substrate selection is discussed point by point[46]:

1. Chemical compatibility: Ideally there should be no chemical reactions between the film and the substrate. The relative high temperatures required for growing films make compatibility requirement more critical than it would be if the high quality film could be grown at lower temperatures. Thus, the substrate must be unreactive in the oxygen-rich ambient required for growth and processing. Oxide substrates are more likely to tolerate the growth requirements of CMR materials than non-oxide materials.

2. Thermo-expansion match: Many film-substrate combinations will be more or less mismatched with regard to thermal expansion. This may result in loss of adhesion or film cracking during thermal cycling.

3. Surface quality: It is at the surface where the film-substrate interaction takes place, so naturally, all deviations from the perfect state could potentially influence the film growth negatively. The surface must be atomically flat, dense, and free of twins and other structural inhomogeneities. Numerous surface defects can be encountered, ranging from the atomic scale: point defects, dislocations and twin boundaries, to macroscopic scale polishing scratches, surface warp and cracks.

4. Substrate homogeneity: Not only surface quality, but also the quality of the bulk is likely to affect film growth. Phase purity is important, otherwise the surface quality is likely to suffer. Grain boundaries should not reach to the surface, and the substrate should have the theoretical density and thus no voiding. Any such bulk imperfections are likely to influence the surface, which will induce defects in the film.

5. Substrate thermodynamic stability: A phase transition of the substrate within the processing and utilisation temperature range can have dramatic effects on the surface quality of the substrate and cause tremendous stress buildup in the film, possibly leading to cracks.

6. Lattice mismatch: The first criterium generally considered in selecting a substrate for epitaxial growth is its lattice match with the film. Studies indicated that for epitaxial films to grow, a lattice mismatch of less than 15% is required[47]. The ability to obtain singularly orientated films is improved by minimising the lattice mismatch as much as possible. The lattice mismatch μ, is calculated as

$$\mu = \frac{a_{film} - a_{substrate}}{1/2(a_{film} + a_{substrate})} \times 100\%, \tag{2.1}$$

where a_{film} and $a_{substrate}$ are the lattice parameters of the film and substrate, respectively.

7. Coincidence sites: In general, lattice match is not the only important factor to ensure good epitaxy; there must be a number of coincidence sites between the two

lattices. These are atomic positions (preferably occupied by atoms with similar sizes and valences) that coincide on either side of the surface[48]. Frequently, this is the case where the film and substrate have similar crystal structures. R. Guo *et al*[49] have shown that the primary consideration for substrate selection is similarity in interatomic structure, including the ionic distributions and distances.

2.1.1 $Si < 100 >$ substrate preparation

The silicon substrates were obtained by scribing 9 mm x 9 mm squares onto single crystal silicon wafers followed by cleaving. The rectangular substrates were cleaned using a standard procedure of ultrasonic agitation in methanol, acetone and trichloroethylene. After reversal of this treatment the samples were washed in deionized water (resistivity better than 12 $M\Omega$-cm) and etched in a 20% solution of HF acid to remove the surface oxide layer. The sample was placed on the centre of the substrate heater by means of silver paint.

2.1.2 Vacuum preparation

To achieve the high vacuum necessary for the pulsed laser deposition process, different pumps are used:

1. A rotary roughing pump *Alcatel* 215 which reduced the pressure to about 10^{-1} mbar;
2. Two *Pfeiffer* TPH240 turbo molecular pumps (TPMs) which can reduce the pressure up to 10^{-6} mbar

Usually pressures in the range of 10^{-5} mbar can be achieved after one hour of pumping; to reach the range of 10^{-6} mbar, one has to wait at least one day for the removal of mostly water vapour in the vacuum chamber. During the use of the TMPs, water cooling must be provided. Ultra high purity oxygen is introduced to the vacuum via a needle valve. Due to the pumping of oxygen during the deposition, a synthetic oil should be used

in the rotary pump instead of flammable mineral oil, known to cause explosions when pumping pure oxygen. The chamber is vented with nitrogen when opened to minimize the introduction of atmospheric moisture into the chamber. **Figure 2.1** gives the PLD vacuum chamber system layout.

2.1.3 Pulsed laser deposition (PLD)

Set up

Conceptually and experimentally, pulsed laser deposition is an extremely simple technique, probably the simplest among all thin film growth techniques. It consists of a target holder and a substrate holder housed in a vacuum chamber. A high-power laser is used as an external energy source to vaporize materials and to deposit thin films onto the substrate. The schematic lay-out and photograph of the pulsed laser deposition system are shown in **Figure 2.2**.

A set of optical components are used to focus and raster the laser beam over the target surface. The optical elements that couple the energy from the laser to the target are lenses and apertures; mirrors, and laser windows. The primary function of the lens is to collect radiation from a point source (laser) and focus it to a corresponding point on the target to achieve the required energy density for ablation. Dielectric multilayer mirrors are also used in order to deflect the laser beam into the port window. The decoupling of the vacuum hardware and the evaporation power source makes this technique so flexible that it is easily adaptable to different operational modes without the constraints imposed by the use of internally powered evaporation sources. During the deposition of multicomponent oxides, oxygen gas is used as an ambient gas because it plays an important role in the oxidation of the ablated species and therefore preserves the film stoichiometry.

The laser ablation equipment is made up of pumps and the vacuum chamber which houses the target carousel, the substrate holder with heater and the window for the

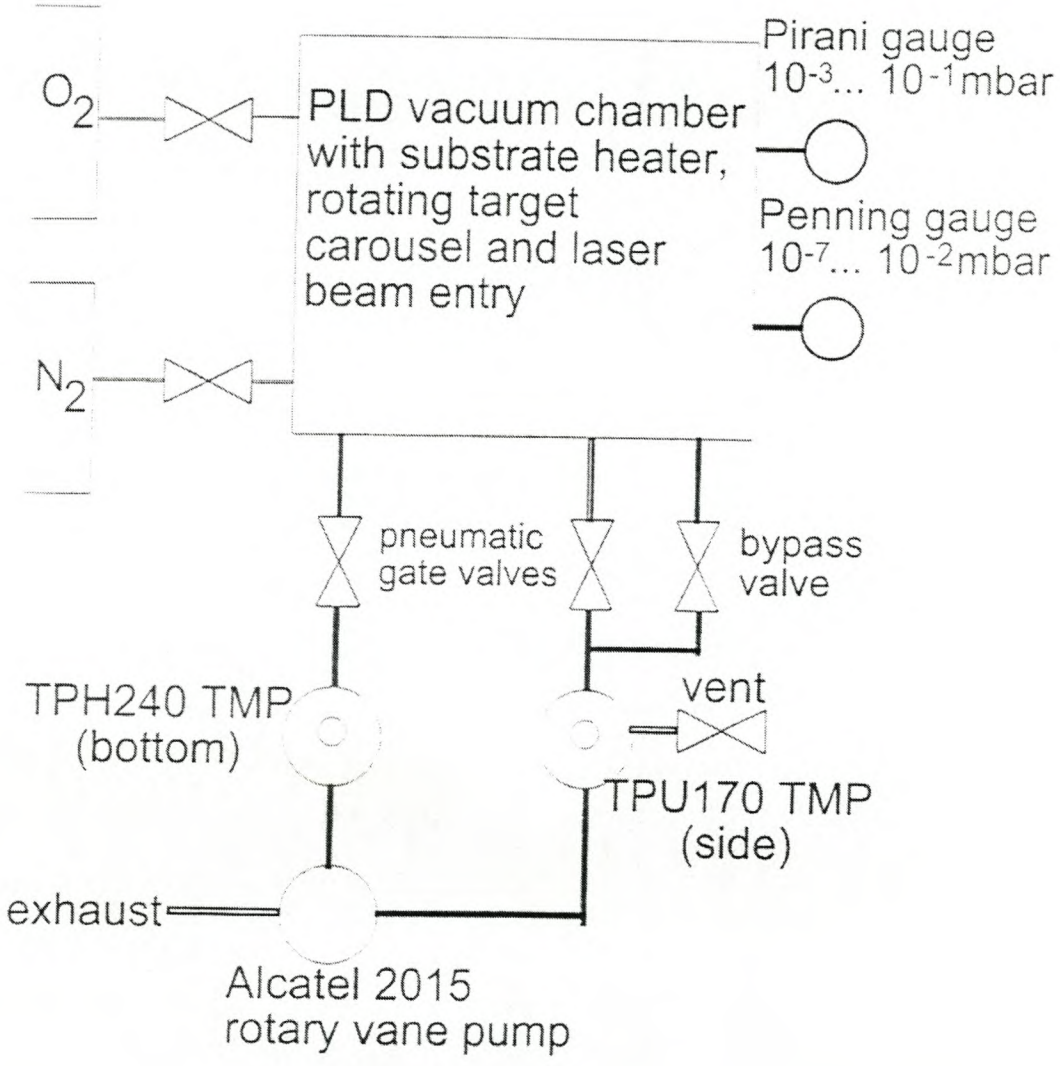

Figure 2.1: *Schematic diagram of vacuum vessel with pumps and gauges. The valves controlling the oxygen and nitrogen flow in the PLD vacuum chamber are needle valves.*

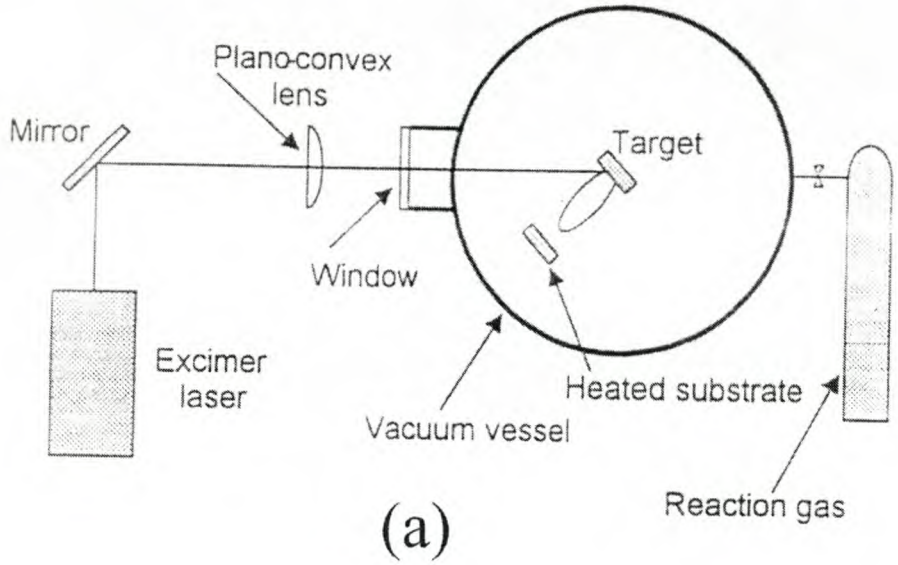

(a)

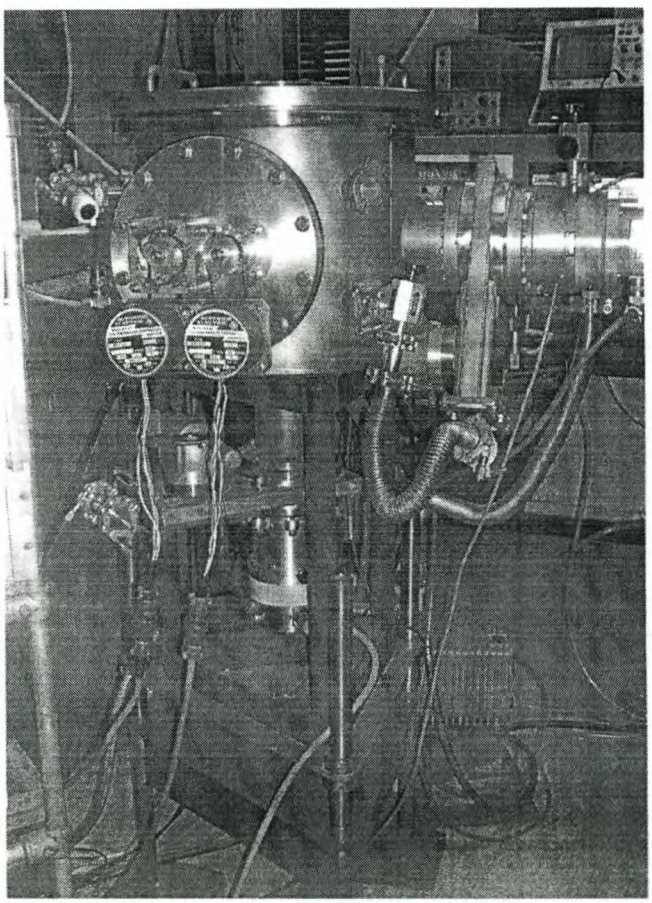

(b)

Figure 2.2: *(a) Planar view of the deposition principle and optical path of the PLD system. Notice that the incoming laser path makes a* 45^0 *angle with the normal of the target surface. (b) Full view of a pulsed laser deposition system housed at the Laser Institute, Physics Department, University of Stellenbosch with the excimer laser in the background (object on the right).*

incoming focused laser beam. The laser system made use of an excimer laser with wavelength (λ = 308 nm), pulse duration (τ_p=25 ns), pulse energy ranging from 100 to 150 mJ, and a repetition rate of 5 - 10 Hz. The beam leaving the excimer laser is directed onto a dielectric mirror, passed through a lens (f=300 mm) and the chamber window (both made of quartz) and impinges on the target close to its focal point.

The external equipment consists of a thermocouple, temperature controller for keeping the substrate at stable temperature and a substrate heater power supply enabling substrate temperatures of up to 850^o C. It also consists of a stepper control for the rotation of the target holder and pressure display connected to Pirani and Penning gauge.

Deposition parameters

Successful PLD is determined by the ability to reproduce the correct stoichiometry of the target onto the substrate. There are a number of deposition parameters which one can vary to achieve the desired result. These parameters are:

1. Laser energy density (Φ)
2. Laser wavelength (λ)
3. Substrate temperature (T)
4. Substrate-target distance (D)
5. Oxygen partial pressure (PO_2)

The optimum ranges for these parameters are summarized in the **Table 2.1** below.

Table 2.1: *Optimum range of conditions for laser ablation of manganites.*

Laser energy density	$2.5 - 3.5 J/cm^2$
Laser wavelength	200 - 400 nm
Substrate temperature	$680 - 780^0 C$
Substrate-target distance	25 - 40 mm
Oxygen pressure	0.1 - 1 mbar

When searching for the optimal deposition conditions, the deposition parameters appear to be strongly correlated. Analytical results using energy dispersive x-ray spectroscopy showed that films placed within the plume or near the tip of the visible plasma plume had the correct stoichiometry. At the tip of the plume, the ejectants consist mainly of low velocity ($< 10^5 cm/s$) neutral oxide molecules and neutral atoms. The length of the plume increases nonlinearly with energy density, thus a nonlinear D versus Φ exists for the optimal target-substrate distance. The empirical relationship obtained is:

$$(\Phi - \Phi_{th}) = D^2.0.14 J cm^{-4}, \tag{2.2}$$

where Φ_{th} is the laser ablation threshold, $\Phi_{th} \sim 1.0 - 2.0 J cm^{-2}$ for manganite materials. Similarly, an empirical relationship for PO_2 and D is

$$PO_2 D^2 = f(\Phi). \tag{2.3}$$

Thus one should decrease the target-substrate distance when the pressure is increased. By comparing the two relationships above, we get

$$PO_2D^2 = k(\Phi_{th}), \tag{2.4}$$

where k is a constant depending on parameters other than PO_2, D, and Φ. Increasing PO_2 would necessitate an increase in Φ to achieve optimal results by keeping the plume at the same length. The oxygen pressure plays a key role during the deposition process for high temperature superconductors as well as for magnetoresisitive materials. For these multicomponent materials, the oxygen content determines the stoichiometry of the thin film. Its deficiency leads to the suppression of the two phenomena, i.e., superconductivity and colossal magnetoresistance.

2.2 Sample Characterization

2.2.1 Rutherford backscattering spectrometry (RBS)

Rutherford Backscattering Spectroscopy (RBS) is perhaps the easiest analytical technique to understand and to apply in the study of thin films. Apart from the accelerator which provides a collimated beam of MeV particles (usually 4 He^{+2} ions), the instrumentation is simple. The sample is bombarded by a homogeneous non-interacting mono-energetic particle beam of 2-4 MeV. Some of the particles are transmitted or absorbed by the sample while others are backscattered. A solid state detector detects the backscattered particles. **Figure 2.3** shows the beam path and the detector position for scattered particles. The energies of the backscattered particles depend on the identity of the atoms from which the alpha particles scatter, the angle of scattering, and the depth into the sample to which the particles travel before scattering. Therefore, the analytical capabilities of Rutherford Backscattering Spectrometry depends on three concepts:

1. Kinematic factor K (mass analysis)

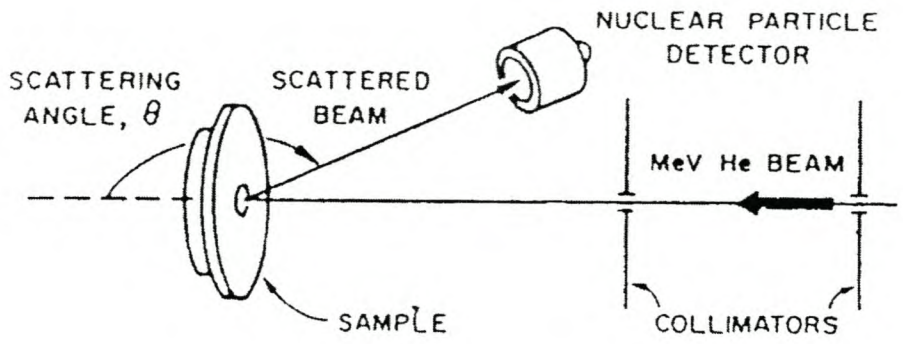

Figure 2.3: *Schematic of the experimental set up for RBS. A collimated beam of He ions is incident on a planar sample. Particles scattered through an angle θ are detected by a solid state nuclear particle detector. All this apparatus must be under vacuum.*

2. Differential cross section $\frac{d\sigma}{d\omega}$ (quantitative analysis)

3. Energy loss $\frac{dE}{dx}$ (depth analysis)

Kinematic factor

Monoenergetic particles in the incident beam collide with target atoms and are scattered backwards into the detector. The collision is assumed to be elastic. In the collision, energy is transferred from the moving particle to the stationary target atom (see **Figure 2.4**). Applying the principles of conservation of momentum and energy in a laboratory frame, the energy transferred in an elastic collision between two particles can be obtained. Conservation of energy and conservation of momentum parallel and perpendicular to the direction of incidence are expressed by the following equations

$$\frac{1}{2}mv_0^2 = \frac{1}{2}mv_1^2 + \frac{1}{2}Mv_2^2, \tag{2.5}$$

$$mv_0 = mv_1 \cos\theta + Mv_2 \cos\phi, \tag{2.6}$$

$$0 = mv_1 \sin\theta - Mv_2 \sin\phi. \tag{2.7}$$

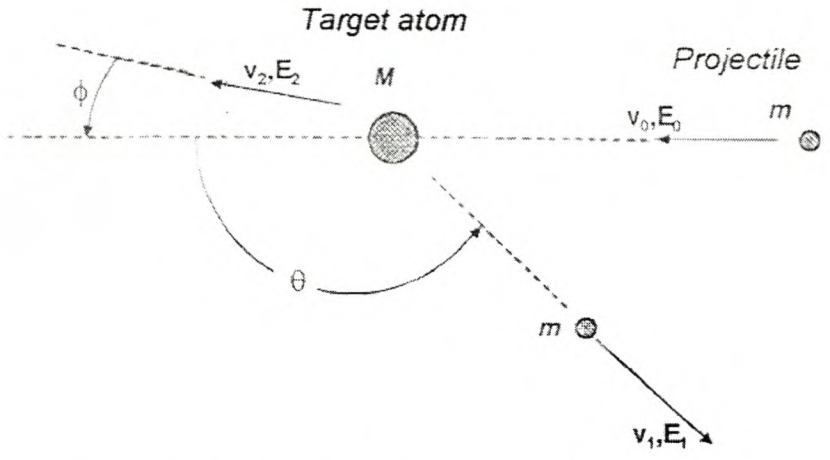

Figure 2.4: *Schematic representation of an elastic collision between a projectile of mass m, velocity v_0 and kinetic energy E_0 and a target mass M, which is initially at rest. After the collision, the projectile and the target mass have velocities and energies v_1, E_1, and v_2 and E_2, respectively. The angles θ and ϕ are positive as shown. All quantities refer to a laboratory frame of reference[50].*

Eliminating ϕ and v_2, we get a quadratic equation in the form of

$$\left(1+\frac{m}{M}\right)\frac{v_1^2}{v_0^2} - 2\frac{m}{M}\frac{v_1}{v_0}\cos\theta - \left(1-\frac{m}{M}\right) = 0. \tag{2.8}$$

Solving the equation, we find

$$\frac{v_1}{v_0} = \frac{m\cos\theta \pm \left(M^2 - m^2\sin^2\theta\right)^{\frac{1}{2}}}{m+M}. \tag{2.9}$$

For $m \leq M$, the plus sign holds. The kinematic factor K is defined as the ratio of the projectile energy after the elastic collision to that before the collision. From the equation 2.5, we can write:

$$K = \frac{E_1}{E_0} = \frac{v_1^2}{v_0^2} = \left[\frac{\left(M^2 - m^2\sin^2\theta\right)^{\frac{1}{2}} + m\cos\theta}{m+M}\right]^2. \tag{2.10}$$

We see, from the equation 2.10 that the kinematic factor K depends on the scattering angle θ in the laboratory system and the masses involved in the collision process, i.e $K = f(m, M, \theta)$. Therefore if m, θ, together with the ratio E_1/E_0 are known, the target mass M can be determined.

Differential cross section

A narrow beam of fast particles impinges on a thin film target that is wider than the beam. At an angle θ from the direction of incidence, the detector counts each particle scattered in the differential solid angle $d\Omega$. If Q is the total number of particles that have hit the target and dQ is the number of particles recorded by the detector, then the differential scattering cross section $\left(\frac{d\sigma}{d\Omega}\right)$ is defined as

$$\frac{d\sigma}{d\Omega} = \frac{1}{Nt}\left[\frac{1}{d\Omega}\frac{dQ}{Q}\right], \tag{2.11}$$

where N is the volume density of atoms in the target and t its thickness. Thus Nt is the number of target atoms per unit area. The differential cross section $\left(\frac{d\sigma}{d\Omega}\right)$ is the probability per unit solid angle that an incident particle is scattered into the solid angle $d\Omega$ and therefore it connects the backscattering yield to the quantitative analysis. To calculate the differential cross section for an elastic collision, the principles of conservation of energy and momentum must be complemented by a specific model for the force that acts during the collision between the projectile and the target masses. In most cases, this force is very well described by the Coulomb repulsion of the two nuclei as long as the distance of closest approach is large compared with nuclear dimensions, but small compared with the Bohr radius $a_o = \frac{\hbar}{m_e e} = 0.53\mathring{A}$. When these assumptions are made and after some transformations, one gets the following formula for the differential cross section

$$\frac{d\sigma}{d\Omega} = \left(\frac{zZe^2}{4E_o}\right)^2 \frac{4}{\sin^4\theta} \frac{\left[\cos\theta + \left(1 - \frac{m^2}{M^2}\sin^2\theta\right)^{\frac{1}{2}}\right]^2}{\left[1 - \left(\frac{m}{M}\sin\theta\right)^2\right]^{\frac{1}{2}}}, \tag{2.12}$$

where ze is the charge of the projectile; Ze, the charge of the target and E_o the energy of the projectile before scattering. This expression shows the significant dependences of the Rutherford differential cross sections:

1. $\left(\frac{d\sigma}{d\Omega}\right)$ is proportional to z^2. The backscattering yield obtained from a given target atom with a He beam ($z = 2$) is four times as large as with a proton beam ($z = 1$) but only a ninth of that produced by a carbon beam ($z = 6$).

2. $\left(\frac{d\sigma}{d\Omega}\right)$ is proportional to Z^2. For a given projectile, heavy atoms are more much efficient scatterers than light atoms. Therefore, backscattering spectrometry is more sensitive to heavy elements than to light ones.

3. $\left(\frac{d\sigma}{d\Omega}\right)$ is inversely proportional to the square of the projectile energy (E_0^2). The yield of scattered particles rises rapidly with decreasing bombarding energy.

4. $\left(\frac{d\sigma}{d\Omega}\right)$ is axially symmetrical with respect to the incident beam, i.e. $\left(\frac{d\sigma}{d\Omega}\right)$ is a function of θ only.

5. $\left(\frac{d\sigma}{d\Omega}\right)$ is approximatively inversely proportional to the fourth power of $(\sin\frac{\theta}{2})$ when $m \ll M$. This dependence gives rapidly increasing yields as the scattering angle θ is reduced.

Energy loss

When a projectile penetrates a target, it loses its energy to the electrons of the target atoms by ionisation and excitation as well as by nuclear collisions. When the projectile undergoes an elastic collision it can change its trajectory into an outward direction with respect to the target surface. During its outward path, it again loses energy to the target atoms until it emerges from the target. By measuring this energy loss, the depth to which the particle has penetrated can be determined. The energy loss per unit length is expressed as a stopping power, $\frac{dE}{dx}$. The stopping cross section is given as $\varepsilon = \frac{1}{N}\frac{dE}{dx}$, where N is the atomic density of the target. Both stopping power and stopping cross section

depend upon the composition of the target and is a relatively slowly varying function of projectile energy. In general, for small losses, $\frac{dE}{dx}$ does not change much and there exists a linear relation between energy loss (ΔE) and depth (t) that can be expressed as $\Delta E = [S]t$, where $[S]$ is called the backscattering energy loss factor. In the so-called surface approximation, where the target film is very thin, it can be assumed that $\frac{dE}{dx}$ of the projectile does not change and can be evaluated at the energy E_0 for its incoming path and $E_1 = KE_0$ for its outgoing path. Thus, the energy lost by a projectile (mass m) which was backscattered by an atom (mass M) at depth t, can be approximated as:

$$\Delta E = [S]t = \left[\frac{K}{\cos\theta_1}\frac{dE}{dx}\,|_{E_0} + \frac{1}{\cos\theta_2}\frac{dE}{dx}\,|_{KE_0}\right]t \tag{2.13}$$

in which θ_1 and θ_2 are the angles between the surface normal and the incoming (1) and the outgoing (2) particle direction respectively.

In a compound target, the energy loss is calculated or measured from the stopping power of the projectile in the compound, while the scattering occurs between the projectile and a given atom of the compound molecule. The energy loss for a particle backscattered from element A at depth t in compound A_mB_n is given in the same way as equation 2.13 as

$$\Delta E_A = [S]_A^{A_mB_n}t = \left[\frac{K_A}{\cos\theta_1}\frac{dE}{dx}\,|_{E_0} + \frac{1}{\cos\theta_2}\frac{dE}{dx}\,|_{K_AE_0}\right]t, \tag{2.14}$$

where K_A is the backscattering kinematic factor of element A. The application of additivity of stopping cross sections for compound targets is based on Bragg's rule which states that $\varepsilon^{A_mB_n} = m\varepsilon^A + n\varepsilon^B$, where ε^A and ε^B are the stopping cross sections of the individual atoms A and B. The total energy loss in the compound A_mB_n can thus be given as

$$\Delta E = [S]^{A_mB_n}t = \frac{m}{m+n}[S]_A^{A_mB_n}t + \frac{n}{m+n}[S]_B^{A_mB_n}t. \tag{2.15}$$

The energy spectra of backscattered particles give quantitative information on the atomic density depth profiles of the atom in the sample. The height of the spectrum H gives the number of backscattered particles with energy in a certain energy interval δE between E

and E+δE, and is given by

$$H = n_0 \Omega \left(\frac{d\sigma}{d\Omega}\right)_A N \frac{\delta E}{[S]\cos\theta_1}, \tag{2.16}$$

where n_0 is the number of incident particles, Ω the solid angle of the detecting system and N the atomic density, while $\frac{d\sigma}{d\Omega}$ and [S] are given by equations 2.12 and 2.13 respectively. The height of the spectrum peak H_A for element A in compound A_mB_n can be given in the same way as equation 2.13

$$H_A = n_0 \Omega \left(\frac{d\sigma}{d\Omega}\right)_A N_A \frac{\delta E}{[S]_A^{A_mB_n}\cos\theta_1}, \tag{2.17}$$

where N_A refers to the density of atoms A in compound A_mB_n. A similar equation holds for H_B the height of the spectrum peak for element B. It is obvious that N_A and N_B are proportional to m and n, thus

$$\frac{H_A}{H_B} = \frac{\sigma_A}{\sigma_B}\frac{m}{n}\frac{[S]_B^{A_mB_n}}{[S]_A^{A_mB_n}}, \tag{2.18}$$

where σ_A is the average differential scattering cross section given by

$$\sigma_A = \frac{1}{\Omega}\int \left(\frac{d\sigma}{d\Omega}\right)_A d\Omega. \tag{2.19}$$

Extensive use has been made of the Rutherford Universal Manipulation Program (RUMP) RBS simulation package[51] and a detailed description of the package is given in **Appendix C**. Although RBS has many favourable features for determining depth profiles quantitatively, the technique does, however, suffer from two serious limitations.

1. It is difficult to determine the identity of heavy atomic species, since the mass resolution decreases with increasing mass.

2. Low levels of light mass impurities in heavier mass substrates are difficult to measure because of the unfavorable ratio of scattering cross sections.

2.2.2 Atomic force microscopy (AFM)

Introduction

Atomic force microscopy (AFM) is a powerful tool for the examination of surfaces. In general, AFM enables one to detect surface morphology, nanoscale structures, and under ideal conditions, molecular and atomic-scale lattices[52]. In contact mode AFM, the spatial variation of the tip-sample repulsive force or that of the tip height is converted into an image as the tip is scanned relative to the sample surface in a raster-line fashion, generating a three-dimensional topographical image[53]. Surface morphology can be accurately determined, and since the repulsive force is universal, AFM is applicable to conducting and insulating materials. In AFM it is commonly the repulsive force between the tip (located at the end of a cantilever) and sample that is measured, on the basis of the cantilever deflection. In contact-mode AFM measurements, all electrons of the surface atoms are involved in the repulsive interactions with the tip, so that the AFM image is described by the total electron density plot $\rho(r)$ of the surface. The forces range in strength from $10^{-9} - 10^{-7}$N.

System set-up

The AFM system consists of the optical block (see **Figure 2.5**) and the base. The stepper motor, the alignment screws, and the sample scanner are installed in the base, and the sample is mounted on the top of the scanner. The optical block contains a viewing window at the top, a diode laser, mirrors, and a four-quadrant positional photodetector. The cantilever holder is fixed on top of the alignment screws, with the tip positioned over the sample. The optical camera attached to the viewing-window allows one to observe the cantilever for alignment of the laser beam and for positioning the tip over the sample area of interest. A laser beam is directed towards the cantilever. The atomic force microscope is mounted on an air cushioned granite table which stabilises the microscope to a high level of accuracy. The granite table was supported by rubber pads with a low ($\sim 1Hz$) natural frequency. The AFM is also shielded against acoustic noise by covering

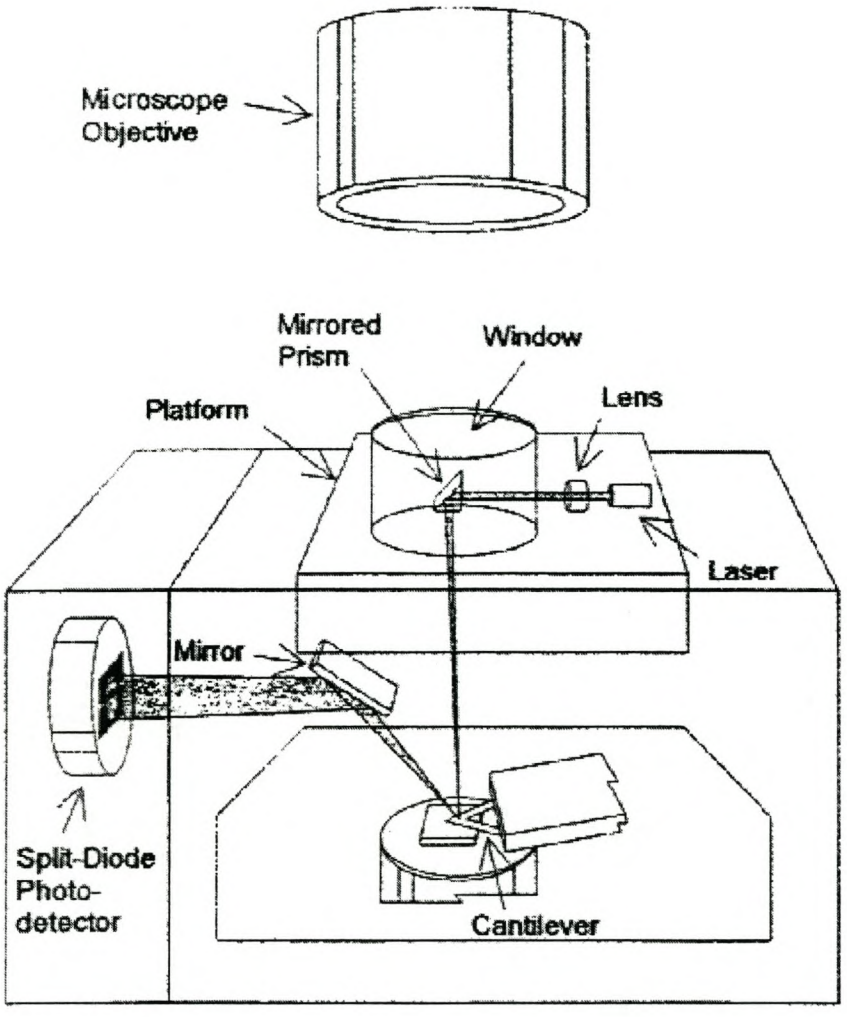

Figure 2.5: *Optical block system of the Atomic Force Microscope. The function of each component is described in the text.*

the system with a metal cylinder. The *Topometrix TMX2000 Explorer* atomic force microscope at the Institute of Polymer Science at the University of Stellenbosch was used in the contact mode. A Si_3N_4 V-shaped cantilever with an integrated Si_3N_4(tip radius 30 nm) tip was used. Hooke's law, $F = -kx$, relates the cantilever's displacement to the force applied to the probe. Forces less than 10^{-10} N are detectable in ideal conditions, but 10^{-8} N was typically achieved in this study. The force constant of the stiff cantilever used was $k = 0.27N/m$. It was found that stiff cantilevers produce better results on hard surfaces than less stiff ones. The surface analysis was conducted using the image processing software *SPMLab version 3.06*[54]. The probe is microfabricated from Si_3N_4 or silicon and the tip is sharpened to a tip radius of $10 - 50$ nm. For the investigation of flat surfaces, pyramid shaped probes with low aspect ratios are usually employed.

For the analysis of colossal magnetoresistive thin films, which present a hard, relatively flat, electrostatically neutral surface, a silicon nitride pyramid probe was used. We assume, with $La_2CaMn_3O_9$ films, that the hardness of the sample is everywhere the same, thus there is no need to correct the image for indentation effects. Contact mode AFM was used, where the probe tip scans the surface, coming into direct contact with the sample. As the probe scans, various topographic features deflect the cantilever. Tip-sample adhesion, which leads to hysteresis in the force-distance curve, is a direct consequence of the surface forces. In ambient-condition experiments, this hysteresis is enhanced by capillary forces associated with the contamination layer. Since we operated the AFM at a constant force, this did not influence our measurements. When the tip comes close to the sample, the cantilever is deflected from its equilibrium position in response to the force experienced by the tip. It bends towards the sample when the force is attractive. This is due to Van der Waals (VDW) forces, eg. a Lennard-Jones-type potential. When the sample is moved further towards the tip, the attractive force exceeds the spring constant of the cantilever, and the tip jumps to the surface. The typical forces between the tip and the sample surface in the contact-mode is $10^{-9} - 10^{-8}$N. When operating the AFM in open air, the capillary action of the ever present thin film of moisture on the sample

surface must also be taken into account.

Scanner

In the AFM system, the driving motion is performed by piezoceramic actuators, which change their dimensions under applied voltage. A hollow piezoelectric tube was used, which can move the sample in all three mutually perpendicular directions. The application of different voltages to each pair of electrodes on the tube's outer surface induces tube bending, which provides lateral motion to the sample attached to the tube. Application of different voltages to the outer and inner electrodes shrinks or extends the tube, which moves the sample vertically. Nonlinearity of the response of the tube is corrected by computer software.

Tip-sample approach

The tip was brought close to the sample by stepper motor control, while the final adjustment of the tip-sample separation, to the value at which the probe interaction reaches the set-point level determined by the user, is performed by the piezoelectric scanner. The tip-sample alignment is controlled by a feedback mechanism. The difference Δ between the actual and set-point values of the probing interaction is used for feedback control. The electronic feedback system generates the response to the scanner, to adjust the vertical position to eliminate the difference Δ. Two scanning methods are usually applied. In the *constant height* method, in which the feedback mechanism is turned off, one detects the charges in the probing interaction at a constant tip-sample separation. In the *constant-interaction* method, in which the feedback mechanism is activated, one detects the variations of the local z-height of the tip with respect to the sample surface at a fixed interaction strength. This is the method employed in this study. In our system, each scan line consists of 512 points, and scanning proceeds with line scanning frequencies in the 1 - 60 Hz range. A plane-fit adjustment was performed when the sample surface was not exactly perpendicular to the scanner z-axis.

Contact mode

In contact mode, the repulsive force is measured by recording the cantilever deflection, by way of the movement of the reflected laser beam at the photodetector. We used the constant interaction method, in which the cantilever is kept under a constant force through a feedback loop. The constant force implied a constant displacement for the cantilever. The vertical displacement of the cantilever is proportional to the differential signal from the vertical segments of the photodetector $\Delta V = V_{up} - V_{down}$. The reduced differential signal $\delta V/(V_{up} + V_{down})$ is used in the feedback signal to keep the cantilever force at the required set-point. The operating force is in the range $10^{-9} - 10^{-7}$ N. The topographic data are then obtained from the control variables, for example the voltages applied to the piezocrystals. Resolution in the z-direction is limited by the level of vibrations between the probe and the surface. The amount of displacement can then be accurately calculated from the difference in light intensity on the sectors.

Surface roughness

AFM is able to provide quantitative information, such as surface roughness and area measurements, in addition to high-resolution micrographs. There are many engineering parameters that can be used to characterize surfaces, such as roughness, waviness, skewness, and roundness. Roughness itself also has many variations, such as R_{max}, the maximum peak-to-valley distance, R_{tm}, the depth of roughness, and R_q, the root-mean-square roughness. For most studies, R_a, which is the arithmetic roughness average of the absolute values of the measured profile deviations is used. It is given by the following expression:

$$R_a = \frac{1}{N}\sum_{i=1}^{n} |Z_i - \overline{Z}| \tag{2.20}$$

where, R_a is the arithmetic roughness average, n the number of height positions along the line profile, Z_i the height at position i, and $\overline{Z}$the average height.

2.2.3 Scanning electron microscopy (SEM)

In the SEM an electron beam is generated with an electron gun, accelerated through a high voltage and focused into a fine probe by electro-magnetic lenses. The electro-optical column through which the beam passes is held under a high vacuum to allow a free path for the electrons and to prevent high voltage discharge. Accelerating voltages vary between 5 and 40 kV. A ray diagram of a two lens SEM is shown in **Figure 2.6**. The condenser lens causes the electrons to converge and pass through a focal point which is above a condenser aperture. The condenser lens, in conjunction with the chosen accelerator voltage is primarily responsible for the intensity of the electron beam when it strikes the specimen. The beam again diverges below the condenser lens aperture. A final lens is used to bring the beam into focus at the specimen by demagnifying (converging) it to a focal point at the specimen surface.The electron beam is scanned across the sample by scan coils (see **Figure 2.6**). From this the name scanning electron microscope. As the beam is scanned across the specimen a detector counts the number of low secondary electrons given off from the surface of the sample. At the same time the spot of a cathode ray tube (CRT) is scanned across the screen in a similar way as in a television. The signal measured by the detector is amplified and coupled to the CRT. The brightness of the point on the screen is therefore dependent on the amount of secondary electrons given off at the corresponding point on the surface of the sample. A one-to-one presentation is therefore produced between the area scanned and the screen of the CRT. Magnification of the image is the relationship between the length of the scan line on the specimen and on the CRT screen. A prerequisite for effective viewing is that the surface of the sample must be electrically conductive. During operation electrons are deposited onto the sample. These electrons must be conducted away to earth potential.

2.2.4 X-ray diffraction (XRD)

X-ray diffraction (XRD) is used to determine the crystalline quality of a thin film by finding the crystalline phases or orientations of the various crystal planes[55]. XRD can

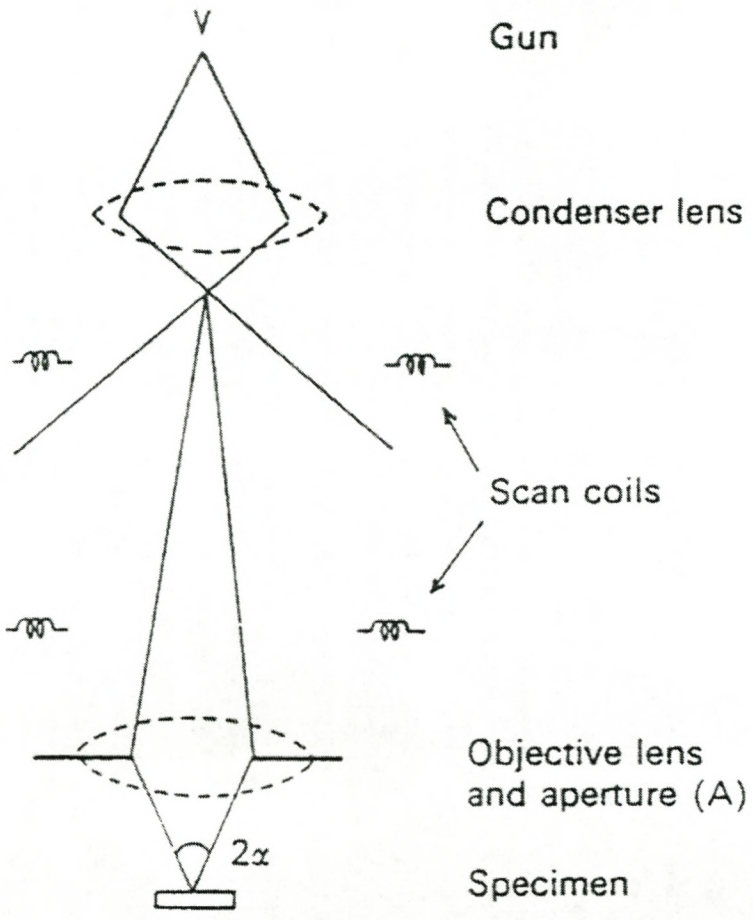

Figure 2.6: *Ray diagram of a two lens SEM showing the electron beam path to the specimen.*

determine the orientation of crystal grains in a thin film, thereby showing whether the film has grown epitaxially or not. The film could also be shown to be polycrystalline, single crystal or amorphous.

The Bragg-Brentano geometry, also known as the $\theta - 2\theta$ -geometry, usually employed for powder samples, is also commonly used to determine which, if any, of a film's diffraction planes lie parallel to the substrate surface. **Figure 2.7 (a) and (b)** shows the geometry for Bragg-Brentano measurement. The purpose of this set-up is to measure the intensity of the x-rays scattered through an angle of 2θ while the angle θ is scanned. When working with thin films, it is important to use glancing angle geometries so as to limit the penetration of the X-rays and therefore enhance the diffraction pattern of the film with respect to the substrate. X-rays provide superior angular resolution and contain more structural data than is available from electron diffraction. Their main drawback is much less intense diffracted intensities necessitating longer exposure times. The basis of X-ray diffraction is the Bragg equation which describes the condition for constructive interference of X-rays scattered from atomic planes of a crystal. The condition for constructive interference is,

$$2d \sin\theta = n\lambda, \tag{2.21}$$

where λ is the wavelength of the incident radiation and n is the order of the reflection. The Bragg's law requires that θ and λ be matched. If the thin film is polycrystalline, the distribution of orientations of the crystalline phases will be nearly continuous, and diffraction will occur from crystallites which happen to be oriented at the angle satisfying the Bragg condition.

2.2.5 Resistivity measurements

The transition temperature of colossal magnetoresistance materials is determined by measuring the electrical resistivity as a function of temperature. The experimental set-up is shown in **Figure 2.8**. The set-up consists of a supporting tube with the sample holder

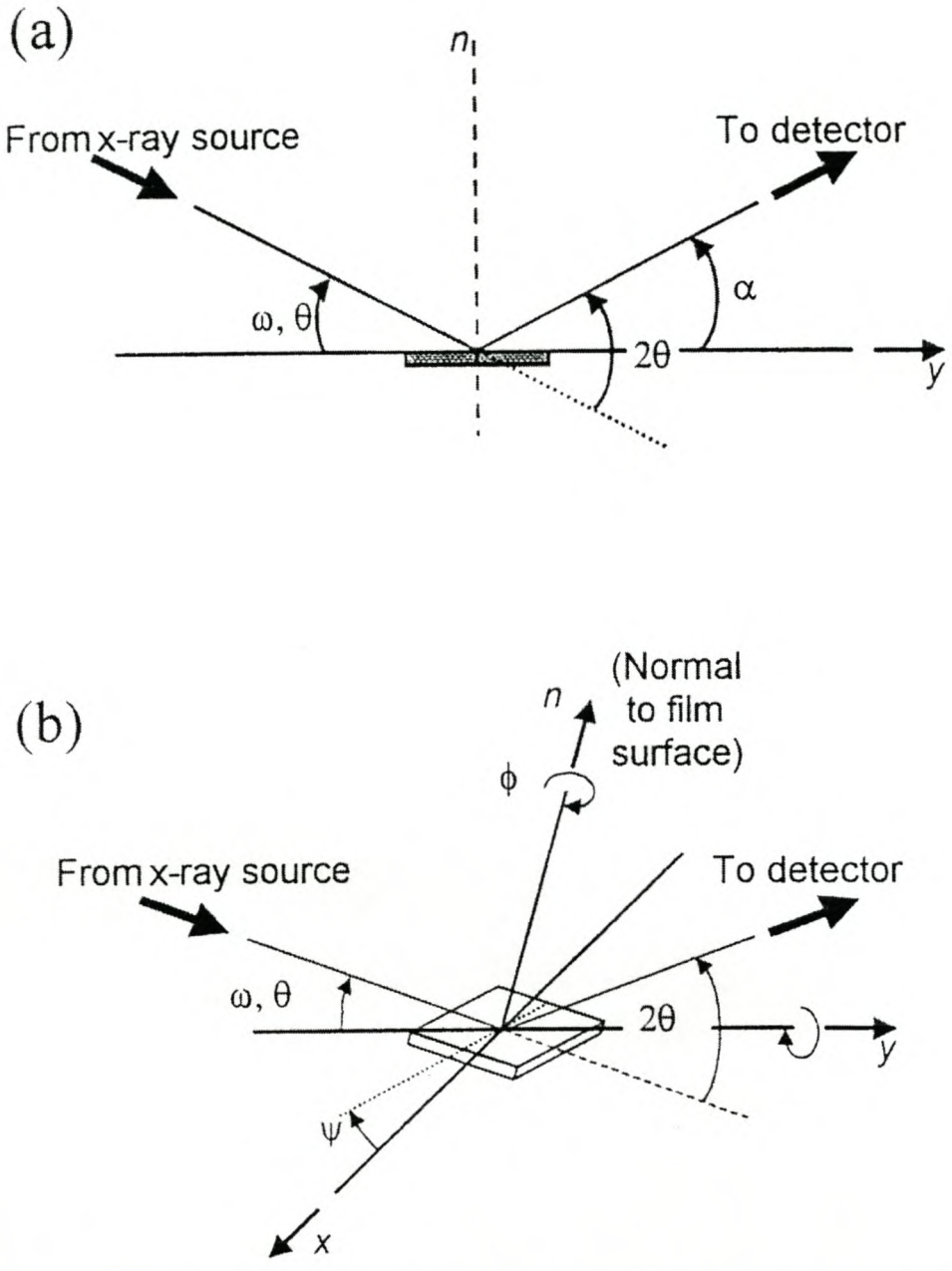

Figure 2.7: *Diagram showing the principal angles for XRD. (a) The geometry for Bragg-Brentano (θ-2θ) measurement. The purpose of this set-up is to detect or measure the intensity of the x-rays scattered through an angle of 2θ while the angle θ is scanned. (b) Three-dimensional diagram of general XRD set-up. The horizontal plane is indicated by the x-y plane. The sample can be tilted out of the horizontal plane, indicated by the angle ψ (around the y-axis). The vector* $\mathbf{n}$ *denotes the normal to the sample surface. The sample can be rotated around the (movable) normal axis,* $\mathbf{n}$*, indicated by the angle ϕ. The origin, located on the film surface, was a stationary point in this geometry.*

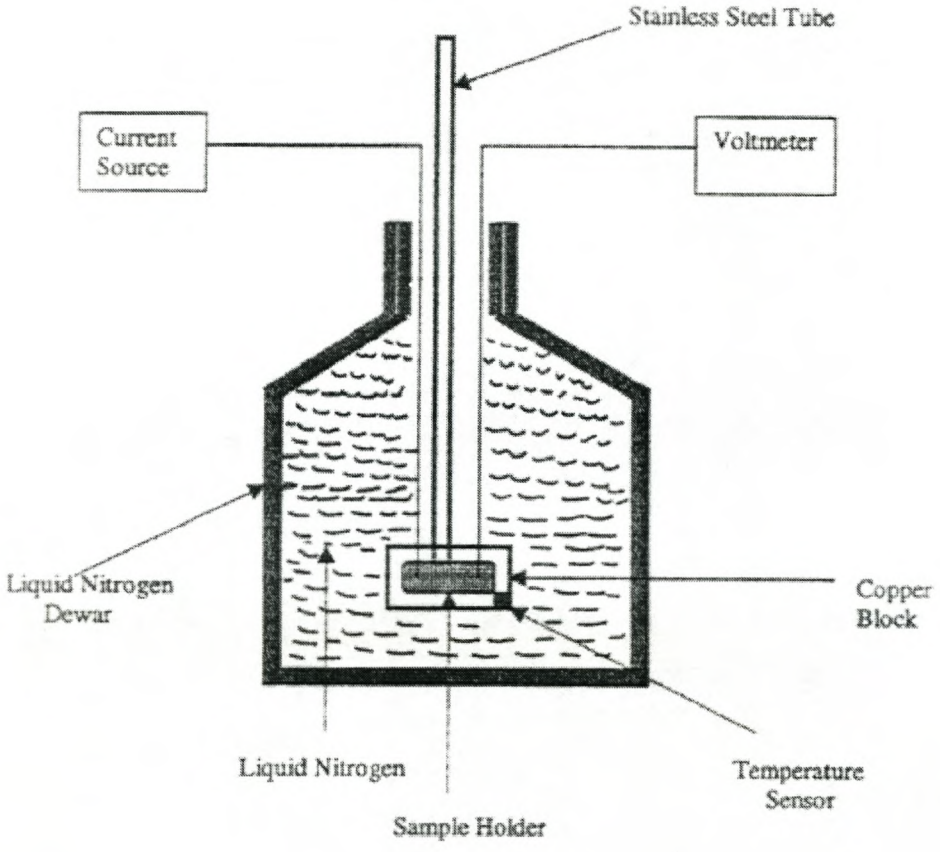

Figure 2.8: *Experimental setup for the resistivity measurements.*

on the tip. Four gold contact pads are deposited on the sample by cathode sputtering. The current leads are glued to these gold pads by means of a silver conductive paint. Two of the leads are connected to a current source, and the other two to a voltmeter. This is called a four-point probe technique. A temperature sensor is placed inside the copper block very close to the sample holder and connected to the temperature controller. The copper block with the supporting tube is placed in the dewar filled with liquid nitrogen. A polystyrene plug is used to seal the neck of the Dewar when the copper block is lowered down. The data acquisition is fully automated by connecting the output of the temperature controller and the voltmeter to a computer. The copper block is lowered slowly into the Dewar and as the temperature of the sample decreases, the voltage is measured as a function of temperature.

Chapter 3

Modeling and Simulation of the *LCMFO* System

3.1 Introduction

One of the main characterization techniques in this investigation is Rutherford Backscattering Spectrometry (RBS). Details of this technique are given in **section 2.2.1**. The main advantages of this technique are the following:

1. Concentration of elements is determined as a function of depth.
2. The technique provides stoichiometric and thickness information of the film.
3. Characterization is non-destructive.
4. RBS is fast and it takes typically 2-10 minutes to obtain a suitable spectrum.
5. RBS spectra of the system to be studied can be obtained by simulation (see Rump simulation package -**Appendix C**) before experimental research is carried out.

Simulation of RBS spectra (point 5) on a computer is a very powerful method of determining the effects of various parameters (thickness, stoichiometry, etc.) before actually starting to carry out experiments. The system to be studied can therefore be modeled systematically beforehand.

3.2 Effect of Different Substrates

Depending on the substrate composition, RBS spectra can differ from one substrate to another. In **Figure 3.1**, simulated spectra for a $La_2CaMn_{2.94}Fe_{0.06}O_9$ film 2000A^o thick on various substrates , namely Si< 100 >, MgO< 100 >, $SrTiO_3$< 100 > and $LaAlO_3$< 100 > are shown. From the simulated spectrum on Si (**Figure 3.1 (a)**), the Ca, Mn and La signals can clearly be observed separately. This is due to their respective atomic masses (M_{Ca}=41.0, M_{Mn}=54.9, M_{La}=138.9) which are larger than the Si atomic mass (M_{Si}=28.1). There is an overlap only between the Si signal and the oxygen signal(M_O=16.0). This situation also applies for the simulated spectrum of MgO< 100 > (**Figure 3.1 (b)**). However in **Figure 3.1 (c)** and **Figure 3.1 (d)**, the situation is quite different. From the simulated spectrum on $SrTiO_3$ (**Figure 3.1(c)**), only the La signal can clearly be seen. The rest, i.e., Ca, Mn and O signals overlap with the signals from the substrate. In **Figure 3.1(d)**, the overlap is total because of the presence of the La in the substrate. As it can be seen, the La signal causes a high background continuum which swamps the signals from the other elements. The film thickness can however be determined by measuring the width of the step in the La signal.

3.3 Effect of Thickness

From RBS spectra information of the film thickness can be obtained. In **Figure 3.2**, simulated spectra of a $La_2CaMn_{2.94}Fe_{0.06}O_9$ film of various thicknesses (1000 $\AA$, 2000 $\AA$, 3000 $\AA$, 4000 $\AA$) deposited on Si< 100 > substrate are shown. It can clearly be seen that as the thickness of the film increases the width of the signals for O, Ca, Mn and La broadens. It can also clearly be observed that as the thickness increases, signals from some elements start to overlap. This is the case in **Figure 3.2(c)** where a small overlap between the Ca and Mn signals can be seen and in **Figure 3.2(d)** where a pronounced overlap between these two signals can be observed. It can therefore be seen that RBS is ideally suited for determining thicknesses of manganite films up to about 3000$\AA$ by

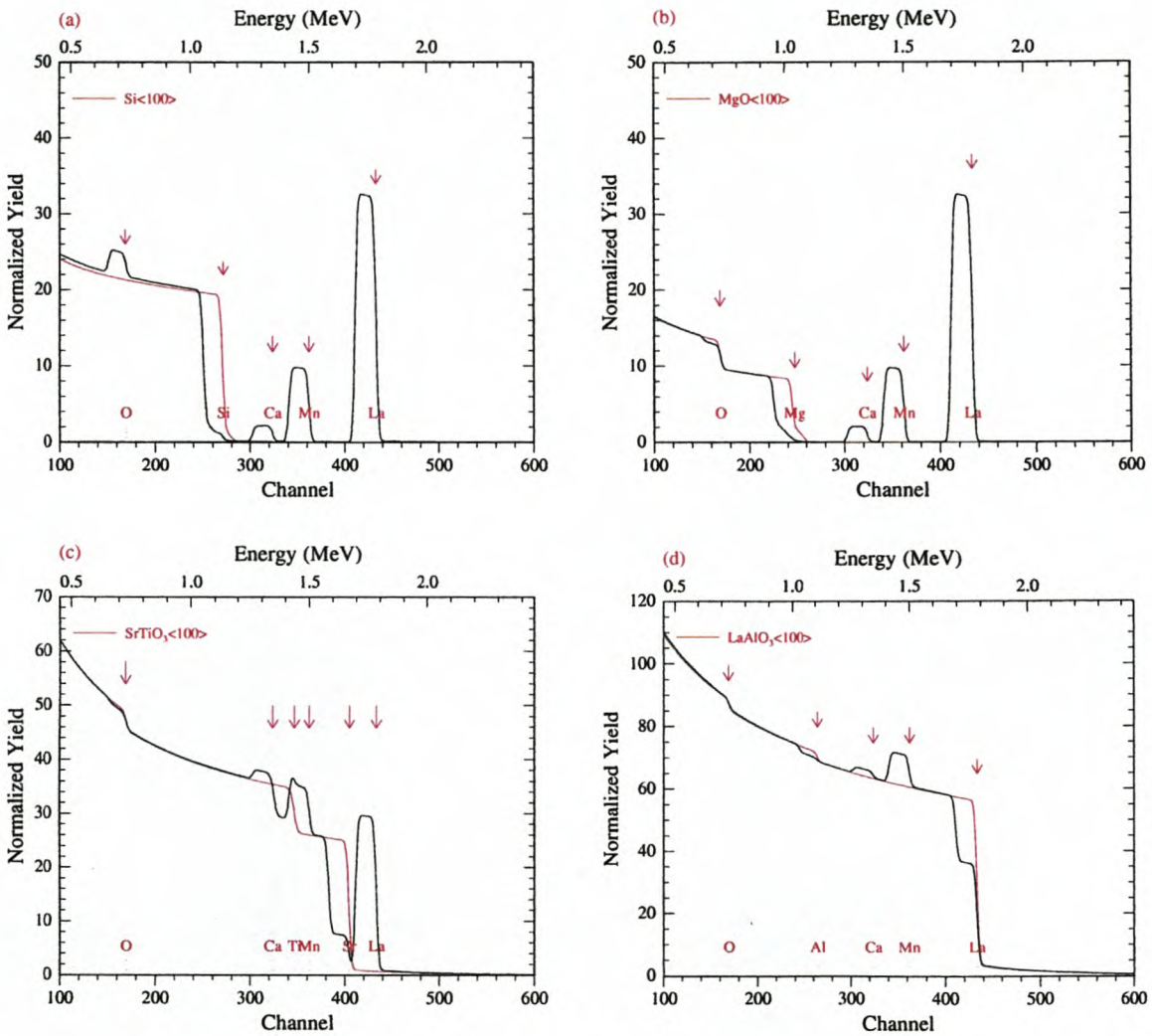

Figure 3.1: *Simulated RBS spectra for a* $La_2CaMn_{2.94}Fe_{0.06}O_9$ *film 2000 Å thick on various substrates. (a)* $Si<100>$ *(b)* $MgO<100>$ *(c)* $SrTiO_3<100>$ *and (d)* $LaAlO_3<100>$. *The red spectra were obtained by simulation of the substrate only, therefore with no manganite film on it. The vertical arrows show the surface energy position for the different elements in a sample. It is interesting to note that the surface energy of the elements in the substrate is pushed back to lower energies due to the thin film on top of the substrate.*

measuring the width of the Ca, Mn and La signals. For much thicker films iterative simulation and fitting can be used.

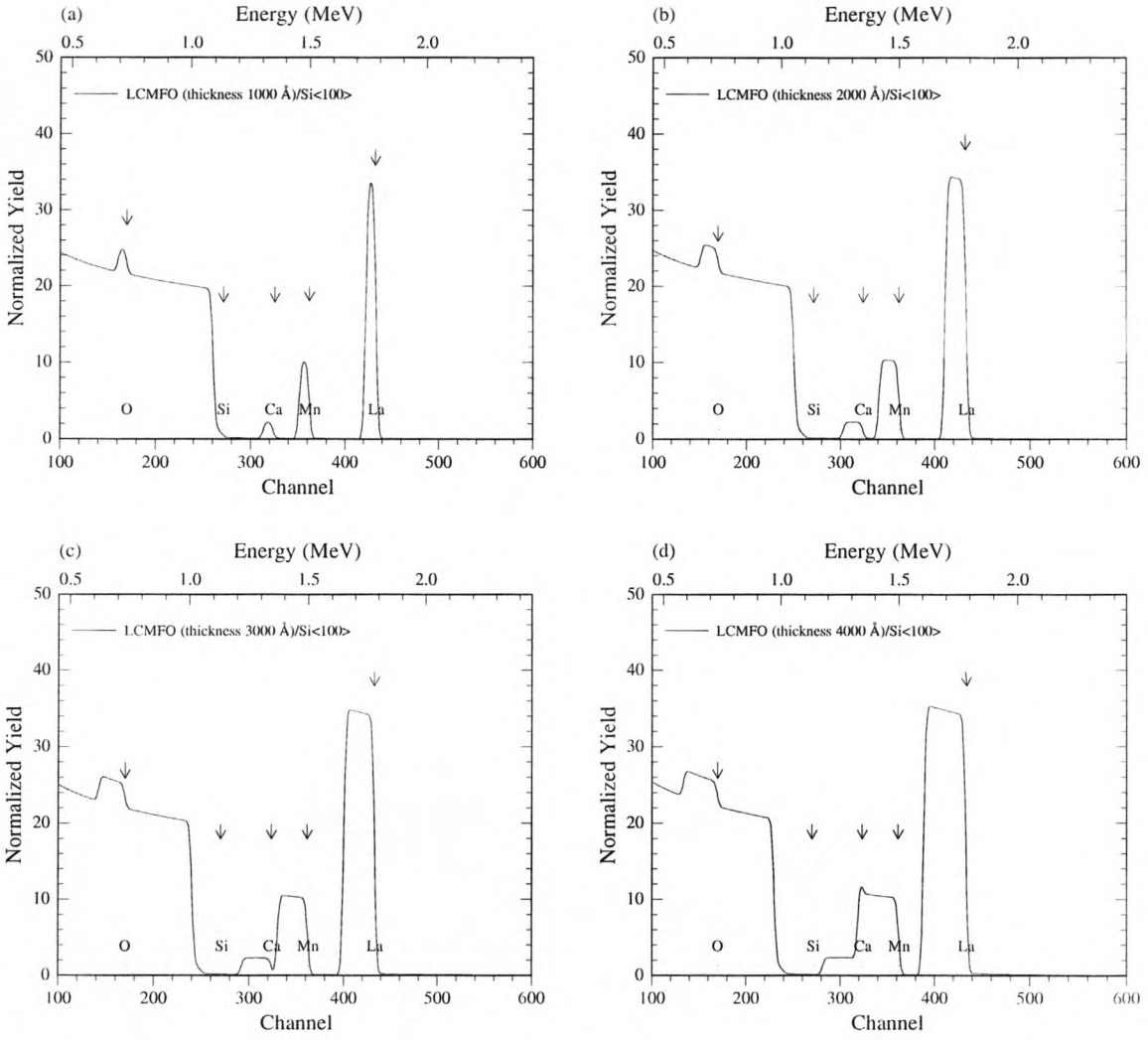

Figure 3.2: *Simulated RBS spectra of a* $La_2CaMn_{2.94}Fe_{0.06}$ *film of various thicknesses deposited on Si*$<100>$ *substrate. (a) 1000 Å (b) 2000 Å (c) 3000 Å (d) 4000 Å. The vertical arrows again give the surface energy positions of the various elements in the sample.*

3.4 Effect of Stoichiometry

When dealing with the fabrication of thin films by PLD, the stoichiometry between the target and the film must be the same to obtain a film of high quality. In **Figure 3.3**, simulated RBS spectra of two films (2000Å thick) with different La and Ca concentrations, namely $La_{2.0}Ca_{1.0}Mn_3O_9$ (blue) and $La_{2.5}Ca_{0.5}Mn_3O_9$ are shown. Though the two films have the same thickness, their stoichiometry is not the same. From the blue spectrum, it can be clearly seen that the La signal has dropped by 20% and the Ca signal by 50%,while the Mn and O signals conserve their stoichiometry. In **Figure 3.4**, simulated spectra of two films with different Mn and Fe concentrations, namely $La_{2.0}Ca_{1.0}Mn_3O_9$ (in red) and $La_{2.0}Ca_{1.0}Mn_{1.5}Fe_{1.5}$ (in blue) are shown. Because the masses of Mn ($M_{Mn} = 54.9$) and Fe ($M_{Fe} = 55.8$) are almost similar, it can clearly be seen that the replacement of Mn by Fe does not significantly affect the RBS spectra. Because RBS cannot distinguish between Mn and Fe, it is preferable to indicate the surface position either by Mn or Fe.

3.5 Film Thickness on $LaAlO_3$ Substrates

As mentioned before (see section 3.2), the manganite films deposited on $LaAlO_3$ give RBS spectra totally different from those deposited on Si (see for instance **Figure 3.1 (d)**). The fact that the La signal swamps the signals from the other elements makes it difficult or nearly impossible to measure the widths of these signals in order to determine film thickness. **Figure 3.5** simulated RBS spectra for the $LaAlO_3$ substrate without a deposited film (black) and a $LaAlO_3$ substrate with a $La_2CaMn_{2.94}Fe_{0.06}$ film 2000Å thick (in red) are shown. By measuring the width ΔE from the step of the La signal, the film thickness can be determined. A calibration curve in **Figure 3.6** gives the La step width as a function of the thickness for a $La_2CaMn_{2.94}Fe_{0.06}$ film deposited on a $LaAlO_3$ substrate.

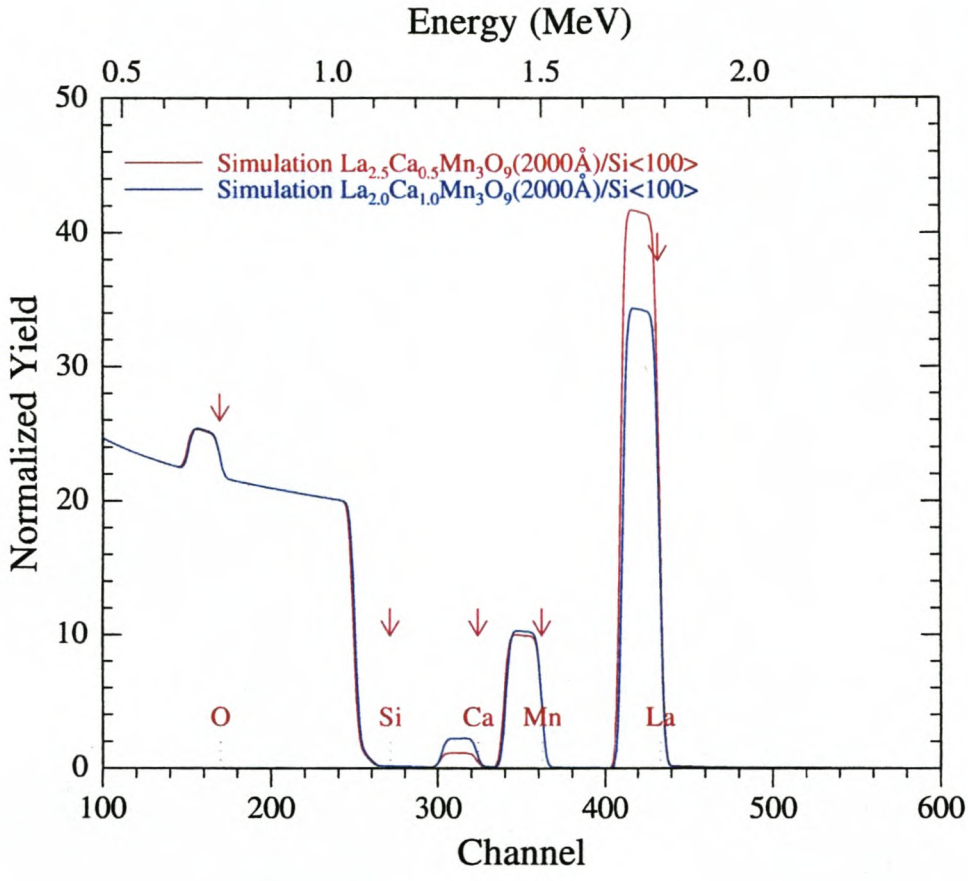

Figure 3.3: *Simulated RBS spectra of two films (2000Å thick), with different La and Ca concentrations, namely* $La_{2.0}Ca_{1.0}Mn_3O_9$ *(blue) and* $La_{2.5}Ca_{0.5}Mn_3O_9$ *(red). From the blue spectrum it can clearly be seen that the La signal has dropped by 20% and the Ca signal by 50%. Note that the Mn and O signals are the same for the two spectra as there is no change in their stoichiometry.*

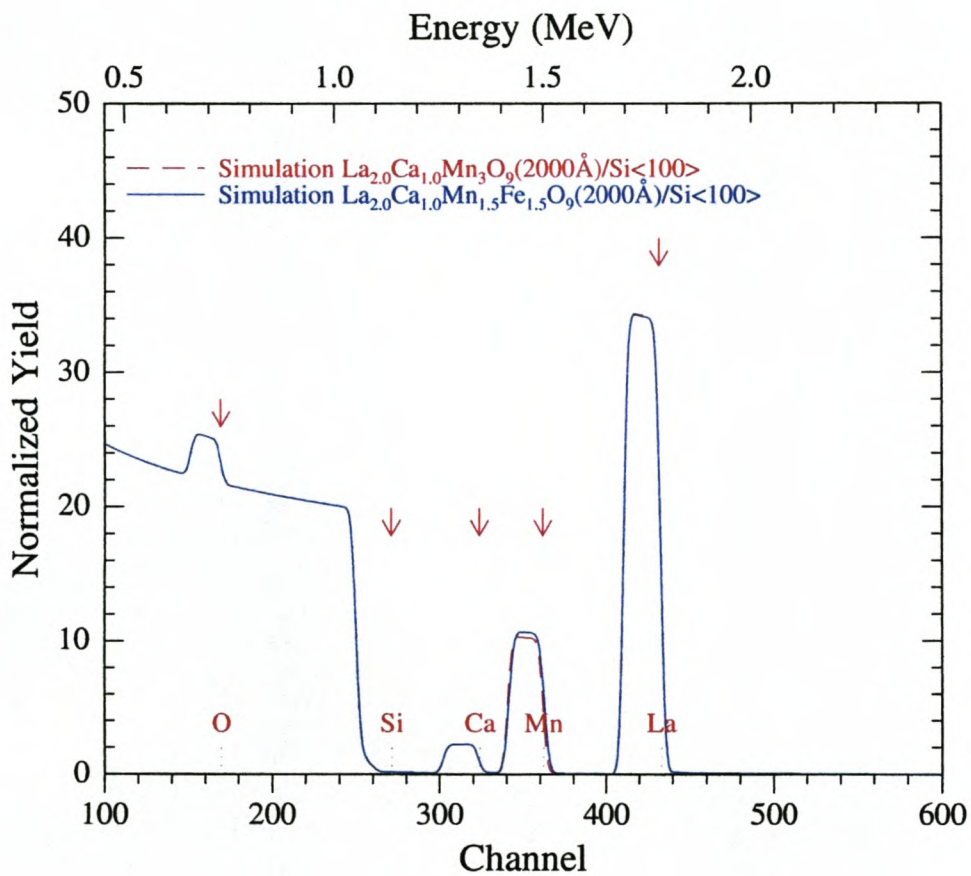

Figure 3.4: *Simulated RBS spectra of two films with different Mn and Fe concentrations. The red spectrum only contains Mn while the blue spectrum is for a film in which half of the Mn is replaced with Fe. It can clearly be seen that RBS cannot readily distinguish between Mn and Fe as their masses of 54.9 and 55.8 are too close to each other.*

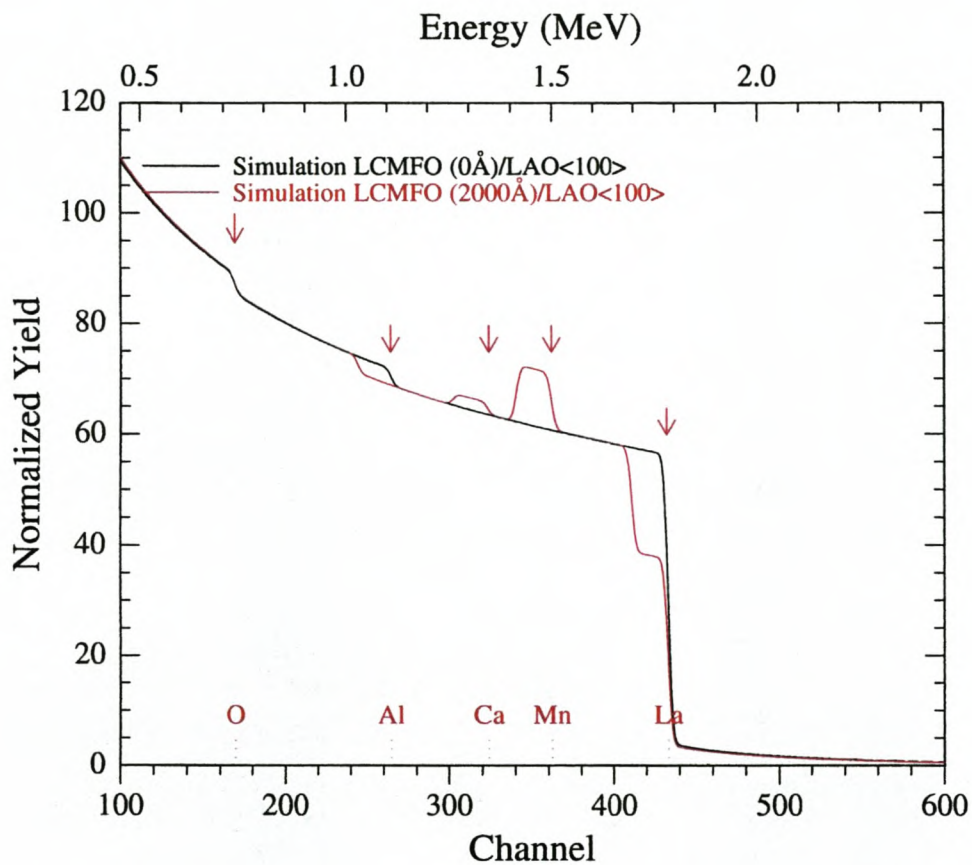

Figure 3.5: *Simulated RBS spectra for a $LaAlO_3$ (LAO) substrate (black) and for a LAO with a $La_2CaMn_{2.94}Fe_{0.06}O_9$ (LCMFO) film deposited on it with a thickness of 2000Å (red). It can clearly be seen that the thickness of the manganite film can be determined by measuring the width (ΔE) of the step caused by the La signal.*

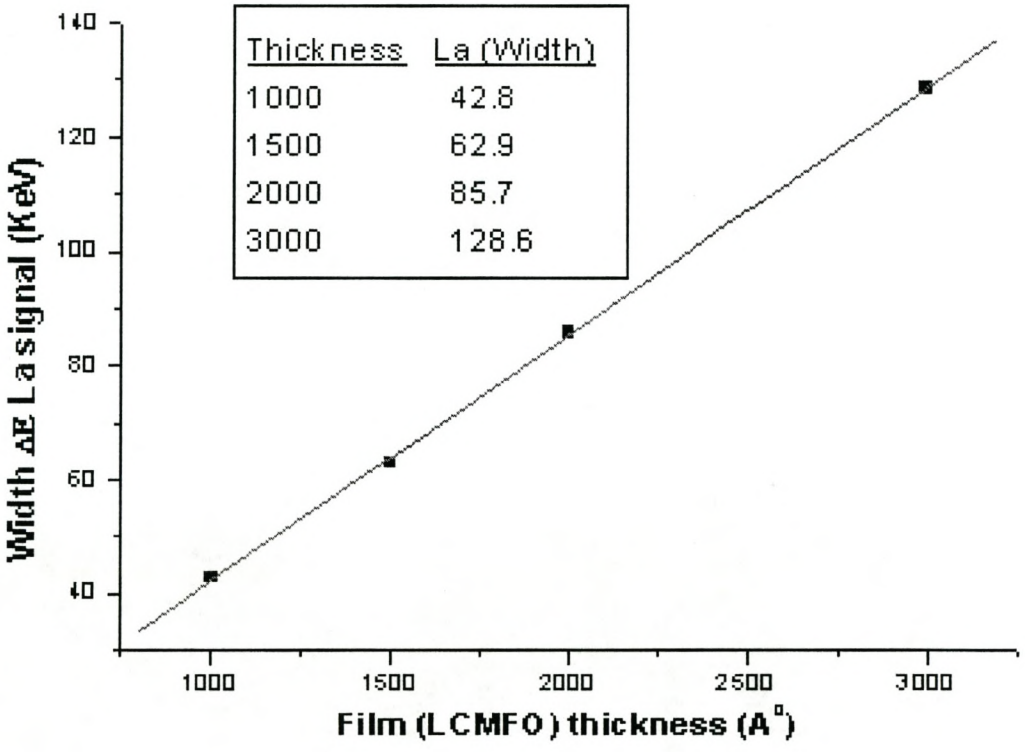

Figure 3.6: *The calibration curve giving the La step width as a function of the thickness for* $La_2CaMn_{0.6}Fe_{2.4}O_9$.

3.6 Summary

It has been shown that RBS is a very powerful characterization technique when used in conjunction with the RUMP simulation program. The effect of various parameters can be determined beforehand by RUMP simulation of the thin film structures to be investigated. After RBS spectra have been measured experimentally for the samples produced by pulsed laser deposition, RUMP simulation can be carried out in order to find the best fit with the experimental data.

Simulation of spectra obtained for manganite films on Si and MgO substrates show no overlapping of the Ca, Mn and La signals with signals from the substrate, because the substrate consists of lighter elements than those in the films. Some overlapping was however found for $SrTiO_3$ substrates but in these cases there was no overlapping with the La signal, due to its heavier mass. A lot of overlapping between $LaAlO_3$ substrates and the film occurs. It has however been shown that manganite film thickness can be determined by measuring the width of the step in the La signal.

Simulation shows that RBS is an excellent characterization tool for determining film thickness, using the width of either the La, Mn or Ca signal. It is ideally suited for thicknesses up to about $3000\mathring{A}$, as overlapping starts to occur for greater thicknesses. In such cases however, iterative simulation and fitting can be used. The height of RBS signals is an excellent measure of stoichiometry. Because the masses of Mn and Fe are so close to each other they cannot be distinguished. RBS therefore only gives a measure of the total Fe plus Mn content of the sample.

Chapter 4

Oxygen Uptake in $La_2CaMn_{3-x}Fe_xO_9$

4.1 Oxidation States in Manganites

The oxidation states of the elements in manganite materials have a large effect on their magnetoresistive properties. In **Table 4.1**, the different oxidation states are given.

Table 4.1: *Oxidation states of the elements in manganite materials (LCMFO)*

Element	Oxidation state
La	(+3)
Ca	(+2)
Mn	(+2)*, (+3), (+4), (+6), (+7)
Fe	(+2),(+3)*
O	(-2)

* *most stable oxidation state*

It can be seen that all the elements have just got one oxidation state except for Mn and Fe. The most oxygen that can be accommodated by the manganite thin films during pulsed laser deposition (PLD) will therefore occur when all the Mn and Fe are in their highest oxidation states namely +7 and +3, respectively. The least uptake of oxygen will occur for Mn and Fe in their lowest oxidation states, namely +2 and +2. The amount of oxygen will naturally depend on the relative amounts of Mn and Fe in the pulsed laser deposited thin films. The two target compositions used in this study were:

- $La_2CaMn_{0.6}Fe_{2.4}O_{9+x}$
- $La_2CaMn_{2.94}Fe_{0.06}O_{9+x}$

As an example, the oxygen uptake in the first mentioned composition is calculated.

4.1.1 Maximum oxygen uptake

Oxidation state Mn = (+7)
Oxidation state Fe = (+3)
$La_2Ca(Mn_{0.6}Fe_{2.4})O_{9+x}$
2(+3) 1(+2) 0.6(+7)2.4(+3) (9+x)(-2)
The total positive and negative charged states must balance therefore:
+6+2+4.2+7.2-18-2x =0
x = +0.7
When the most oxygen possible is taken up in the thin film the composition will be: $La_2CaMn_{0.6}Fe_{2.4}O_{9.7}$.

4.1.2 Minimum oxygen uptake

Oxidation state Mn = (+2)
Oxidation state Fe = (+2)
$La_2CaMn_{0.6}Fe_{2.4}O_{9+x}$

2(+3) 1(+2) 0.6(+2)2.4(+2) (9+x)(-2)

The total positive and negative charged states must balance therefore:

+6+2+1.2+4.8-18-2x =0

x = -2

When the least oxygen is taken up in the thin film the composition will be:

$La_2CaMn_{0.6}Fe_{2.4}O_{7.0}$.

4.2 Oxygen Measurement by RBS

The above calculations show that for a cation composition of $La_2CaMn_{0.6}Fe_{2.4}$, the oxygen content can vary from a minimum of $O_{7.0}$ to a maximum of $O_{9.7}$. In **Figure 4.1**, Rutherford backscattering spectra (RBS) simulated by using RUMP[51], (see also **Appendix C**) are given for these different oxygen concentrations. It can clearly be seen that the height of the La signal is considerably lower for magnetoresistive films with high oxygen content. This is due to the fact that the extra oxygen increases the energy loss of the alpha particles in the film, therefore spreading the La signal over a larger energy interval. The Mn(Fe) and Ca signals also drop by the same percentage as the La signal. The height of the La signal can therefore be used as a measure of the oxygen content of a film. The Ca or Mn(Fe) peak heights may also be used, but give less accuracy due to the smaller magnitude of their signals. A calibration curve for $La_2CaMn_{0.6}Fe_{2.4}O_{9+x}$ was constructed using the RUMP simulation programme and is given in **Figure 4.2**. By measuring the height of the La signal, the oxygen content of the film may be determined using such a calibration curve. The oxygen content of films may also be determined using an iterative simulation process, leading to the best fit between the measured and simulated RBS spectrum. From **Figure 4.3** it can be seen that an excellent fit is obtained for a simulated spectrum with a film thickness of 2500 $\AA$ and an oxygen content of $O_{9.0}$. The apparent bad fit at lower energies is due to channeling of alpha particles in the single crystal silicon substrate.

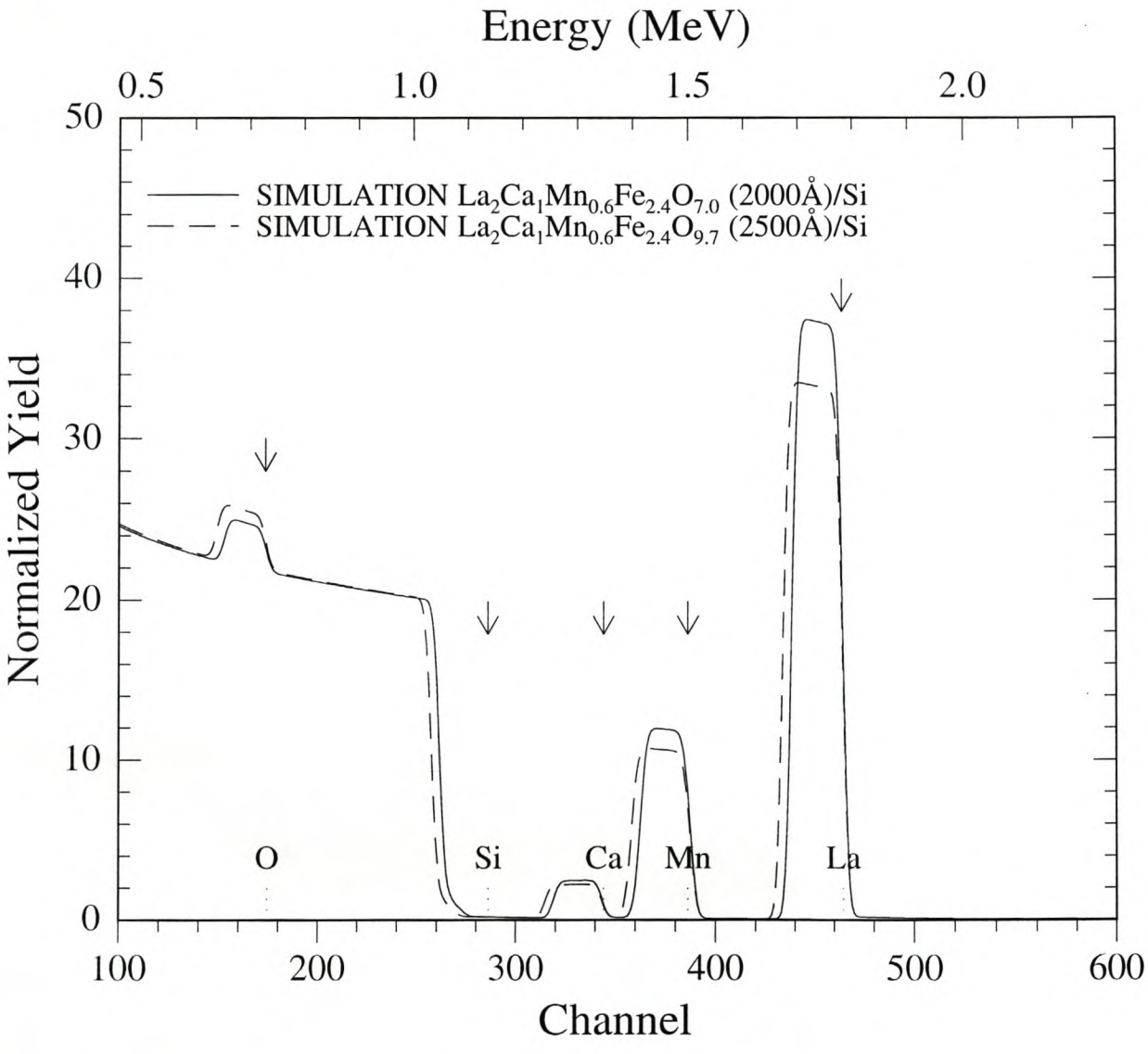

Figure 4.1: *Comparison of two simulated spectra showing the heights of the different elements in* $La_2CaMn_{0.6}Fe_{2.4}O_{9+x}$ *thin film. The highest signals correspond to the minimum oxygen uptake and the lowest signals correspond to the maximum oxygen uptake. Only the surface position (vertical arrows) of Mn is indicated in these spectra, because the masses of Mn and Fe are so close to each other, that they cannot be distinguished by RBS.*

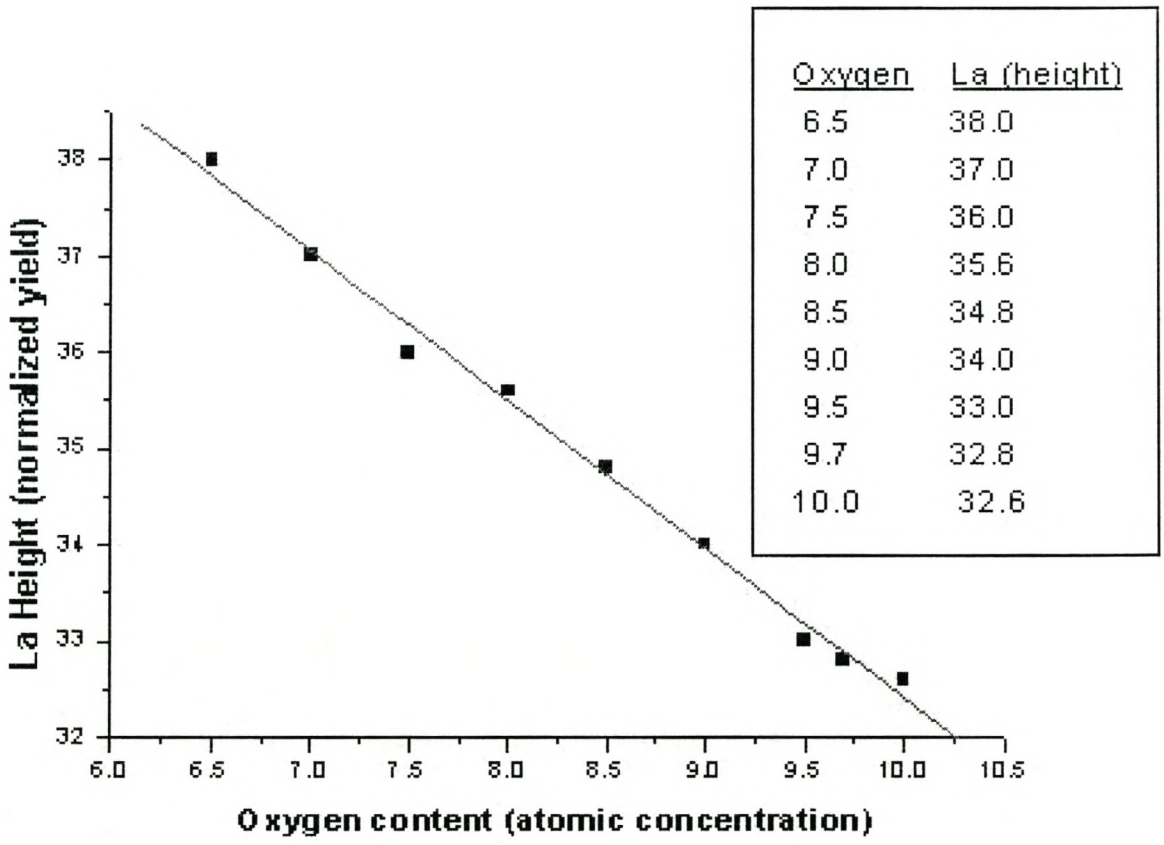

Figure 4.2: *The calibration curve giving the La height as a function of the oxygen content in* $La_2Ca(Mn_{0.6}Fe_{2.4})O_{9+x}$.

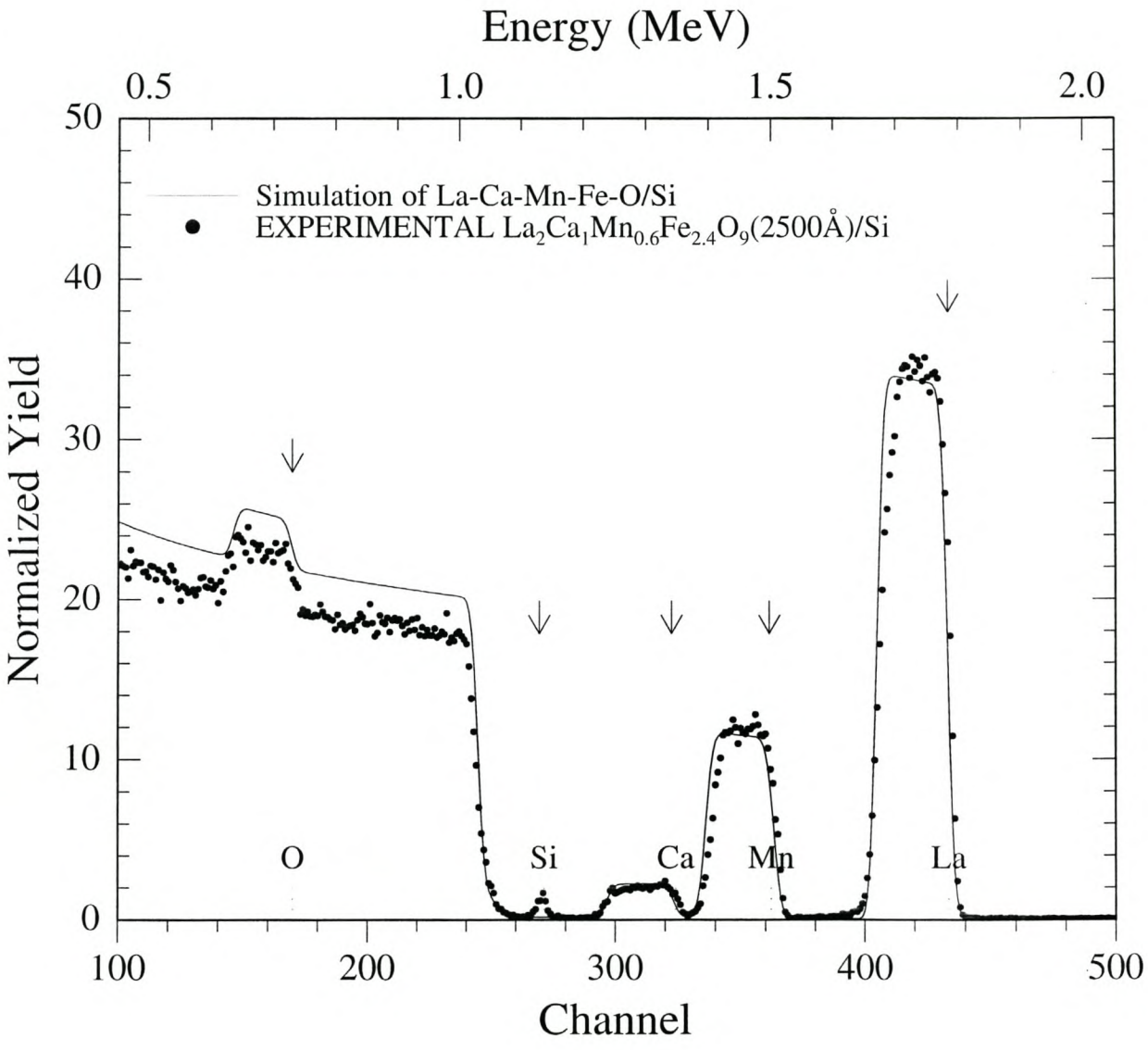

Figure 4.3: *Simulated spectrum compared with experimental spectrum of a manganite film deposited on a single crystal silicon substrate. The best fit is obtained for a simulated spectrum, with oxygen content equal to* $O_{9.0}$. *The film prepared by PLD therefore has the composition* $La_2Ca(Mn_{0.6}Fe_{2.4})O_{9.0}$, *with a film thickness of 2500 Å.*

The oxygen content determines the Mn valence, responsible for magnetotransport properties of manganites. Deficiency of oxygen leads to a reduction of carrier density resulting in suppressed ferromagnetic ordering. During laser ablation, the oxygen content may be controlled by adjusting the ambient pressure using a needle valve (see **Figure 2.1**). Pressures typically between 0.01 mbar and 1 mbar oxygen were used during pulsed laser deposition. It has been proven that after deposition, the films usually have an oxygen deficit, and postannealing in pure oxygen is needed to improve electrical and magnetic properties[56,57,58]. On the basis of this observation most of our samples were annealed after deposition for one hour under an oxygen pressure of 500 mbar and at 750^{o}C. In this study ozone was sometimes used to enhance oxygen content of the samples.

Chapter 5

Characterization of Samples Prepared by PLD

5.1 Introduction

5.1.1 Effect of magnetic field on bulk manganates

The application of a magnetic field up to 6 Tesla causes a significant decrease in the resistivity of bulk manganate perovskites. In $La_{1-x}A_xMnO_3$ samples (A is usually one of the bi-valent alkaline elements such as Ca, Sr or Ba), the decrease in resistivity (i.e. magnetoresistance, MR) is particularly observed in the compositions with $0.1 < x < 0.5$. MR is highest in the region of T_c (Curie temperature) or T_{im} (transition temperature from insulator to metal). The comparison of temperature variation of the resistivity of $La_{1-x}Ca_xMnO_3$ at 6 T with that at 0 T is shown in **Figure 5.1**. Magnetoresistance in manganates is generally negative and is highest around T_c or T_{im}. CMR close to 100% has been observed in many polycrystalline and single crystal $La_{1-x}A_xMnO_3$ compositions, but the applied magnetic field is quite high (5-6 T). Self-doped $LaMnO_3$ samples with sufficient Mn^{4+} content ($La_{1-\delta}Mn_{1-\delta}O_3$) exhibit CMR similar to that observed in $La_{1-x}A_xMnO_3$ compositions. In **Figure 5.2**, the behavior of $La_{0.945}Mn_{0.945}O_3$, with 33 % Mn^{4+} is shown. Besides the magnetic field, the effect of particle size on the electron transport and magnetic properties of polycrystalline manganate perovskites has been investigated. The results show that the magnetoresistance is insensitive to particle size although T_c decreases with decreasing particle size.

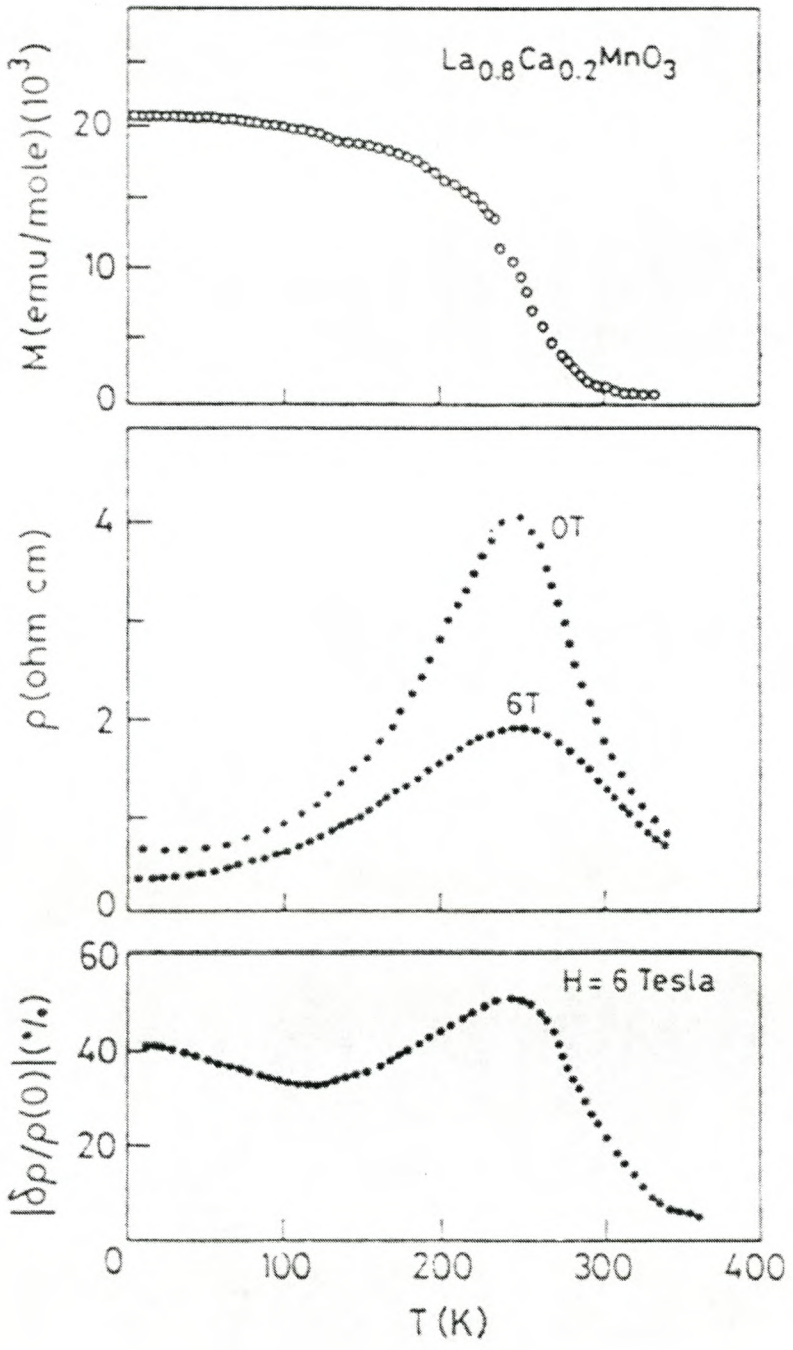

Figure 5.1: *Temperature variation of magnetization, resistivity (at H=0 T and H=6 T) and magnetoresistance of polycrystalline $La_{0.8}Ca_{0.2}MnO_3$ (adapted from Mahendiran et al[59]).*

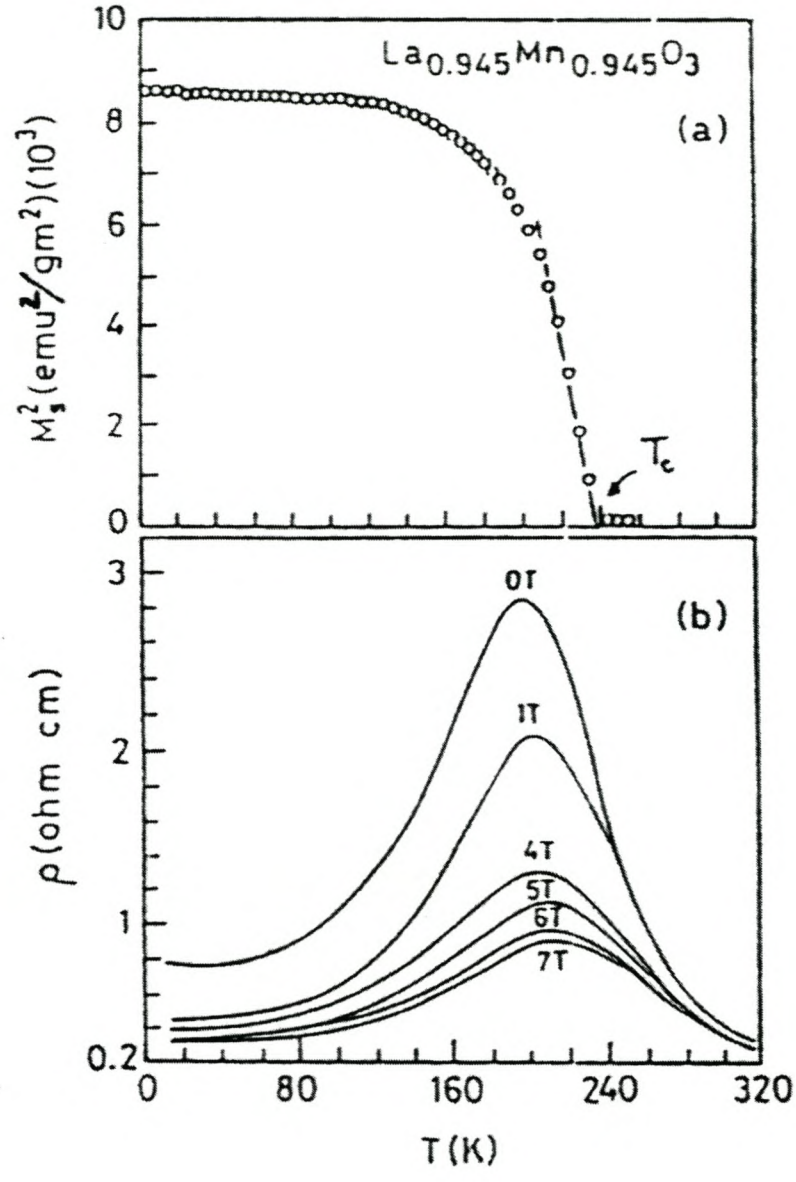

Figure 5.2: *(a) Magnetization data of polycrystalline* $La_{0.945}Mn_{0.945}O_3$ *(b) resistivity-temperature plots for polycrystalline* $La_{0.945}Mn_{0.945}O_3$ *at different magnetic fields (after Mahendiran et al[59].*

This feature is shown in **Figure 5.3** where the I-M transition becomes broader when the particle size is small, but the % MR is nearly a constant over a wide temperature range.

5.1.2 Effect of magnetic field on thin film manganates

In 1993, von Helmholt et al.[13] reported a large negative magnetoresistance effect, of the order $\Delta R/R(H = 0) > 60\%$ at room temperature in a 7-tesla field, in $La_{0.67}Ba_{0.33}MnO_3$ epitaxially thin films made using pulsed laser deposition in an off-axis geometry followed by a postannealing. A typical annealing condition involves a high-temperature (around 900^0C) short-time (about 30 minutes) treatment in an oxygen atmosphere. This achievement opened up new possibilities for applications in diverse areas of technology such as magnetic random access memories and read heads for hard disk drives. The results are shown in **Figure 5.4**.

5.1.3 Literature summary

Table 5.1 gives a summary of some results on efforts of synthesizing the doped manganate perovskites using pulsed laser deposition and other techniques such as reactive sputtering, reactive ion beam sputtering, and molecular beam epitaxy (MBE). From this table, it's interesting to note that the pulsed laser deposition is the main technique used to get thin films.

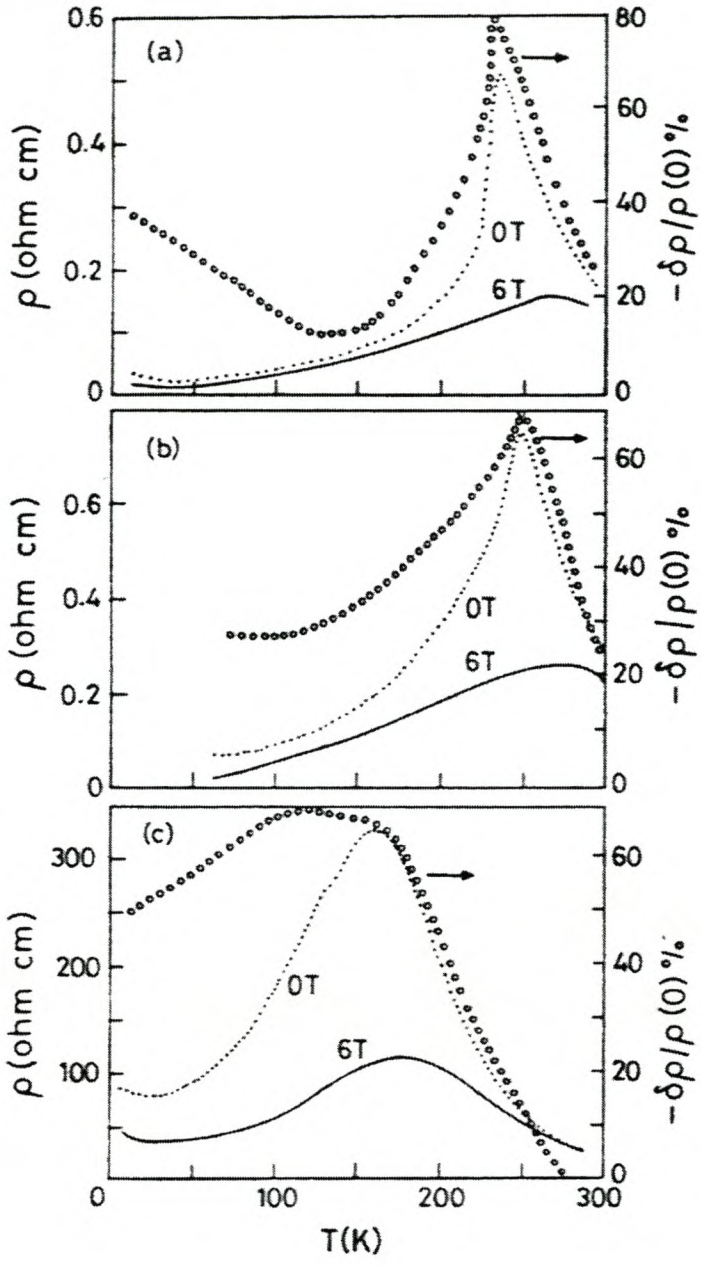

Figure 5.3: *Temperature variation of resistivity (at 0 T and 6 T) and magnetoresistance of* $La_{0.7}Ca_{0.33}MnO_3$ *with particle diameters of (a) 3.5 μm (b) 1.5μm and (c) 0.025μm (from Mahesh et al[60]).*

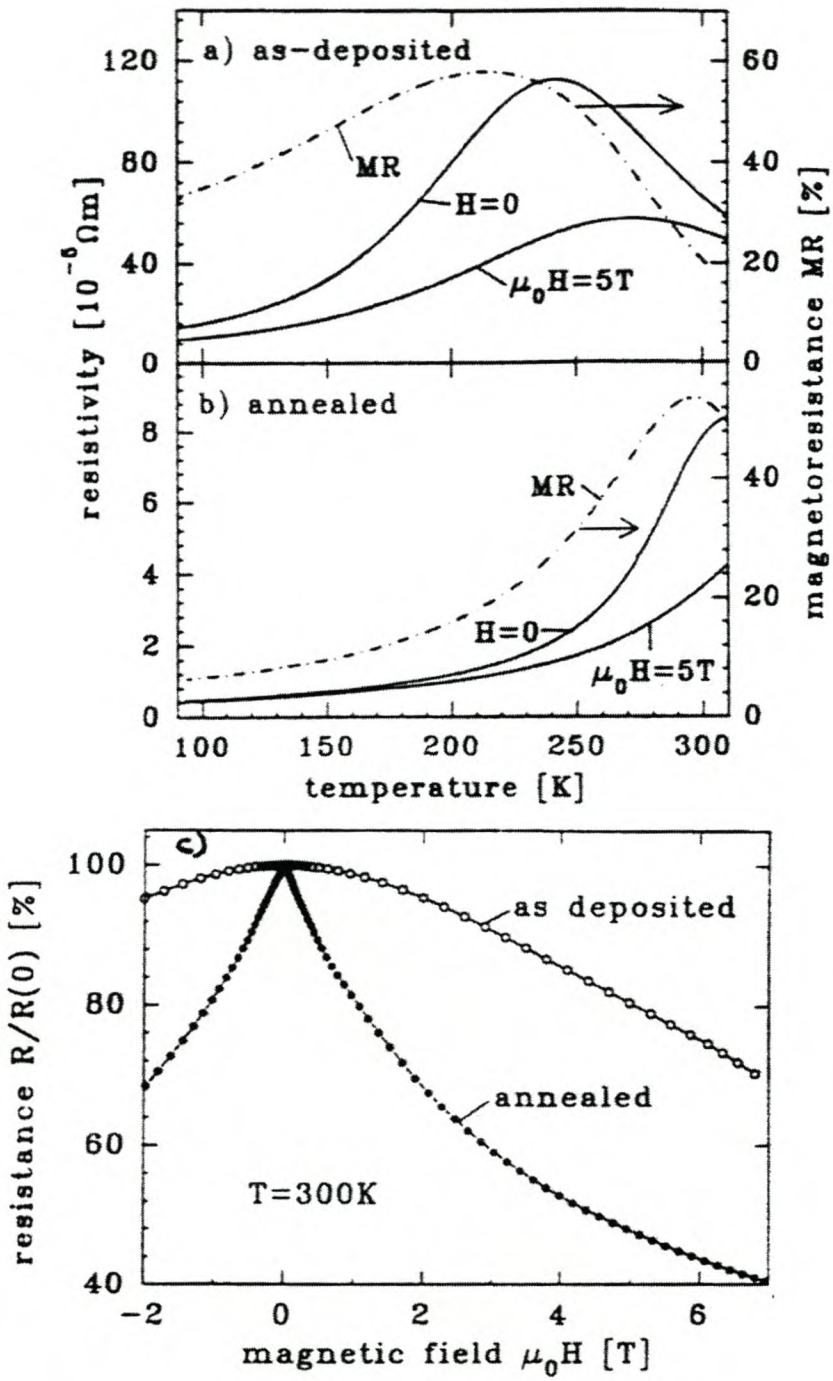

Figure 5.4: *First report of large magnetoresistance in* $La_{0.7}Ba_{0.3}MnO_3$ *thin films. Temperature dependence of the resistivity at zero field and an applied magnetic field of* $\mu_o H$ *= 5 T (a) as-deposited at* T_S*=600°C, (b) after a subsequent annealing at* T_A*= 900°C for 12 h; the dashed line represents the relative magnetoresistance effect and (c) resistance versus field curves for the as-deposited sample (*T_S*=600°C) and after annealing at* T_A *= 900°C for 12 h, measured at T= 300K[13].*

Table 5.1: *Some recent results on thin-film CMR materials. T_c denotes the Curie temperature, room-temperature resistivity is denoted as ρ_0 $(\Omega - cm)$, and magnetoresistance by $\Delta R/R(H)$.*

Material	Deposition	Substrate	$T_c(K)$	$\rho_0(\Omega - cm)$	$\Delta R/R(H)$	Ref
$La_{0.7}Ba_{0.3}MnO_3$	PLD	$SrTiO_3(100)$	~ 300	3×10^{-4}	150% (7 T)	[13]
$La_{0.67}Ca_{0.33}MnO_3$	PLD	$LaAlO_3(100)$	~ 100	N/A	1.25×10^5% (6 T)	[16]
$Nd_{0.7}Sr_{0.3}MnO_3$	PLD	$LaAlO_3(100)$	~ 95	2×10^{-2}	3340% (5 T)	[61]
$La_{0.67}Ca_{0.33}MnO_3$	PLD	$LaAlO_3(100)$	~ 110	N/A	1.1×10^6% (6 T)	[62]
$La_{0.74}Pb_{0.26}MnO_3$	rf sputter	Si (100)	325	3×10^2	30% (2 T)	[63]
$La_{0.67}Ca_{0.33}MnO_3$	dc sputter	MgO (100)	86	12	460% (0.82 T)	[64]
$La_{0.67}Ca_{0.33}MnO_3$	dc sputter	MgO (100)	226	$< 10^{-3}$	130% (0.82 T)	[64]
$La_{0.58}Ca_{0.42}MnO_3$	MBE	$SrTiO_3(100)$	234	N/A	900% (5.5 T)	[65]
$La_{0.75}MnO_3$	PLD	$SrTiO_3(100)$	255	2×10^4	425% (4 T)	[66]
$La_{0.67}Sr_{0.33}MnO_3$	PLD	Si(100)	~ 120	$\sim 4x10^{-2}$	250% (5 T)	[67]

5.2 Deposition Parameters - Pulsed Laser Deposition (PLD)

The $La_2Ca(Mn_{0.6}Fe_{2.4})O_9$ and $La_2Ca(Mn_{2.94}Fe_{0.06})O_9$ thin films were deposited on Si, $LaAlO_3$, MgO, and $SrTiO_3$ single crystals. During PLD, all parameters were maintained fixed except the oxygen partial pressure which varied between 0.01 and 1 mbar, corresponding to the optimum range for magnetoresistive materials. **Table 5.2** gives the fixed values used during PLD.

Table 5.2: *Fixed values used during PLD*

Laser energy	400 mv (~182 mJ)
Energy density	~3.0 J/cm^2
Target-substrate distance	40 mm
Substrate temperature	750^{o}C
Number of pulses	2000
Deposition time	4 min
Annealing temperature	750^{o}C

The thin film deposition procedure can be summarized in the following main steps:

1. Mount the substrate on the substrate holder using silver paint.
2. Pump the vacuum chamber for at least 4 hours to get a base pressure of 2×10^{-6} mbar. Pressure of 1×10^{-6} mbar was reached by pumping for about 12 hours.

3. Heat the substrate up to 750^{o}C.

4. Switch on the excimer laser system.

5. Measure and adjust laser energy. Laser energy was measured with a pyroelectric detector. This detector produces a voltage pulse for each laser pulse incident on it's surface, and the voltage pulse's peak height is proportional to laser pulse energy. By recording a series of pulses on a storage oscilloscope, the average pulse energy could be determined. The laser fluence, F can be calculated from the following expression:

$$P_L = F \times A \times C(1 + eff), \tag{5.1}$$

where P_L is the laser energy, A the surface area of the beam spot, C the conversion constant at the laser power meter, and eff the power loss through the lens. F is expressed in J/cm^2, and A in cm^2. C is equal to 2.2 and eff to 0.34. The fluence used during our depositions was about 3 J/cm^2.

6. Introduce oxygen in the vacuum chamber by means of a needle valve to the desired partial pressure.

7. Switch on the target rotator.

8. Pre-ablate target for 2 minutes.

9. Deposit the thin film for a desired time deposition.

10. Annealing. Increase oxygen pressure to 500 mbar for 1 hour.

11. Switch off the heater, allowing the substrate to cool approximately to 60^{o}C.

12. Break vacuum to dry nitrogen

13. Open vessel to remove the deposited sample.

5.3 Thickness and Stoichiometry - RBS

The RBS spectra of films deposited on single crystal silicon substrates at different ambient pressures are shown in **Figure 5.5**. It can be observed that the fit is improving from lower to higher pressures. The best fit is obtained at 0.5 mbar. From the spectra, it can also be seen that backscattered alpha particles from heavy atoms are at higher energies. The heaviest element is lanthanum and the lightest is oxygen. The spectra obtained using

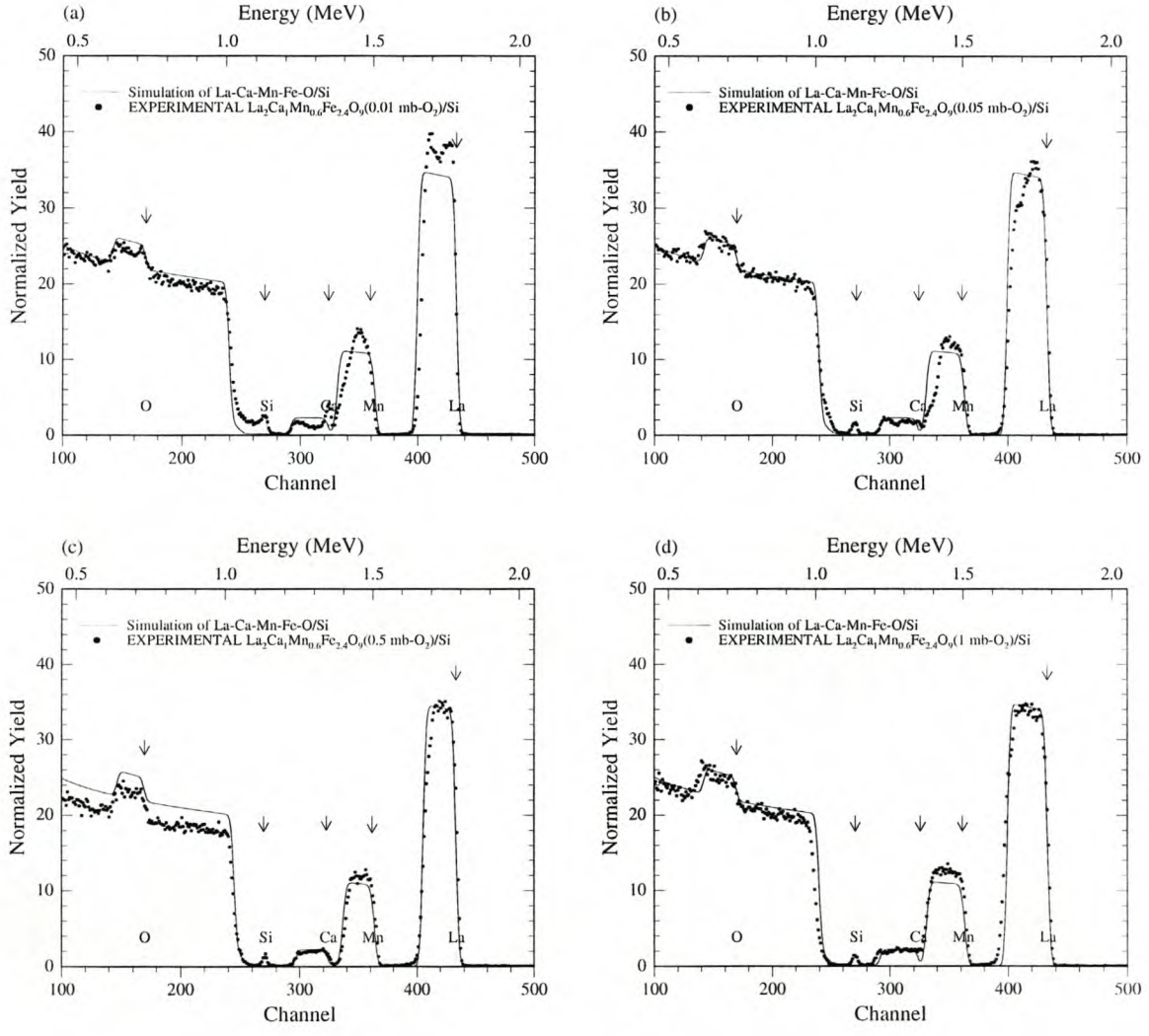

Figure 5.5: *RBS spectra of manganite films deposited on Si< 100 > substrates at different oxygen ambient pressures. (a) 0.01 mbar (b) 0.05 mbar (c) 0.5 mbar and (d) 1 mbar. The vertical arrows in each RBS spectrum give the surface energy position of each element*

single crystal $LaAlO_3$ substrates have profiles very different from those deposited on Si substrates (see **Figure 5.6**). This difference is attributed to the presence of lanthanum in the substrate. La is the heaviest element in the sample and therefore causes a high background continuum which swamps the signals from the other elements. The spectra

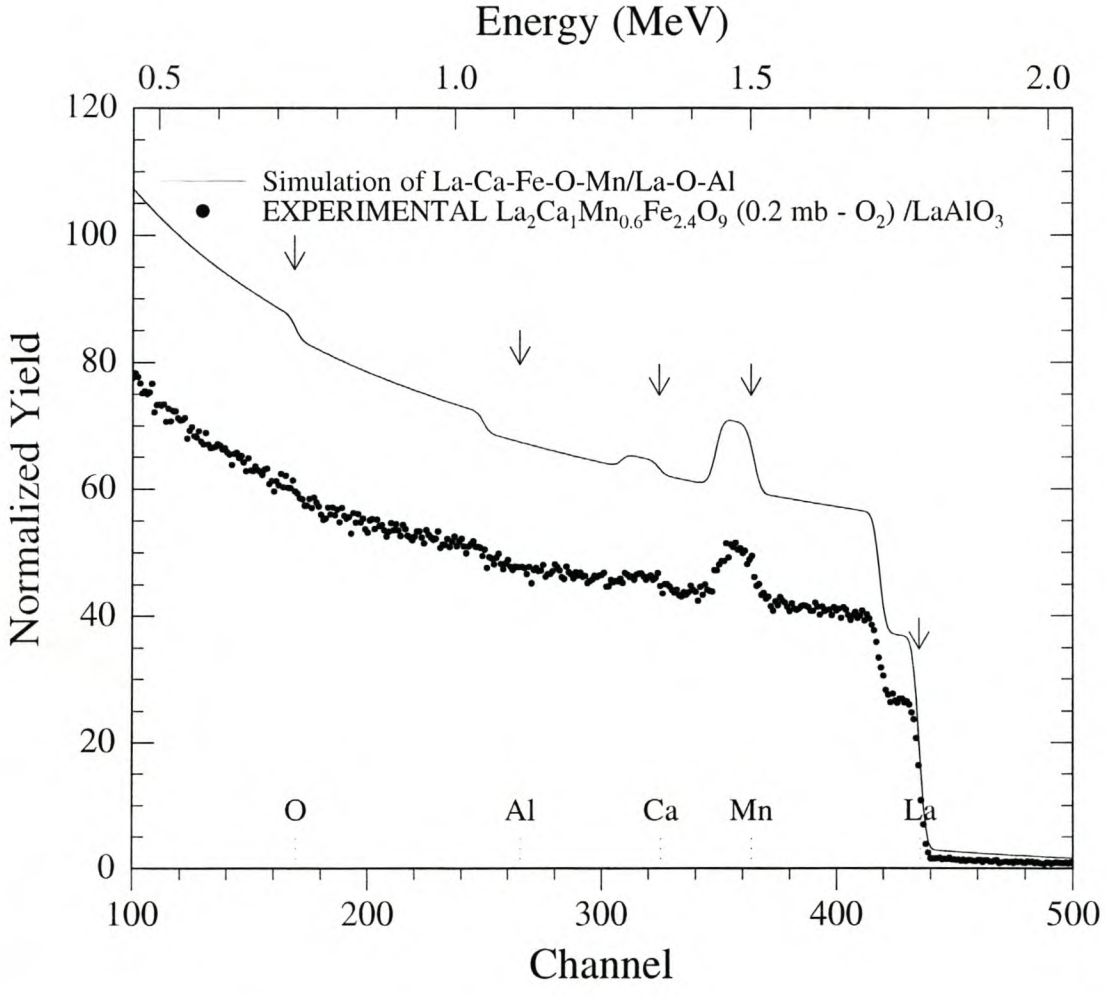

Figure 5.6: *RBS spectra of $La_2CaMn_{0.6}Fe_{2.4}O_9$ thin film deposited on $LaAlO_3$ single crystal substrate. Solid line is a simulated spectrum and dots the measured spectrum. The gap between the two spectra is due to the channeling effect.*

from MgO and $SrTiO_3$ single crystal substrates are shown in **Figure 5.7** and **Figure 5.8**.

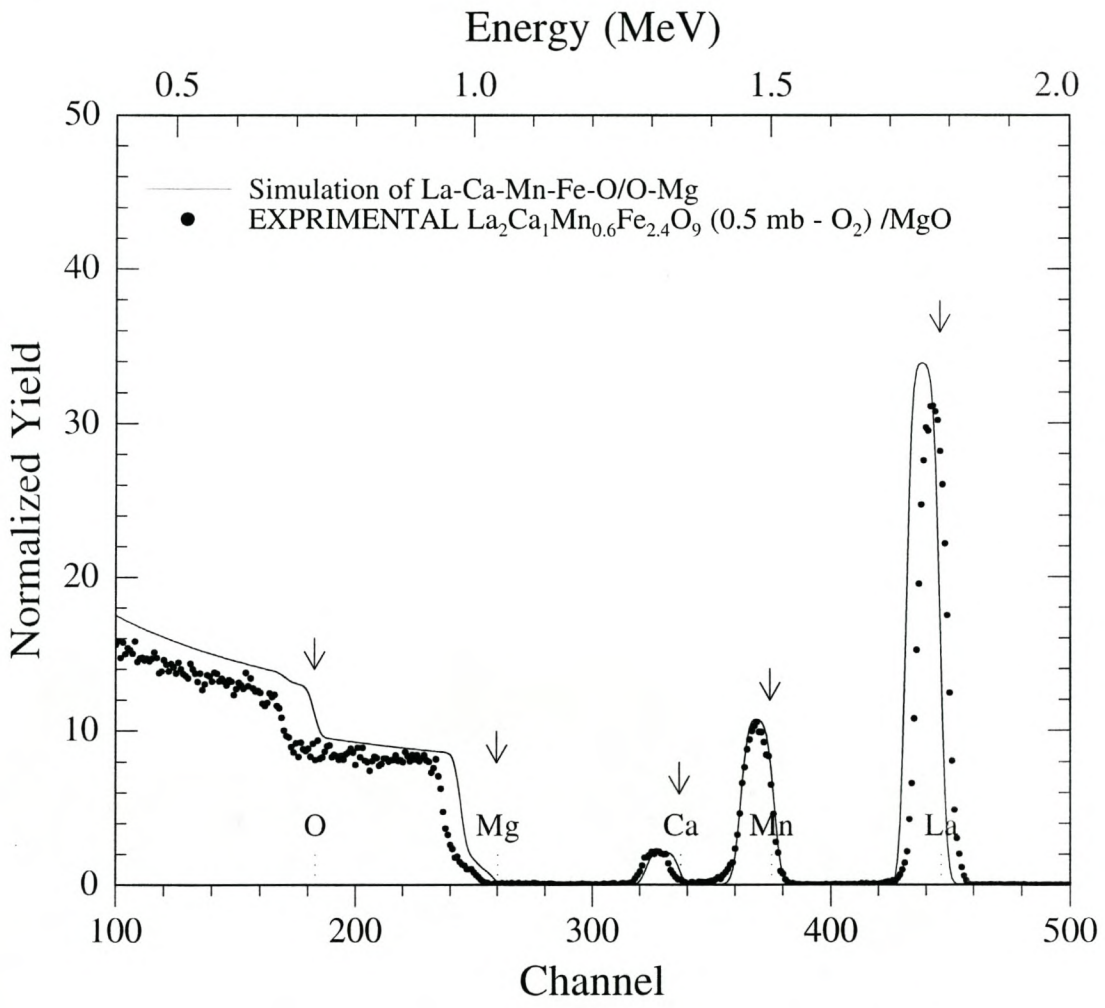

Figure 5.7: *RBS spectra of $La_2CaMn_{0.6}Fe_{2.4}O_9$ thin film deposited on MgO single crystal substrate.*

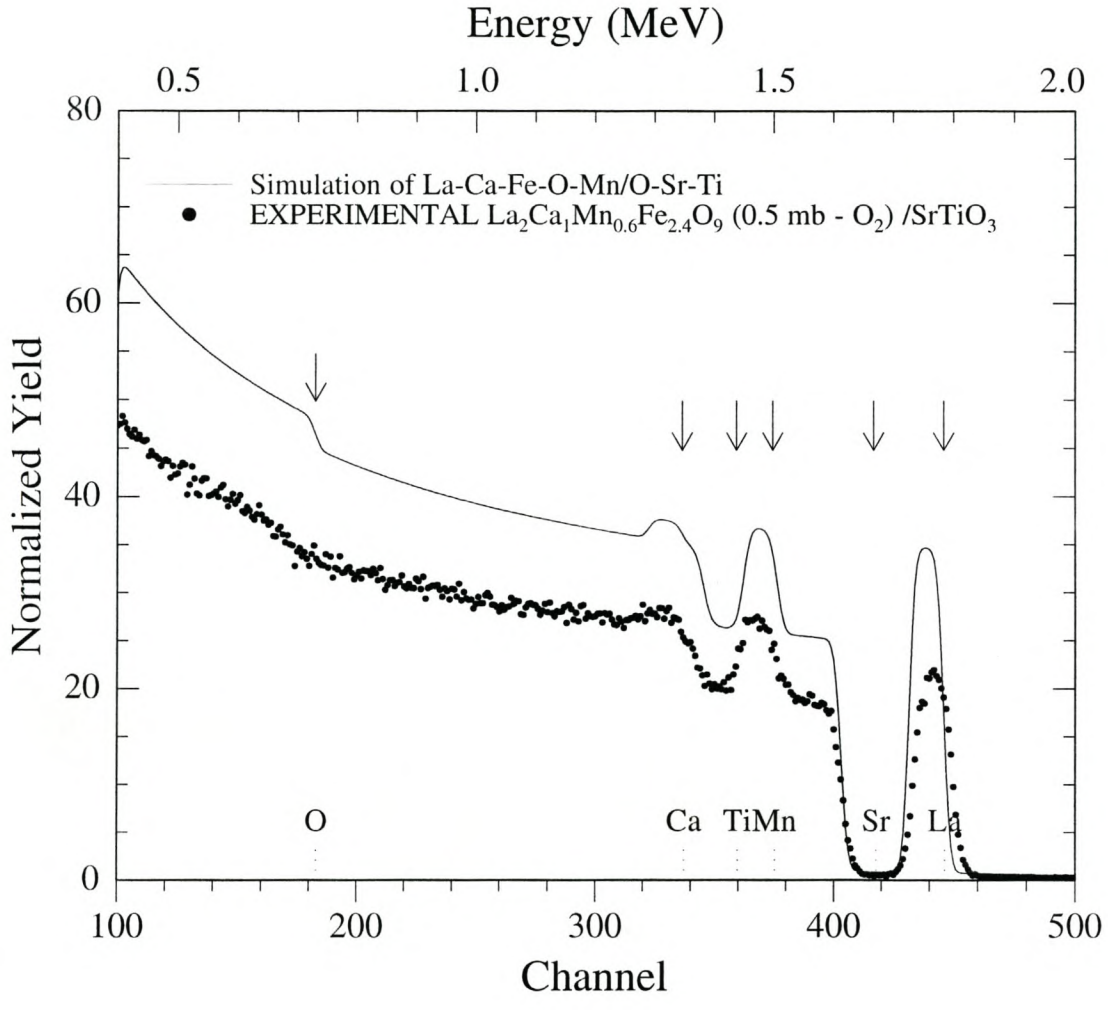

Figure 5.8: *RBS spectra of $La_2CaMn_{0.6}Fe_{2.4}O_9$ thin film deposited on $SrTiO_3$ single crystal substrate. The gap between the simulated spectrum and the measured spectrum is due to the channeling effect.*

5.4 Surface Roughness - AFM

Atomic force microscopy was used to determine the roughness of the thin films. The results from non-annealed and annealed films, with magnified area of 50 μm$\times$ 50μm are presented. The non-annealed film (**Figure 5.9**) and the annealed film (**Figure 5.10**) differ slightly in terms of boulders. These boulders are the consequence of the droplets formed due to splashing during PLD (see **section 1.4.3**). Their size vary between roughly 1 μm and 7μm. It can also be seen that the surface roughnesses of the two samples are different. The annealed film (average roughness 4.5 nm) shows a surface smoother than the non-annealed film (average roughness 5.3 nm) (also see **section 2.2.3**).

5.5 Surface Morphology - SEM

The SEM was also used to characterize the samples. Here we show the results obtained for thin films prepared from the two target compositions used during our experiments, namely $La_2Ca(Mn_{0.6}Fe_{2.4})O_9$ and $La_2Ca(Mn_{2.94}Fe_{0.06})O_9$. As it can be seen, the two samples are quite different in terms of polycrystallinity. In the case of samples having a high Fe content (**Figure 5.11**), the crystallinity size varies between about 0.04 μm and 0.10 μm. In the case of a high manganese content (**Figure 5.12**), the crystallinity varies between 0.03 μm and 0.06 μm.

5.6 Structure and Phase Identification - XRD

Manganites samples were analyzed using Bragg-Brentano (2θ) X-ray diffraction (see section 2.2.2). The samples were deposited on various single crystal substrates, namely Si$<$ 100 $>$, MgO$<$ 100 $>$, $SrTiO_3<$ 100 $>$ and $LaAlO_3<$ 100 $>$. The expected XRD reflections from these substrates are given in **Appendix B**. Reflections measured from manganite samples deposited on these substrates by PLD are summarized in **Table 5.3**.

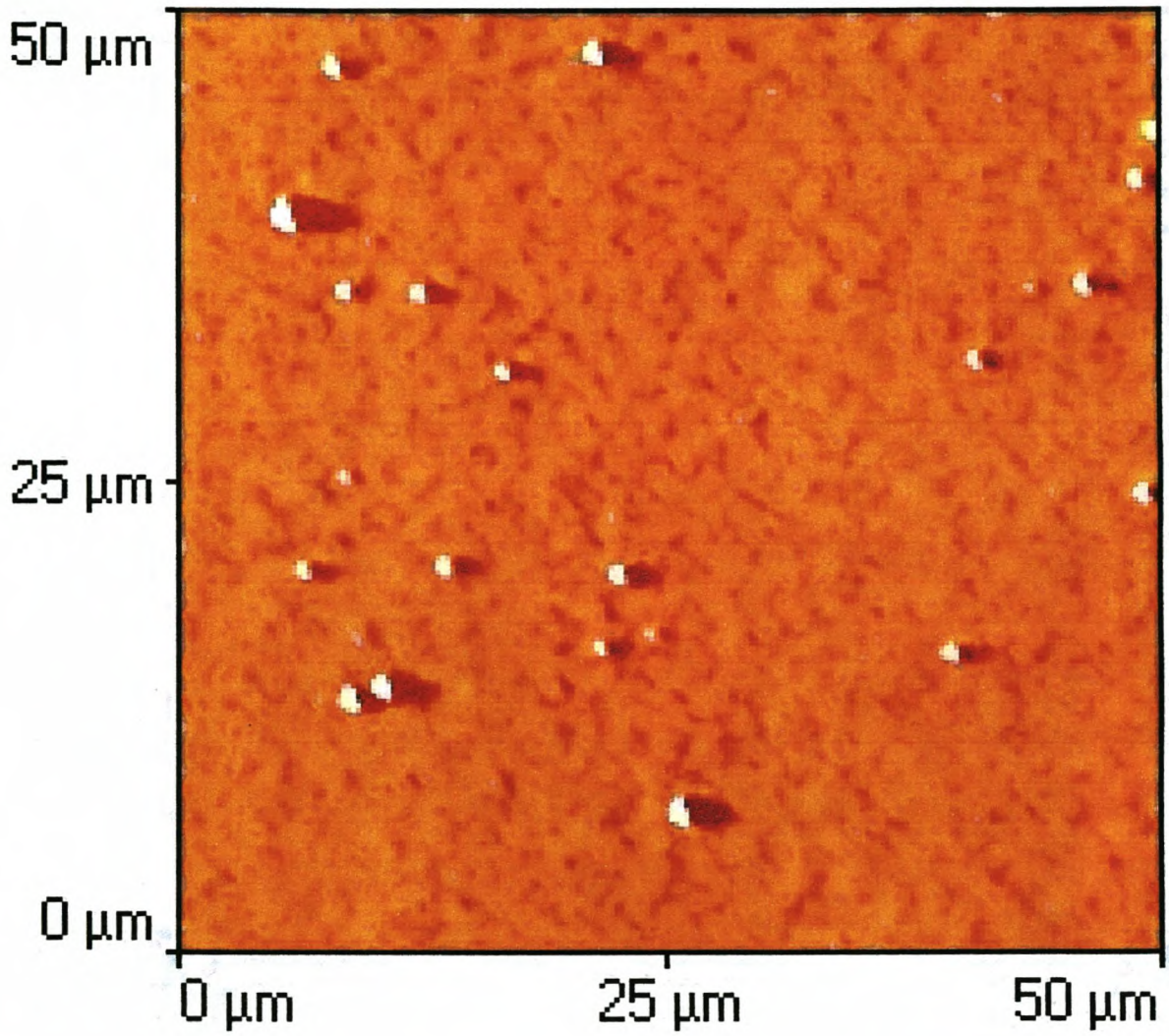

Figure 5.9: *$La_2Ca(Mn_{0.6}Fe_{2.4})O_9$ thin film deposited on Si substrate, without annealing after deposition.*

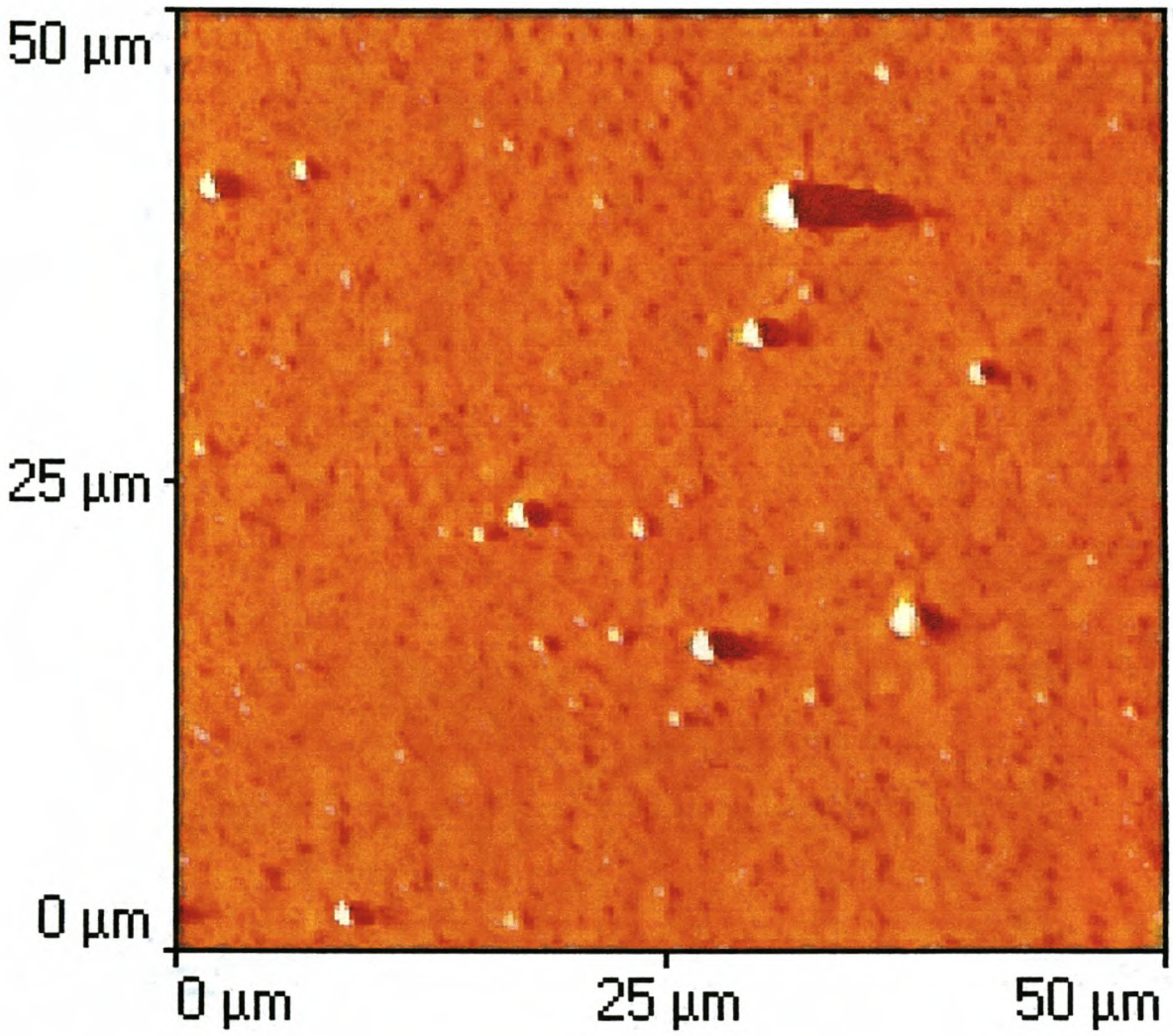

Figure 5.10: *$La_2Ca(Mn_{0.6}Fe_{2.4})O_9$ thin film deposited on Si substrate with annealing after deposition.*

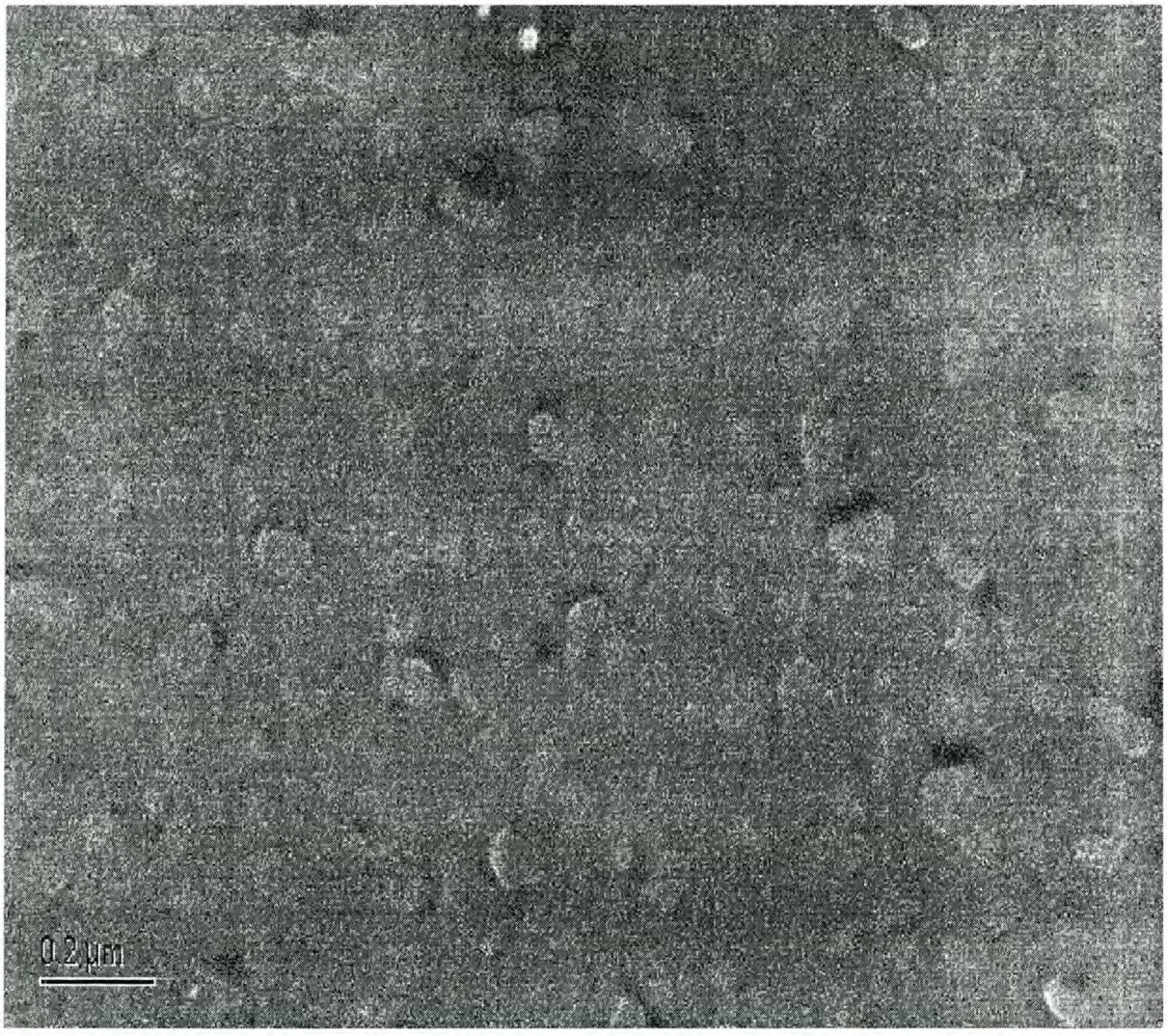

Figure 5.11: *SEM micrograph of* $La_2Ca(Mn_{0.6}Fe_{2.4})O_9$ *thin film prepared by laser ablation onto a heated (750°C)* $LaAlO_3$ *substrate at a partial pressure of 0.5 mbar oxygen. The scale bar represents 0.2 µm.*

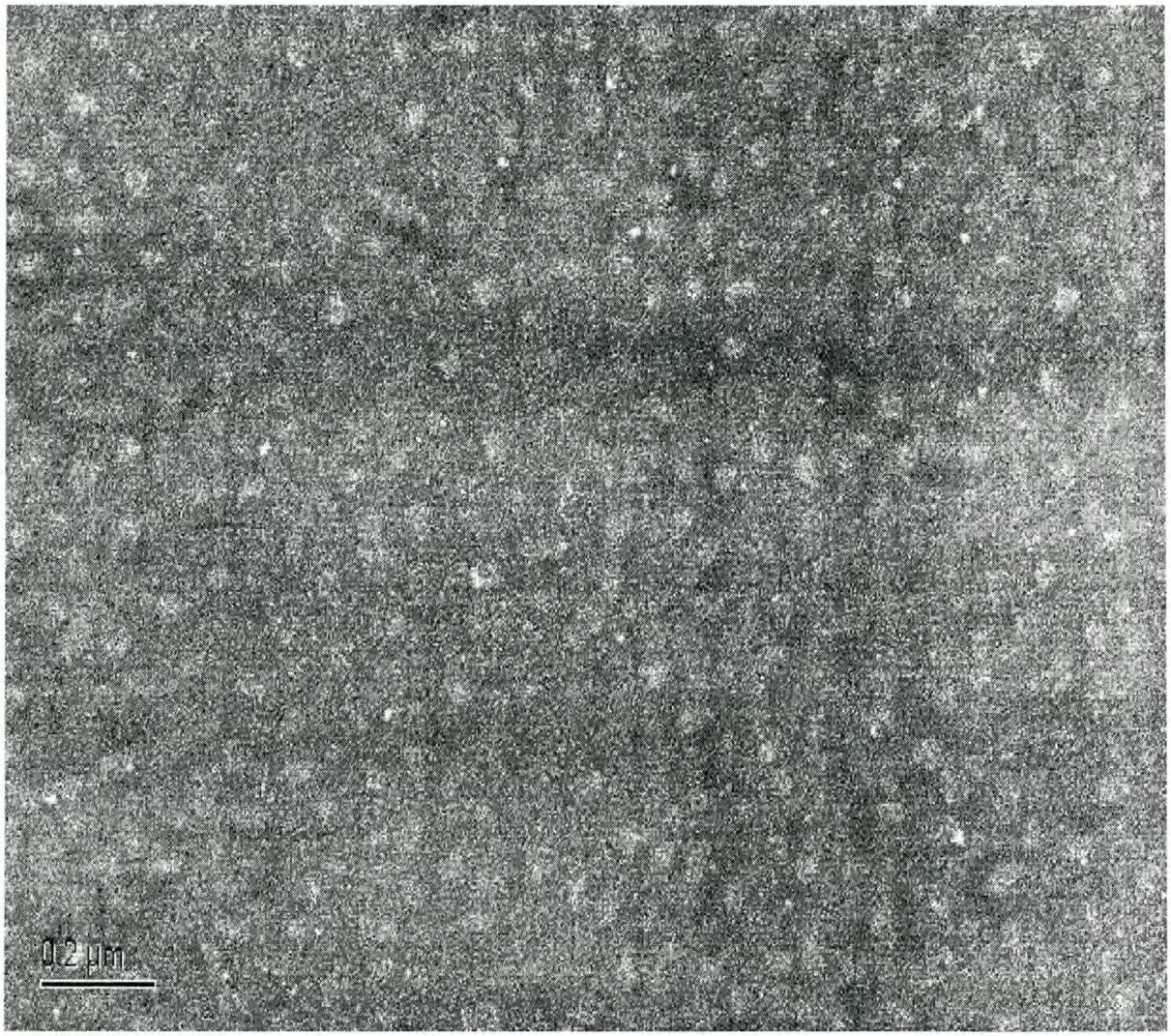

Figure 5.12: *SEM micrograph of* $La_2Ca(Mn_{2.94}Fe_{0.06})O_9$ *thin film prepared by laser ablation onto a heated (750°C)* $LaAlO_3$ *substrate at a partial pressure of 0.5 mbar oxygen. The scale bar represents 0.2* μm.

In **Figure 5.13** an XRD spectrum is shown for a thin film deposited onto silicon. Apart from the main Si< 100 >, very few reflections from the film can be seen. This is probably due to the fact that manganite films cannot be grown epitaxially on single crystal Si< 100 > due to a large lattice mismatch. We can also therefore conclude that the Fe-rich manganite has also not grown epitaxially on the MgO (200) substrate (see **Figure 5.14**). In the case of $SrTiO_3$ several reflections from the film can be seen, indicating reasonable epitaxial growth (**Figure 5.15**). The XRD spectra for manganite films deposited onto single crystal $LaAlO_3$ (LAO) substrates are given for both Fe-rich and Mn-rich manganites in **Figure 5.16** and **Figure 5.17** respectively. Several reflections from the film are observed and the sharpness also indicates relatively good epitaxy. It is interesting to note that the reflections from the film differ slightly from the substrate reflections. This feature is especially very observable in the case of Mn-rich (**Figure 5.17**) film and can be ascribed to a slight difference in lattice parameter between film and substrate and to stress effects. Our SEM measurements of these samples (see **Figure 5.11** and **Figure 5.12**) however show considerable crystallinity. Complete epitaxy has thus not occurred, but many grains have an epitaxial orientation.

Table 5.3: *Measured x-ray reflections from manganite films prepared by PLD.*

Substrate	2θ	(hkl)	material	Substrate	2θ	(hkl)	material
Si	66.8^o	-	substrate	**$LaAlO_3$**	22.8^o	-	film
	69.2^o	(100)	substrate		23.4^o	(100)	substrate
	69.4^o	-	film		23.7^o	-	film
MgO	23.0^o	-	film		42.6^o	-	film
	41.0^o	-	film		44.9^o	-	film
	42.8^o	(200)	substrate		45.6^o	-	film
	47.0^o	-	film		47.0^o	-	film
$SrTiO_3$	22.8^o	-	film		47.5^o	(200)	substrate
	44.8^o	-	film		70.7^o	-	film
	46.8^o	(200)	substrate		73.2^o	-	film
	47.2^o	-	film		73.8^o	(300)	substrate
	72.4^o	-	film		74.2^o	-	film
	72.8^o	-	film				

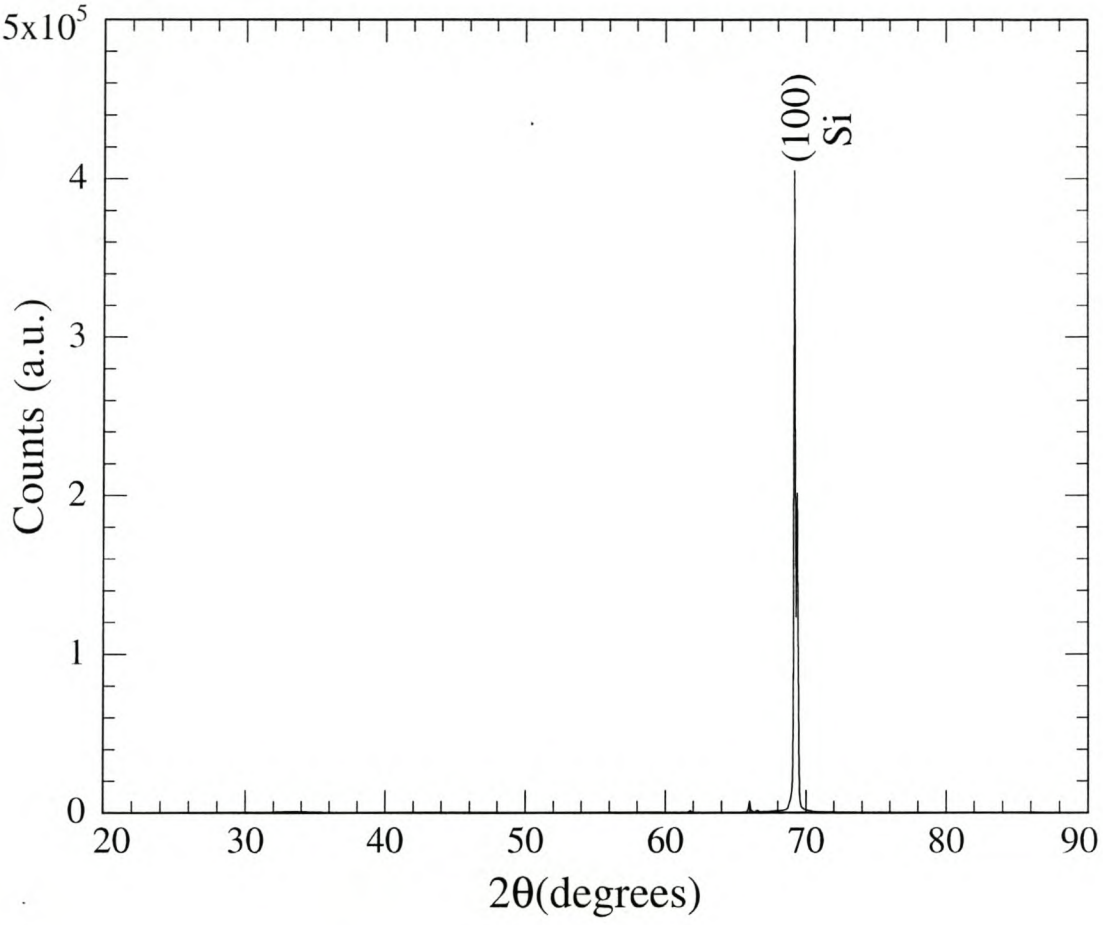

Figure 5.13: *XRD spectrum of* $La_2Ca(Mn_{0.6}Fe_{2.4})O_9$ *thin film deposited on* $Si< 100 >$ *single crystal.*

5.7 Electrical and Magnetic Measurements

Due to experimental problems encountered at Wits University for the electrical and magnetic measurements, very few measurements could be done. However, the resistance versus temperature (from room temperature to about 100 K) (**Figure 5.18**) in zero applied magnetic field was measured for a $La_2Ca(Mn_{0.06}Fe_{2.4})O_9$ thin film. It can be seen from the curve obtained, that a maximum resistance corresponds to about 108 K. At higher temperatures the resistance decreases as temperature increases. The manganite

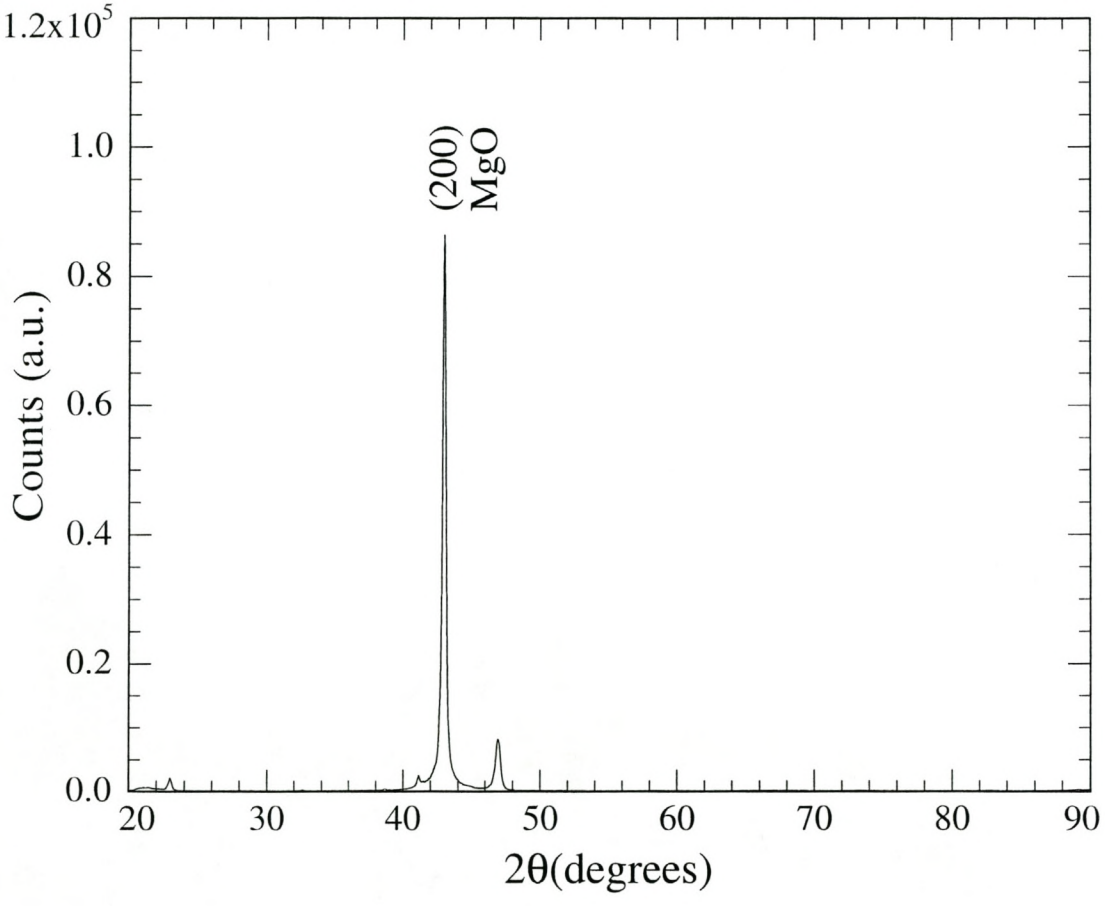

Figure 5.14: *XRD spectrum of* $La_2Ca(Mn_{0.6}Fe_{2.4})O_9$ *thin film deposited on* $MgO<100>$ *single crystal.*

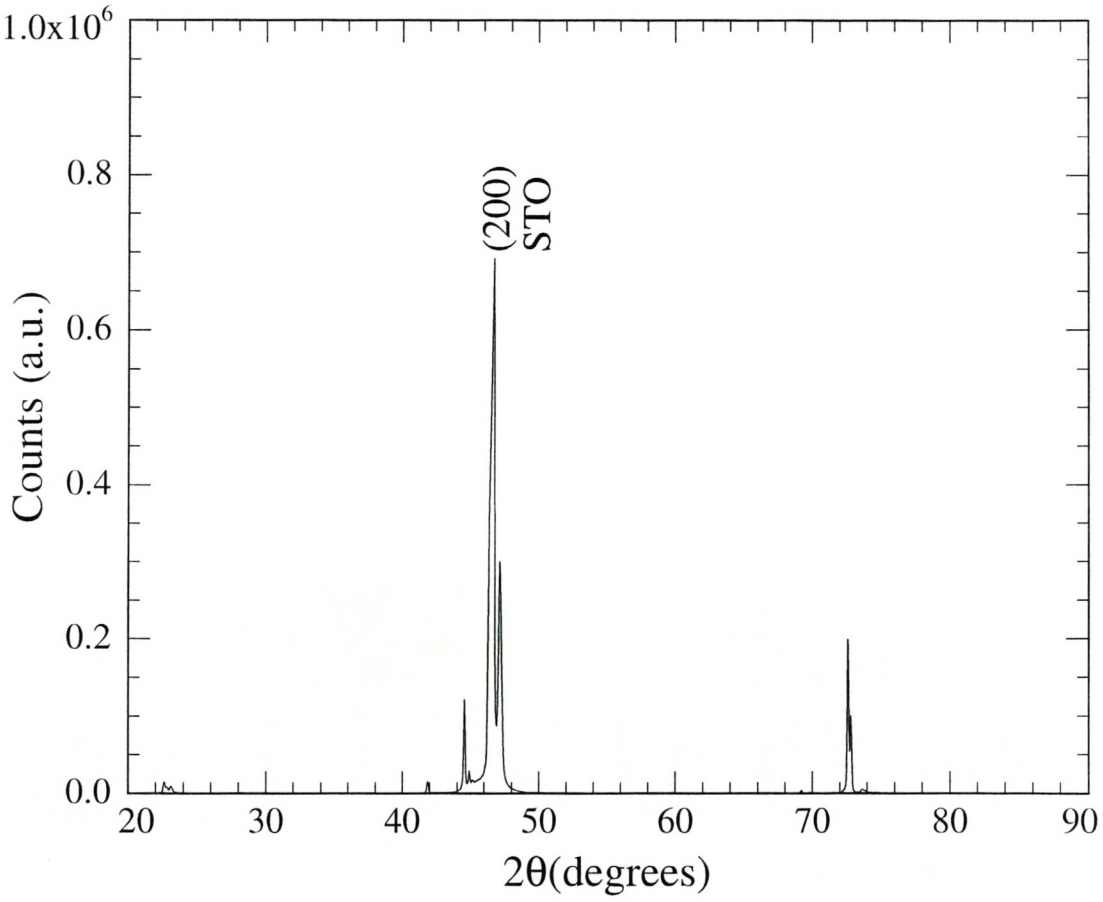

Figure 5.15: *XRD spectrum of* $La_2Ca(Mn_{0.6}Fe_{2.4})O_9$ *thin film deposited on* $SrTiO_3(STO)< 100 >$ *single crystal.*

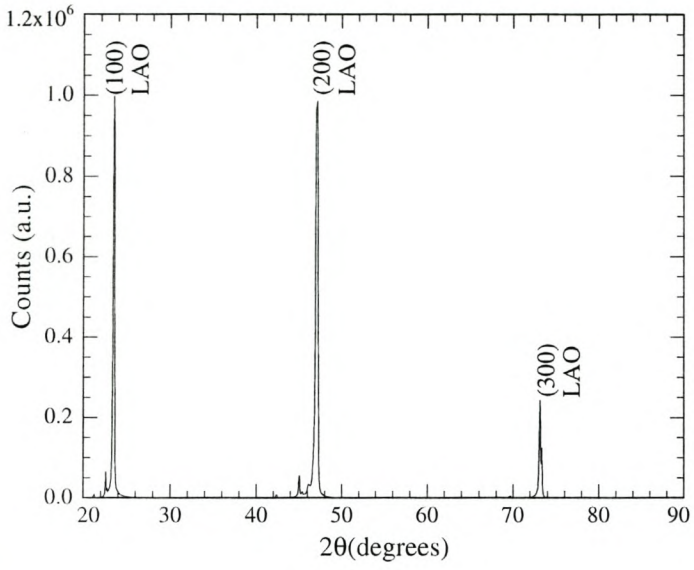

Figure 5.16: *XRD spectrum of* $La_2Ca(Mn_{0.6}Fe_{2.4})O_9$ *thin film deposited on* $LaAlO_3(LAO)< 100 >$ *single crystal.*

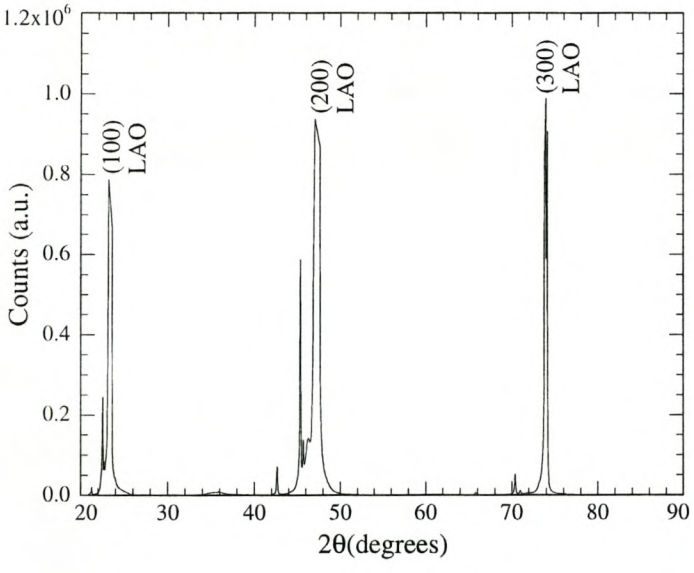

Figure 5.17: *XRD spectrum of* $La_2Ca(Mn_{2.94}Fe_{0.06})O_9$ *thin film deposited on* $LaAlO_3(LAO) < 100 >$ *single crystal.*

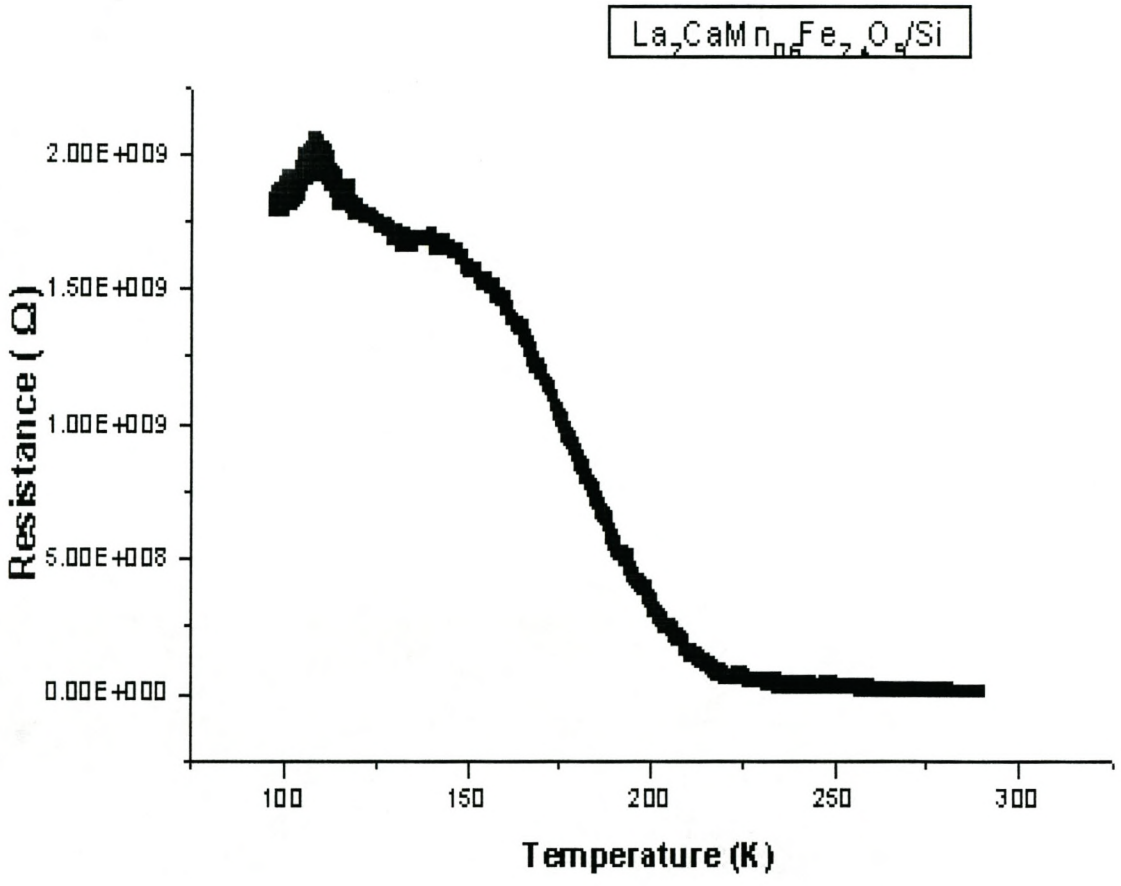

Figure 5.18: *Resistance versus temperature of* $La_2Ca(Mn_{0.6}Fe_{2.4})O_9$ *thin film. Partial oxygen pressure = 0.5 mbar.*

thin film therefore shows semiconductor behaviour.

Resistance measurements were also done at different magnetic fields for some of the samples at low temperatures. **Figure 5.19** shows how the resistance of a manganite film varies when it is subjected to a variable magnetic field. This figure is made up of two figures (resistance versus count and magnetic field versus count). Actually it represents the variation of the film resistance as a function of the applied magnetic field varying between 0 and 1 Tesla. The measurements were carried out at a constant temperature (79.86 K) and a steady current (I=100μA). It can be seen that the resistance increases with increasing magnetic field and decreases with decreasing magnetic field. The film therefore shows a small positive magnetoresistance of +0.83%, calculated as follows. From equation 1.18 where

$$MR = \frac{R(H) - R(0)}{R(H)} \times 100\% = \frac{48.4K\Omega - 48.0K\Omega}{48.4K\Omega} \times 100\% = 0.83\%$$

Usually the magnetoresistance phenomenon is measured at higher magnetic fields (see **table 5.1**) and this could be the reason for our low value. The fact that the iron content is so high could be another reason for the small magnetoresistivity found

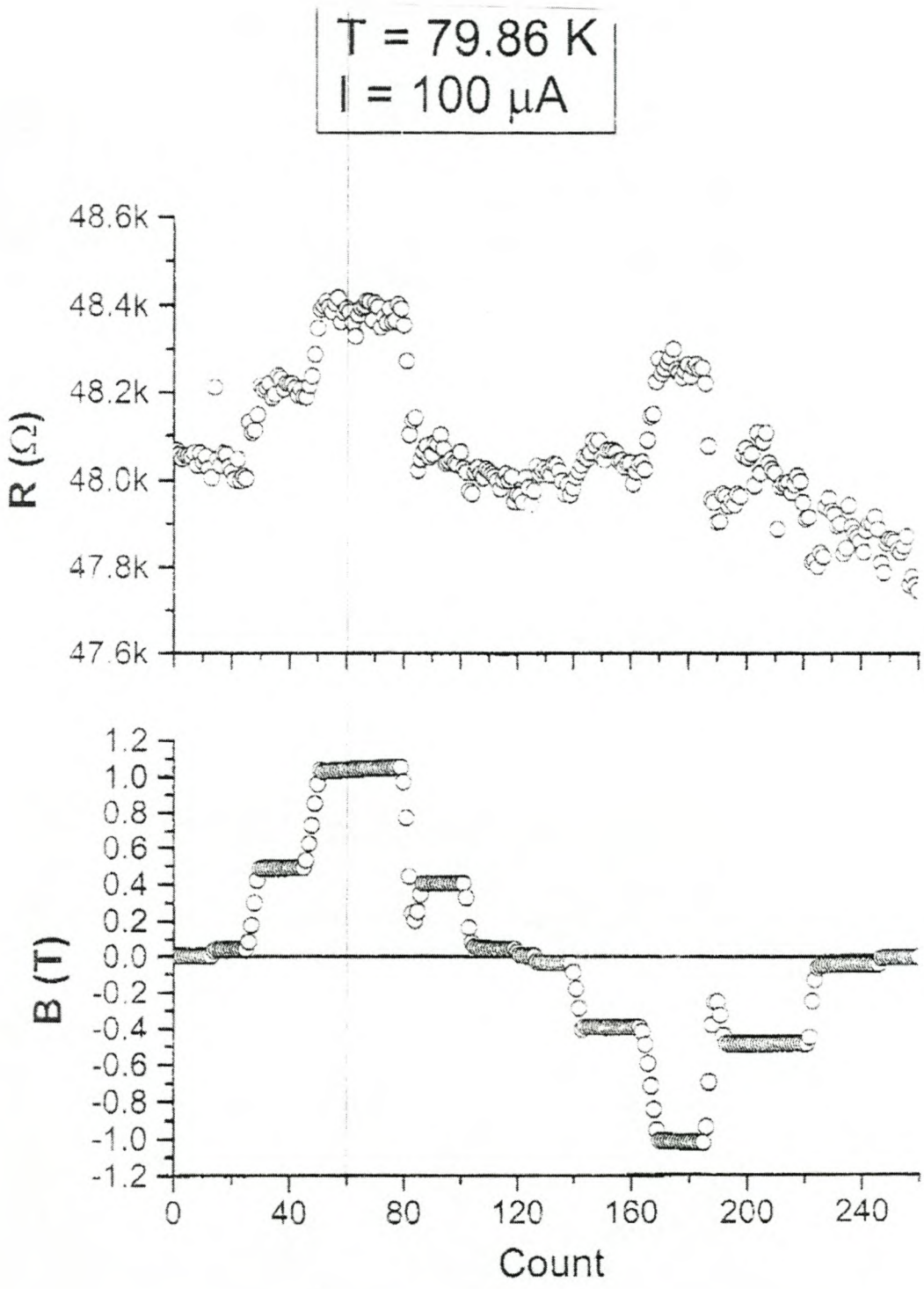

Figure 5.19: *Resistance versus magnetic field of* $La_2Ca(Mn_{0.6}Fe_{2.4})O_9$ *thin film prepared by laser ablation at a partial pressure of 0.1 mbar. The axis labelled count represents time and the two figures are correlated with each other.*

Chapter 6

Summary and Conclusion

In this investigation, the formation of thin film manganites by PLD and their characterization is studied. Interest in mixed-valence manganites was revived in the 1990s following the preparation of high-quality thin films with large magnetoresistance by Von Helmholt *et al*[13] and Chahara *et al*[14]. Thin films manganites have considerable potential for magnetic recording and magnetic sensor applications. In this work 80% of Mn is replaced by Fe in order to see the effect of oxidation states on magneto-resistivity.

In **Chapter 2**, formation and characterization techniques are presented. Pulsed laser deposition was used to fabricate the thin films. This method involves the interaction of a focussed high power laser pulse with the multicomponent bulk mixed-valence manganite material. Material ablated from the target forms a fast moving plume consisting of atomic and molecular particles, directed away from the target, and towards a usually heated substrate onto which the particles condense to form a thin film. Different techniques to characterize films prepared by PLD were used: RBS for sample thickness and stoichiometry; AFM, SEM and XRD for surface morphology, crystallinity and phase identification. Resistivity measurements were also carried out. In this investigation, two target compositions, namely $La_2CaMn_{2.94}Fe_{0.06}O_9$ and $La_2CaMn_{0.6}Fe_{2.4}O_9$ were used to fabricate thin films. Films were deposited on Si$<100>$, MgO$<100>$, $SrTiO_3<100>$ and $LaAlO_3<100>$ single crystals.

In **Chapter 3** modeling and simulation of the $La_2CaMn_{3-x}Fe_x$ system is dealt with. One of the main characterization techniques in this investigation is Rutherford Backscat-

tering Spectrometry (RBS). Details of this technique is given in **section 2.2.1**. It has been shown that RBS is a very powerful characterization technique when used in conjunction with the RUMP simulation program. The effect of various parameters can be determined beforehand by RUMP simulation of the thin film structures to be investigated. After RBS spectra have been measured experimentally for the samples produced by pulsed laser deposition, RUMP simulation was carried out in order to find the best fit with the experimental data. Simulation of spectra obtained for manganite films on Si and MgO substrates show no overlapping of the Ca, Mn and La with signals from the substrate, because the substrate consists of lighter elements than those in the films. Some overlapping was however found for $SrTiO_3$ substrates, but in these cases there was no overlapping with the La signal, due to its heavier mass. A lot of overlapping between substrate and film does occur when $LaAlO_3$ substrates are used. It has however been shown that manganite film thickness can be determined by measuring the width of the step in the La signal. Simulation shows that RBS is an excellent characterization tool for determining film thickness, using the width of either the La, Mn or Ca signal. It is ideally suited for thicknesses up to about $3000\mathring{A}$, as overlapping starts to occur for greater thicknesses. In such cases however, iterative simulation and fitting can be used. The height of RBS signals is an excellent measure of stoichiometry. Because the masses of Mn and Fe are so close to each other they cannot be distinguished. RBS therefore only gives a measure of the total Fe plus Mn content of the sample.

In **Chapter 4** the role of oxygen uptake in the $La_2CaMn_{3-x}Fe_xO_9$ system is discussed. The oxidation states of elements in manganite materials have a large effect on their magnetoresistive properties. It can be seen that all the elements have just got one oxidation state except for Mn and Fe. The most oxygen that can be accommodated by the manganite thin films during pulsed laser deposition (PLD) will therefore occur when all the Mn and Fe are in their highest oxidation states namely +7 and +3, respectively. The least uptake of oxygen will occur for Mn and Fe in their lowest oxidation states, namely +2 and +2. The amount of oxygen will naturally depend on the relative amounts of Mn

and Fe in the pulsed laser deposited thin films. The two target compositions used in this study were $La_2CaMn_{0.6}Fe_{2.4}O_{9+x}$ and $La_2CaMn_{2.94}Fe_{0.06}O_{9+x}$. When the most oxygen possible is taken up in the films, the compositions will be $La_2CaMn_{0.6}Fe_{2.4}O_{9.7}$ and $La_2CaMn_{2.94}Fe_{0.06}O_{14.38}$ respectively. When the least oxygen is taken up in the films, the compositions become $La_2CaMn_{0.6}Fe_{2.4}O_{7.0}$ and $La_2CaMn_{2.94}Fe_{0.06}O_{7.0}$ respectively. The La signal height is considerably lower for manganite films with higher oxygen content. This is due to the fact that the extra oxygen increases the energy loss of the alpha particles in the film, therefore spreading the La signal over a larger energy interval. The height of the La signal can therefore be used as a measure of the oxygen content of a film. The Ca or Mn(Fe) peak heights may also be used, but give less accuracy due to the smaller magnitude of their signals. A calibration curve for $La_2CaMn_{0.6}Fe_{2.4}O_{9+x}$ was constructed using the RUMP simulation. By measuring the height of the La signal, the oxygen content of the film may be determined using such a calibration curve. The oxygen content determines the Mn valence, responsible for magnetotransport properties of manganites. Deficiency of oxygen leads to a reduction of carrier density resulting in suppressed ferromagnetic ordering. During laser ablation, the oxygen content was controlled by adjusting the ambient oxygen pressure using a needle valve. Pressures typically between 0.01 mbar and 1 mbar oxygen were used during pulsed laser deposition. It has been proven that after deposition, the films usually have an oxygen deficit, and post-annealing in pure oxygen is needed to improve electrical and magnetic properties[56,57,58]. On the basis of this observation most of the samples deposited were annealed after deposition for one hour at 750°C under an oxygen pressure of 500 mb.

Characterization results of samples prepared by pulsed laser deposition are given in **Chapter 5**. During PLD at an energy density of 3 J/cm^2, all parameters were maintained fixed except the oxygen partial pressure which varied between 0.01 and 1 mbar, corresponding to the optimum range for magnetoresistive materials. The fixed values used during PLD are given in **Table 5.2**. RBS spectra of films deposited on single crystal silicon substrates at different ambient pressures show that the fit between simulated

and measured RBS spectra improves with higher oxygen pressures, thereby indicating better quality manganite material. The RBS spectra also show that the films have good stoichiometry as can be seen from the heights of the La, Ca and Mn signals.

Atomic force microscopy was used to determine the roughness of the thin films. It was found that the non-annealed film has more boulders than the annealed film film. These boulders are the consequence of the droplets formed due to splashing during PLD (**section 1.4.3**). Their size vary between roughly 1 μm and 7μm. It was observed that the surface roughness of the two samples are different. The annealed film (average roughness 4.5 nm) shows a surface smoother than the non-annealed film (average roughness 5.3)

Scanning electron microscopy (SEM) was also used to characterize the samples. Results were obtained for thin films prepared from the two target compositions used during our experiments, namely $La_2CaMn_{0.6}Fe_{2.4}O_9$ and $La_2CaMn_{2.94}Fe_{0.06}O_9$. The two samples were found to be different in terms of polycrystallinity. In the case of samples having a high Fe content, the crystallite size varied between about 0.04 μm and 0.10 μm, while for samples with a high manganese content, the crystallite size varied between 0.03 μm and 0.06 μm.

Manganites samples were analyzed using Bragg-Brentano (2θ) X-ray diffraction (**section 2.2.2**). The samples were deposited on various single crystal substrates, namely Si$<$ 100 $>$, MgO$<$ 100 $>$, $SrTiO_3<$ 100 $>$ and $LaAlO_3<$ 100 $>$. Reflections measured from manganite samples deposited on these substrates by PLD are summarized in **Table 5.3**. The XRD spectra for thin films deposited onto Si and MgO show very few reflections from the films. This is probably due to the fact that manganite films cannot be grown epitaxially on Si$<$ 100 $>$ and MgO$<$ 100 $>$ single crystals, due to a large lattice mismatch. In the case of $SrTiO_3$ several reflections from the film can be seen, indicating reasonable epitaxial growth. XRD spectra for manganite films deposited onto single crystal $LaAlO_3$ (LAO) substrates measured for both Fe-rich and Mn-rich manganites also

show several reflections and good peak sharpness indicating epitaxy. It is interesting to note that the reflections from the films differ slightly from the substrate reflections. This feature is especially very observable in the case of Mn-rich film and can be ascribed to stress effects and a slight difference in lattice parameter between film and substrate. SEM measurements of these samples however show crystallinity. Complete epitaxy has thus not occurred, but many grains have an epitaxial orientation.

Resistance versus temperature (from room temperature to about 100 K) in zero applied magnetic field was measured for a $La_2CaMn_{0.06}Fe_{2.4}O_9$ thin film and a maximum resistance corresponding to about 108 K was found. At higher temperatures the resistance decreases as temperature increases. The manganite thin film therefore shows semiconductor behaviour. Resistance measurements carried out at different magnetic fields (0 - 1 T) and under a constant temperature (79.86 K) at a steady current (I = 100μA) shows a small positive magnetoresistance of +0.83%. Usually the magnetoresistance phenomenon is measured at higher magnetic fields and this could be the reason for our low value, as well as the fact that the iron content is so high.

Appendix A

Definition of terms and symbols

AFM - Antiferromagnetic or Atomic Force Microscopy

k - Boltzmann's constant($1.38066 \times 10^{-23} J/K$)

CMR - Colossal Magnetoresistance

B_c - Critical magnetic field (in Tesla)

T_c - Critical temperature in superconductors or Curie temperature in magnetism (in Kelvin)

θ_D - Debye temperature. It is the temperature of a crystal's highest normal of vibration, i.e., the highest temperature that can be achieved due to a single normal vibration. The Debye temperature is given by: $\theta_D = hf_{max}/k$.

N(E) - Density of conduction electron states

DE - Double Exchange

E_g - Energy gap

E_F - Fermi energy which is the energy of the highest filled level

FM - Ferromagnetic

GMR - Giant Magnetoresistance

HTs - High Temperature Superconductors

LARES - Laser Ablation by Rapidly Exchanged Sources

M - Magnetization (amp-turn/m)

μ - mobility of electron

MRAM - Magnetoresistive Random Access Memory

T_N - Neel temperature, temperature above which an antiferromagnetic material reverts to paramagnetic material.

ORNL - Oak Ridge National Laboratories

PM - Paramagnetic

h - Planck's constant ($6.62608 \times 10^{-34} J.s$)

f(E) - Probability of finding an electron in a particular state of energy E. It is also called the Fermi-Dirac distribution function.

PLD - Pulsed Laser Deposition

ρ - resistivity ($\Omega.cm$)

RBS - Rutherford Backscattering Spectroscopy

RUMP - Rutherford Universal Manipulation Program

SEM - Scanning Electron Microscopy

R_a - surface roughness

χ - susceptibility of a material

VLSI - Very Large Scale Integrated Circuits

XRD - X-Ray Diffraction

Appendix B

X-ray crystallographic data

B.1 Plane spacings

The value of d, the distance between adjacent planes in the set (hkl), may be found from the following equations.

1. Cubic

$$\frac{1}{d^2} = \frac{h^2 + k^2 + l^2}{a^2} \tag{B.1}$$

2. Tetragonal

$$\frac{1}{d^2} = \frac{h^2 + k^2}{a^2} + \frac{l^2}{c^2} \tag{B.2}$$

3. Rhombohedral

$$\frac{1}{d^2} = \frac{(h^2 + k^2 + l^2)\sin^2\alpha + 2(hk + kl + hl)(\cos^2\alpha - \cos^2\alpha)}{a^2(1 - 3\cos^2\alpha + 2\cos^3\alpha)} \tag{B.3}$$

4. Orthorhombic

$$\frac{1}{d^2} = \frac{h^2}{a^2} + \frac{k^2}{b^2} + \frac{l^2}{c^2} \tag{B.4}$$

5. Monoclinic

$$\frac{1}{d^2} = \frac{1}{\sin^2\beta}\left(\frac{h^2}{a^2} + \frac{k^2\sin^2\beta}{b^2} + \frac{l^2}{c^2} - \frac{2hl\cos\beta}{ac}\right) \tag{B.5}$$

6. Triclinic

$$\frac{1}{d^2} = \frac{1}{V^2}\left(S_{11}h^2 + S_{22}k^2 + S_{33}l^2 + 2S_{12}hk + 2S_{23}kl + 2S_{13}hl\right) \tag{B.6}$$

In the equations for triclinic crystals, V is the volume of the unit cell (see below) and the areas are given by the following expressions

$$S_{11} = b^2c^2\sin^2\alpha$$

$$S_{22} = a^2c^2\sin^2\beta$$

$$S_{33} = a^2b^2\sin^2\gamma$$

$$S_{12} = abc^2(\cos\alpha\cos\beta - \cos\gamma)$$

$$S_{23} = a^2bc(\cos\beta\cos\gamma - \cos\alpha)$$

$$S_{12} = ab^2c(\cos\gamma\cos\alpha - \cos\beta)$$

B.2 Cell volumes

The following equations give the volume V of the unit cell.

1. Cubic

$$V = a^3 \tag{B.7}$$

2. Tetragonal

$$V = a^2c \tag{B.8}$$

3. Hexagonal

$$V = \frac{\sqrt{3}a^2c}{2} \tag{B.9}$$

4. Rhombohedral

$$V = a^3\sqrt{1 - 3\cos^2\alpha + 2\cos^3\alpha} \tag{B.10}$$

5. Orthorhombic

$$V = abc \tag{B.11}$$

6. Monoclinic

$$V = abc \sin \beta \tag{B.12}$$

7. Triclinic

$$V = abc\sqrt{1 - \cos^2 \alpha - \cos^2 \beta - \cos^2 \gamma + 2 \cos \alpha \cos \beta \cos \gamma} \tag{B.13}$$

B.3 Diffraction directions

If the Bragg law is combined with the plane spacing equation then the diffraction angle can be predicted. For example, if the crystal is cubic, then

$$\frac{1}{d^2} = \frac{h^2 + k^2 + l^2}{a^2} \tag{B.14}$$

and

$$\lambda = 2d \sin \theta \tag{B.15}$$

The combination of these equations give

$$\sin^2 \theta = \frac{\lambda^2}{4a^2} \left(h^2 + k^2 + l^2\right) \tag{B.16}$$

The reflections of the (110) planes in terms of the angle of incident x-ray, will then occur at

$$\sin^2 \theta_{110} = \frac{\lambda^2}{2a^2} \tag{B.17}$$

B.4 Expected reflections from single crystal substrates used in this study

1. Si< 100 >

   33.3^o small (2nd order)

   61.9^o small (2nd order)

66.8^o small (2nd order)

69.2^o major reflection (100)

2. MgO< 100 >

   42.8^o major reflection (200)

   94.8^o small reflection (400)

3. $LaAlO_3$< 100 >

   22.8^o major reflection (100)

   47.8^o major reflection (200)

   74.0^o major reflection (300)

4. $SrTiO_3$< 100 >

   24.3^o major reflection (100)

   46.8^o major reflection (200)

   73.8^o major reflection (300)

   104.6^0 major reflection (400)

Appendix C

The Rump RBS simulation package

The physical model of Chu *et al*[50] for the interpretation of RBS spectra is too complex for computation by hand and computer programs have been developed to implement it (see ref [51] and references therein). An algorithm has been developed[51] which substantially reduces the number of arithmetic operations required to generate accurate theoretical spectra and is known as RUMP. The idealized sample is assumed to consist of a finite number of layers with a uniform composition and sharp interfaces between layers. The focus of algorithm development has been to develop methods capable of handling thick sublayers with the emphasis on accuracy beyond that of iterated surface approximations. In the sample description layers may have arbitrary thickness, however if a layer exceeds a certain maximum thickness the simulated spectra will be inaccurate. All layers exceeding this maximum are automatically subdivided into sublayers ensuring that all sublayers in the mathematical description of the sample will produce accurate results. The final simulated spectra is built up by the contributions from every isotope of every sublayer in the sample. One such a contribution is referred to as a brick. The isotopes of elements beyond lead are not considered separately, because improvements gained will be insignificant compared to detector resolution. To evaluate the location in energy of a brick the energy lost by the beam along its inward and outward paths must be known. The beam loses energy according to the differential equation

$$\frac{dE}{da} = -\epsilon(E) \tag{C.1}$$

where $\epsilon(E)$ is the energy-dependent stopping cross section and a is the path length into the sample in areal density units. RUMP uses a fifth order polynomial least squares fit

to Ziegler's 1977 data[68]. Invoking the linear additivity of stopping cross sections for non-elemental material (Bragg's rule), coefficients defining the stopping cross section for every sublayer are computed. Given an initial beam energy of E(0) the energy of the beam passing through a single sublayer of thickness Nt at an angle θ to the normal, the problem is to arrive at E(Ntsec θ). This is accomplished by a Taylor expansion of E(a-0) around E(0),

$$E(a) = E(0) + a\frac{dE}{da} \mid_0 + \frac{1}{2}a^2\frac{d^2E}{da^2} \mid_0 + \frac{1}{6}a^3\frac{d^3E}{da^3} \mid_0 + \cdots \tag{C.2}$$

which, with ϵ, $\epsilon^{'}$ and $\epsilon^{"}$ evaluated at a=0, E=E(0) and neglecting terms beyond the third order, reduces to

$$E(a) = E_0 - a\epsilon + \frac{1}{2}a^2\epsilon\epsilon^{'} - \frac{1}{6}a^3(\epsilon^{"}\epsilon^2 + \epsilon^{'2}\epsilon). \tag{C.3}$$

The location in energy of the brick is then completely determined by the energy loss along the inward and outward path of the beam through all overlying sublayers, together with a description of the scattering events from the front and back of the brick. These scattering events are assumed to be simple elastic and are described by the appropriate kinematic factor. To determine the shape of the brick the yield of the nuclide A at the interface a is

$$y^A = \frac{x_A\sigma(E_i)}{[\epsilon(E_i)]_A \cos\theta} \prod_{layers} \frac{\epsilon(E_{in}}{\epsilon(E_{out})}. \tag{C.4}$$

Here E_i is the energy of the beam as it strikes the interface, and x_A is the atomic fraction of nuclide A in the sublayer. $[\epsilon(E_i)]_A$ is the stopping cross section factor for component A and is defined as

$$[\epsilon(E)]_A = K_A\epsilon(E) + \epsilon(K_AE). \tag{C.5}$$

The product term is taken over all overlying sublayers and each term is the ratio of the stopping power of the scattered beam between entry and exit of the sublayer[51]. To complete the description of the brick the shape is assumed to be quadratic and the extra

degree of freedom is linked to an independent computation of the area

$$area = \int_0^{Nt\sec\theta} \sigma(E(a))da. \tag{C.6}$$

The simulation is completed by a virtual multi-channel analyzer which evaluates the quadratic expression for every brick by integrating over the energy ranges corresponding to a channel. The Rutherford cross section used gives accurate answers for a wide range of beam energies and atoms. At low energies the core electrons screen the nuclear charges from each other reducing the cross section from the Rutherford value. RUMP does not attempt to correct for core electron screening and uses strictly Rutherford cross sections. At high energies nuclear reactions become important. Although RUMP does not treat such complex phenomena in general, it has recently been upgraded to handle the influence of nuclear resonances on the theoretical spectra[69]. The revised code simulates cross sections that have been fit to a set of straight line segments, and once the scattered energy is less than that of the resonance table a smooth transition to normal Rutherford scattering is made. The original code has been modified whenever the incident energy range of a brick contains a point (E_c, σ_c), and the yield at ends of the new bricks are still given by

$$y^A = \frac{x_A\sigma(E_c)}{[\epsilon(E_c)]_A\cos\theta}\prod_{layers}\frac{\epsilon(E_{in}}{\epsilon(E_{out})}. \tag{C.7}$$

The product

$$r = \frac{x_A}{[\epsilon(E_c)]_A\cos\theta}\prod_{layers}\frac{\epsilon(E_{in}}{\epsilon(E_{out})}, \tag{C.8}$$

is not calculated exactly, but linearly interpolated based on the placement of E_c relative to the end points of the original brick. $\sigma(E_{front})$ and $\sigma(E_{back})$ are interpolated from the non-Rutherford cross section curve. The use of the ^{16}O elastic resonance with 3.045 MeV alpha particles in determining oxygen content of high Z oxides has been illustrated [69] and accuracies in the range of 5% were obtained. Typically evaluation of RBS spectra are based on overlaying a theoretical spectrum with the experimental one and iteratively modifying the parameters of the synthesis until an adequate fit is achieved. An algorithm has been developed which automates this fitting procedure[70]. Once a

qualitative description of the sample has been established, the algorithm will search for the "best fit" values from a set of parameters. Quantitative estimates of statistical uncertainty of each parameter are also determined. The norm used to evaluate the distance between a synthesized and an experimental spectrum is the Poisson maximum likelihood χ^2 function

$$\chi^2 = -2\sum(n_i(1 - \ln(n_i/t_i)) - t_i), \tag{C.9}$$

given n_i as the experimental number of counts in channel i, and t_i as the synthesized number of counts in channel i. χ^2 will then depend upon the parameters $\mathbf{x}$ used to describe the sample[70]. The minimization algorithm determines an approximate expression for χ^2 near its minimum, in the form

$$\chi^2(\mathbf{x}) \approx \chi_{\mathbf{0}}^{\mathbf{2}} + \frac{\mathbf{1}}{\mathbf{2}}(\mathbf{x} - \mathbf{x_0})^{\mathbf{T}}\mathbf{H}(\mathbf{x} - \mathbf{x_0}). \tag{C.10}$$

$\mathbf{x_0}$ represents the vector of "best fit" values, χ_0^2 is the minimum χ^2 achieved, and $\mathbf{H}$ is the positive definite Hessian matrix. χ_0^2 can be used as a guide to the "goodness of fit". The Hessian matrix provides uncertainty information

$$H_{ij}^{-1} = \sigma_{x_i x_j}, \tag{C.11}$$

(the ij element of H^{-1} is the covariance of the ith and jth parameter).

Bibliography

[1] R.A Serway, *Physics for Scientists and Engineers with Modern Physics*, Saunders College Publishing, third edition, 1982

[2] E.J. Maritz, *Flux Creep in Pulsed Laser Deposited Superconducting* $YBa_2Cu_3O_7$ *thin films*. PhD Thesis, University of Stellenbosch, 2002.

[3] N.F. Mott and H. Jones, *The Theory of the Properties of Metals and Alloys*, Dover Publications, Inc., New York, (1958).

[4] D.D Pollock, *Electrical Conduction in Solids: An Introduction*, American Society for Metals, Metals Park, OH, (1985).

[5] A.C. Rose-Innes and E.H. Rhoderick.*Introduction to Superconductivity*, Pergamon Press, first edition, 1969.

[6] J. Li, *Pinning Phenomenon in High-Tc Superconductors*, PhD thesis, University of Amsterdam, 1992.

[7] A.R. West. *Solid State Chemistry and its Applications*. John Willey & Sons Ltd, 1984.

[8] T. Thio et al., *Phys. Rev.*, **B 57**(1998) 12239.

[9] http://researchweb.watson.ibm.com/research/gmr.html

[10] A. Fert et al, *Phys. Rev. Lett.*, **61** (1988) 2472.

[11] M.D Coey et al, *Phys. Rev. Lett.*, **80** (1998) 3815.

[12] J.Z. Sun et al., *IBM Journal of Research and Development*, **vol 42**, $N^0 1$.

[13] Von Helmholt et al, *Phys. Rev. Lett.*, **71** (1993) 2331.

[14] K. Chahara et al, *Appl. Phys. Lett.*, **63** (1990).

[15] P. Schiffer et al, *Phys. Rev. Lett.*, **75** (1995) 3336

[16] S. Jin et al, *Science*, **264** (1994) 413.

[17] H. Y. Hwang et al, *Phys. Rev. Lett.*, **77** (1996) 2041.

[18] C. Zener, *Phys. Rev.*, **81**(1951)440.

[19] C. Zener, *Phys. Rev.*, **82**(1951)403.

[20] E. Pollert et al, *J. Phys. Chem. Solids*, **43**(1982)1137.

[21] G. Zhao et al, *Nature*, **381** (1996) 676.

[22] E.L. Nagaev, *Uspekhi Fizicheskikh*, **39** (1996) 781 english translation.

[23] P.A Algarabel, J.M. De Teresa, C. Marquinq, B. Garcia-Landa, C. Ritter and M.R. Ibarra, submitted.

[24] V.M. Goldsmith, *Geochemische Verteilungsgesetse der Elemente VII-VIII*, 1928 (1927.

[25] K.H. Ahnet et al, *Phys. Rev.*, **B54** (1996).

[26] N. Witte and J. Goodenough, *Australian Journal of Physics*, **52** (1999).

[27] S. Satpathy et al, *J. Appl. Phys.*, **79** (1996) 4555.

[28] I. Solovyev et al, *Phys. Rev. Lett.*, **79** (1996) 4825.

[29] P.W. Anderson and H. Hasegawa, *Phys. Rev.*, **100** (1955) 675.

[30] P.G De Gennes, *Phys. Rev.*, B**118** (1960) 141.

[31] J.W Cai et al, *Appl. Phys. Lett.*, **71** (1997) 12.

[32] F. Breech anf L. Cross, Optical micromission stimulated by a ruby laser. *Appl. Spectroscopy*, **16** (1962) 59.

[33] H.M. Smith and A.F Turner, *Appl. Opt.*, **4** (1965) 147.

[34] T. Venkatesan. *Pulsed laser Deposition of High-Temperature Superconducting Thin films in Laser Ablation : Principles and Applications by J.V Miller (ed.)*, chapter 4, page 85, Springer-Verlag, (1994).

[35] T. Venkatesan, *Appl. Phys. Lett.*, **52** (1988) 1193.

[36] D.H. Lowndes. Growth and doping of compound semiconductor films by pulsed laser ablation. In Miller J.C. and Haglund R.F., editors, *Laser Ablation and Desorption*, volume 30 of *Experimental Methods in the Physical Sciences*, chapter 11, pages 475-571. Academic Press, San Diego, 1998.

[37] D.B Geohegan. Diagnostic and charactheristics of pulsed laser deposition plasma. In Chrisley D.B. and Hubler, editors, *Pulsed Laser Deposition of Thin films*, chapter 5, pages 115-165. John Wiley and Sons Inc., New York, U.S.A., 1994.

[38] I.V. Nemchinov and S.V. Popov. *JEPT Lett.*, **11**, (1970) 312.

[39] R.K. Singh and J. Narayan. *Phys. Rev. B*, **41** (1990) 8843.

[40] C.H. Becker and J.B. Pallix. *J. Appl. Phys.*, **64** (1988) 5152.

[41] K.L. Saenger. Angular distribution of ablated material. In Chrisley D.B and Hubler G.K., editors, *Pulsed Laser Deposition of Thin Films*, chapter 7, pages 199-227. John Wiley and Sons, New York, U.S.A., 1994.

[42] R.E. Muenchausen et al, *Appl. Phys. Lett.*, **56** (1990) 578.

[43] A.D. Akhsakhalyan et al, *Sov. Phys. Tech. Phys.*, **33** (1988) 1146.

[44] http://www.ornl.gov/ORNLReview/rev30-12/text/advanced.htm. Advanced Materials, Processing, Synthesis, and Characterization.

[45] http://www.ornl.gov/ORNLReview/rev27-12/text/lasmain.html. Laser Ablation: Opening Doors to New Materials for Industry by Carolyn Krause.

[46] J.A. Philips. Substrate selection for high-temperature superconducting thin films.*J. Appl. Phys.*, **79** (1996) 1829-1848.

[47] D.W. Pashley. In J.W. Matthews, editor, *Epitaxial growth.* Academic press, New York, U.S.A., 1975.

[48] R. Guo, A.S. Bhalla, L.E. Cross, and R. Roy, *J. Mater. Res.*, **9** (1994) 1644.

[49] Superconductive Components Inc. 1995 Product Guide. Columbus, Ohio., U.S.A., 1995.

[50] W.K. Chu, J.W. Mayer, and A.M. Nicolet. *Backscattering Spectrometry.* Academic Press, New York, U.S.A., 1978.

[51] L.R. Doolittle. *Nucl. Inst. Meth.*, **9** (1985) 344.

[52] S.N. Magonov and M.H. Whangbo, *Surface Analysis with STM and AFM.* VCH Verlaggesellschaft, Weinheim, Germany, 1996.

[53] G. Binning et al, *Phys. Rev. Lett.*, **56** (1986) 930.

[54] Topometrix, http://www.topometrix.com. *Topometrix scanning probe microscope -user's guide*, 1998.

[55] B.D. Cullity, *Elements of X-ray diffraction.* Addison-Wesley, Reading, Massachussets, U.S.A., 1978.

[56] W. Zhang et al, **Appl. Phys. Lett., 69(25)** (1996) 3929.

[57] C. Osthover et al, **Mater. Sci. Eng., B56** (1998) 164.

[58] H. Ju et al, **Phys. Rev., 51(9)** (1995) 6143

[59] R. Mahendiran et al, **Phys. Rev. B 53** (1996) 3348.

[60] R. Mahesh et al, **Appl. Phys. Lett. 68** (1996) 2291.

[61] G.C. Xiong et al, *Appl. Phys. Lett*, **66** (1995) 1427.

[62] L.H. Chen et al, *IEEE Trans. Magn.*, **31**, (1995) 3912.

[63] G. Srinivasan et al, *Appl. Phys. Lett.*, **67** (1995) 2090.

[64] X.T. Zeng and H.K. Wong, *IEEE Trans. Magn.*, **31** (1995) 3910.

[65] V.S. Achutharaman et al, *Appl. Phys. Lett.*, **67** (1995) 1019.

[66] A. Gupta et al, *Appl. Phys. Lett.*, **67** (1995) 3494.

[67] Z. Trajanovie et al, *Appl. Phys. Lett.*, **69** (1996) 1005.

[68] J.F Ziegler, *Helium, Stopping Powers and Ranges in All Elements*, (Pergamon, New York, 1977).

[69] B.Blanpain et al, *Nucl. Instr. Meth. B*, **34** (1988) 459.

[70] L.R. Doolittle, *Nucl. Instr. Meth. B*, **15** (1986) 227.